Università degli Studi di Padova

Dipartimento di Fisica e Astronomia "Galileo Galilei"

Master Degree in Astrophysics and Cosmology

Final Dissertation

Neutrino Triggered Target of Opportunity: multi-messenger view of the gamma-ray flaring blazar OP 313

Supervisor:

Prof. Elisa Bernardini
Università degli studi di Padova

Co-Supervisors:

Prof. Pratik Majumdar
Saha Institute of Nuclear Physics

Dr. Davide Miceli
Istituto Nazionale di Fisica Nucleare

Candidate:

Alessandra Briscioli

Academic Year 2023/2024

"The cosmos is within us. We are made of starstuff.
The nitrogen in our DNA, the calcium in our teeth,
the iron in our blood, the carbon in our apple pies
were made in the interiors of collapsing stars.
We are thinking matter, stardust with consciousness.
We are a way for the Universe to know itself."

Carl Sagan

Sommario

Negli ultimi decenni, il campo dell'astrofisica ha abbracciato sempre di più un approccio multi-messaggero, in particolare modo per indagare fenomeni extragalattici come i Nuclei Galattici Attivi (AGN), più specificatamente la sotto-classe dei blazar.
Un evento degno di nota del 2017, che ha visto la rilevazione di un neutrino ad alta energia dal blazar TXS 0506+056 insieme a un brillamento di raggi gamma osservato dai telescopi MAGIC, ha sottolineato l'importanza di questo approccio.
Questa tesi si concentra su un altro blazar, OP 313, che ha sperimentato un flare significativo ad alta energia da dicembre 2023. Questo evento ha fornito l'opportunità di un'indagine completa multi-messaggera. La tesi mira a identificare potenziali correlazioni tra i fotoni gamma osservati dai telescopi MAGIC e Fermi-LAT e i segnali di neutrini di IceCube.
Dal punto di vista metodologico, i dati dei telescopi MAGIC vengono calibrati e convertiti, seguiti dalla pulizia del fondo e dalla parametrizzazione dell'immagine. Vengono impiegati algoritmi specifici per ricavare informazioni sul tipo, la direzione e l'energia della particella primaria, che portano a un'analisi di alto livello per determinare il significato del brillamento, la distribuzione dell'energia spettrale e la curva di luce.
I risultati indicano una forte emissione di raggi gamma ad altissima energia (VHE) da OP 313, un fenomeno precedentemente non rilevato. Anche le osservazioni di Fermi-LAT mostrano un'intensa emissione che persiste da novembre 2023. Inoltre, due recenti segnalazioni di neutrini da parte di IceCube sono state segnalate in direzione di OP 313, appena al di sopra della soglia di rilevazione.
Lo studio di OP 313, insieme a quello dei blazar in generale, è importante per chiarire i meccanismi dei getti nei blazar. Un approccio multi-messaggero è ritenuto essenziale per discernere se lo scenario di accelerazione dei raggi cosmici (CR) sia lepto-adronico o puramente leptonico.

Abstract

In the last decades, the field of astrophysics has increasingly embraced a multi-messenger approach, particularly in investigating extragalactic phenomena like Active Galactic Nuclei (AGNs) and more specifically the sub-class of blazars.
A notable event in 2017, involving the detection of a high-energy neutrino from the blazar TXS 0506+056 alongside a gamma-ray flare observed by MAGIC telescopes, underscored the importance of this approach.
This thesis focuses on another blazar, OP 313, which experienced a significant high-energy flare from December 2023. This event provided an opportunity for a comprehensive multi-messenger view, especially since recent neutrino alerts originated from the same source direction. The thesis aims to identify potential correlations between gamma photons observed by MAGIC and Fermi-LAT telescopes and neutrino signals from IceCube.
Methodologically, data from MAGIC telescopes are calibrated and converted, followed by background cleaning and image parameterization. Specific algorithms are employed to derive information about the primary particle's type, direction, and energy, leading to a high-level analysis to determine the significance of the flare, spectral energy distribution, and light curve.
The results indicate a strong emission of Very High Energy (VHE) gamma rays from OP 313, a phenomenon previously undetected. Fermi-LAT observations also show intense emission persisting from November 2023. Additionally, two recent neutrino alerts from IceCube were reported in the direction of OP 313, just above the detection threshold.
The study of OP 313, alongside blazars in general, holds significance in elucidating the mechanisms within blazar's jets. A multi-messenger approach is deemed essential for discerning whether the Cosmic Ray (CR) acceleration scenario is lepto-hadronic or purely leptonic.

Contents

List of Figures

Chapter 1

INTRODUCTION

Astroparticle physics is a burgeoning branch of physics that explores the intersection of astrophysics and particle physics. It focuses on the study of elementary particles of astronomical origin and their interactions with cosmic environments. This field aims to answer fundamental questions about the Universe by investigating high-energy particles, namely neutrinos, cosmic rays, and gamma rays, that originate from space.
A still unclear topic in astroparticle physics is the origin of cosmic rays. These high-energy particles are detected on Earth, but their production sites remain elusive since their paths are deflected by magnetic fields during their propagation through the Universe. Nevertheless, their origin can be probed combining information coming from the other cosmic messengers, such as neutrinos and photons (especially gamma-rays). In fact, these messengers do not lose information on their origin since they are electrically neutral. In addition, gamma-rays and neutrinos can originate also as secondary products from the interaction of cosmic rays in the Universe. As a result, the study of the processes involved in the production of gamma-rays and neutrino can directly link to investigate also the origin of the cosmic rays. An important class of objects candidate as source of cosmic rays is Active Galactic Nuclei (AGN), especially the sub-class of blazars. AGNs are galactic nuclei powered by supermassive black holes that accrete matter, producing extremely powerful non-thermal radiation that can exceed the emission of their host galaxies. Ultra-relativistic jets of matter are present in some AGNs. In the case of blazars these jets point directly toward the observer. This alignment causes the intrinsic emission from blazars to appear highly boosted in the observer's reference frame due to relativistic beaming effects.
The Spectral Energy Distribution (SED) of a blazar has two typical peaks. The first one, at low energy, is usually attributed to synchrotron radiation from accelerated electrons within the jet. The origin of the second peak, at higher energy, is debated and could be due to leptonic (involving electrons) or hadronic (involving protons) processes. In the latter case, blazar jets could then provide an ideal environment for cosmic ray acceleration. So, gamma-ray observations are crucial to fully characterize this second hump.
The discovery, in 2017, of a high-energy neutrino detected by IceCube in the direction of the blazar TXS 0506+056 [1], coinciding with enhanced emission in gamma-rays, provided strong evidence for hadronic processes occurring within relativistic jets, and

thus that blazars may provide environments for cosmic ray acceleration (see Appendix A for more details). This discovery opened a new window in astronomy known as "multi-messenger astrophysics" which involves observations of different cosmic messengers. In this case, it involves the simultaneous study of gamma rays and high-energy neutrinos.
Using the same approach, my thesis focuses on the blazar OP 313, which was detected at an enhanced state in the gamma energy range from December 2023 until April 2024, and for which two neutrino alerts were issued by IceCube in March 2024.
I performed the analysis of the MAGIC data collected for OP 313 during the recent flare episode. Then, I complemented these results both with archival observations performed by the MAGIC telescopes from 2014, simultaneous and long-term multi-wavelength results obtained in lower energy ranges from other instruments and the recent results from the IceCube Observatory. The goal of this approach is to investigate possible links in a multi-messenger scenario and characterize the source properties.
The thesis is structured as follows:

- **Chapter 2** provides an introduction to the multi-messenger astrophysics, particularly by briefly describing cosmic messengers (cosmic rays, photons and neutrinos), and the candidate multi-messenger sources, with particular focus on AGNs, especially the sub-class of blazars.
- **Chapter 3** outlines various gamma-ray detection methods, including both direct and indirect techniques, with a particular emphasis on the Fermi-LAT instrument and the MAGIC telescopes. Additionally, it provides insights into high-energy neutrino detection methodologies, focusing on the IceCube telescope.
- **Chapter 4** is dedicated to the MAGIC data analysis procedure, in particular to the description of data taking and the MARS software used.
- **Chapter 5** describes the main properties of the blazar OP 313 and reports all archival data on this source taken with MAGIC and Fermi-LAT telescopes and past IceCube alerts. Most importantly, It presents the new recent results from December 2023 to April 2024 taken with MAGIC and Fermi-LAT telescopes and the new IceCube alerts.
- **Chapter 6** draws the conclusions of this comprehensive analysis of OP 313 and discusses the future perspectives.

Chapter 2

MULTI-MESSENGER ASTROPHYSICS

Multi-messenger astrophysics is a branch of astrophysics that has emerged in recent decades due to new discoveries in particle and astroparticle physics as well as technological progress. Traditionally, astrophysics has primarily relied on the analysis of celestial objects through the observation of their light emissions across various wavelengths. Multi-messenger astrophysics, however, introduces an innovative paradigm, wherein investigations of celestial sources incorporate data not only from electromagnetic radiation (photons) but also from other cosmic messengers such as neutrinos, cosmic rays, and gravitational waves. Given the diverse properties and interactions of these different particle types, their collective examination enables the explanation of distinct processes occurring within a single source, thereby revealing additional characteristics that define the source's nature. In this Chapter I will present an overview of the three cosmic messengers that are important for the purpose of this thesis, namely cosmic rays, photons (particularly gamma-rays), and neutrinos (Section 2.1) and describe the possible environments that can generate these messengers (Section 2.2), focusing on a particular subclass of AGNs, called blazars.

2.1 Cosmic messengers

It is important to undertake a comprehensive study of a source employing various messengers to facilitate the acquisition of complementary information. This approach is particularly useful in elucidating the enigmatic origin of cosmic rays. One way through which this endeavor can be pursued involves the examination of gamma photons and neutrinos. Cosmic rays are charged particles subject to deflection during their travel to Earth, thereby compromising directional cues. Neutrinos and photons are neutral particles and therefore retain direction information. Nevertheless, while photons interact with matter and are often absorbed or scattered, neutrinos exhibit minimal interaction with matter. In Figure 2.1 the generation and propagation of ultra-high-energy particles throughout the Universe is schematized.

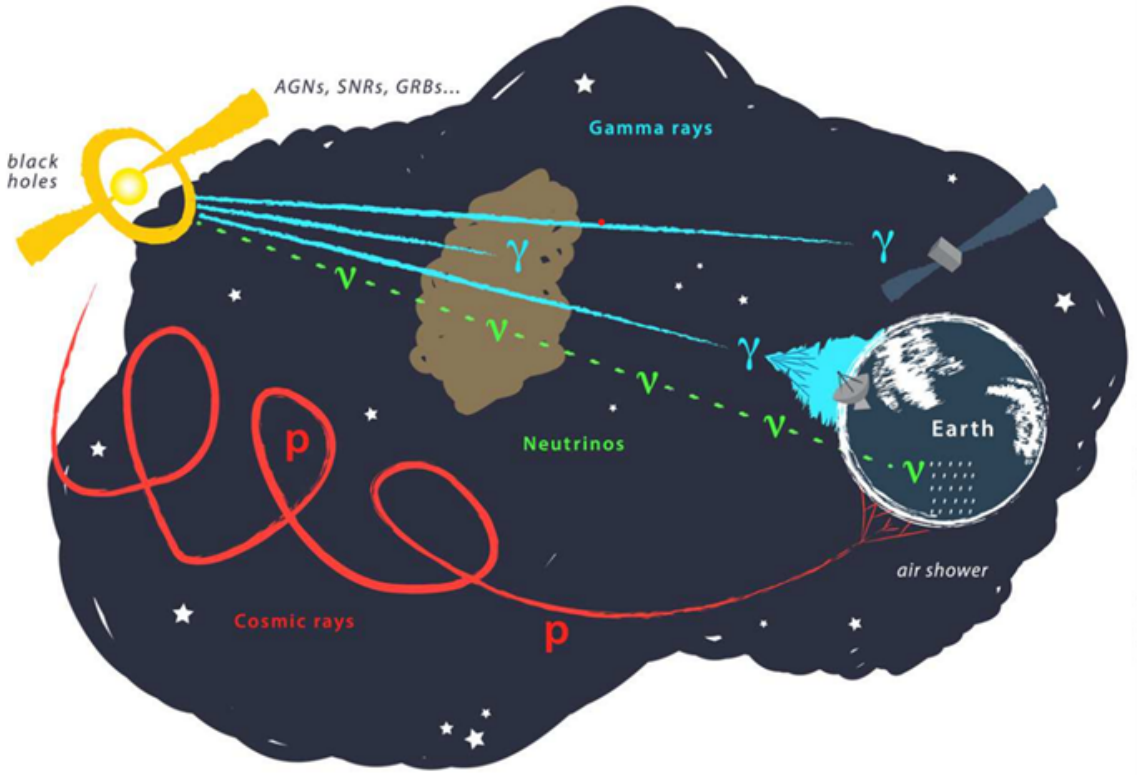

Figure 2.1: The generation and propagation of ultra-high-energy particles in the Universe. It is clear that it is possible to examine a given source, such as an Active Galactic Nucleus (in yellow) through the detection of various particles from that source, i.e. cosmic rays (in red), neutrinos (in green), and photons (in blue), as they pass through the Earth. Credit: IceCube Collaboration.

2.1.1 Cosmic rays

Cosmic Rays (CR) are charged energetic particles and atomic nuclei that, moving almost at the speed of light, strike the Earth from all directions. They are produced in both galactic and extra-galactic environments. The existence of CRs was discovered by Victor Hess in 1912 [2]. At the beginning, no explanation could be found for the following problem: there appeared to be more radiation on the ground than the one produced by natural radioactivity. Therefore, Hess did an experiment on a balloon through an electroscope. He measured that the amount of charged particles increased with altitude. This was the first evidence of an unknown radiation that had no terrestrial origin but came from space. It was called "cosmic rays". Today, we know that CRs are composed of about 90% protons and 9% helium nuclei. The remaining 1% are heavier nuclei and lighter particles such as the electron or positron and other subatomic particles. Because CRs are electrically charged, they are deflected by galactic, extragalactic and terrestrial magnetic fields, so their original direction is lost (except possibly at higher energies, since deflection decreases with CR energy, however at such high energies other issues arise such as the attenuation due to the interaction with CMB).
Let us now focus on the description of the CR spectrum (Figure 2.2). CRs have en-

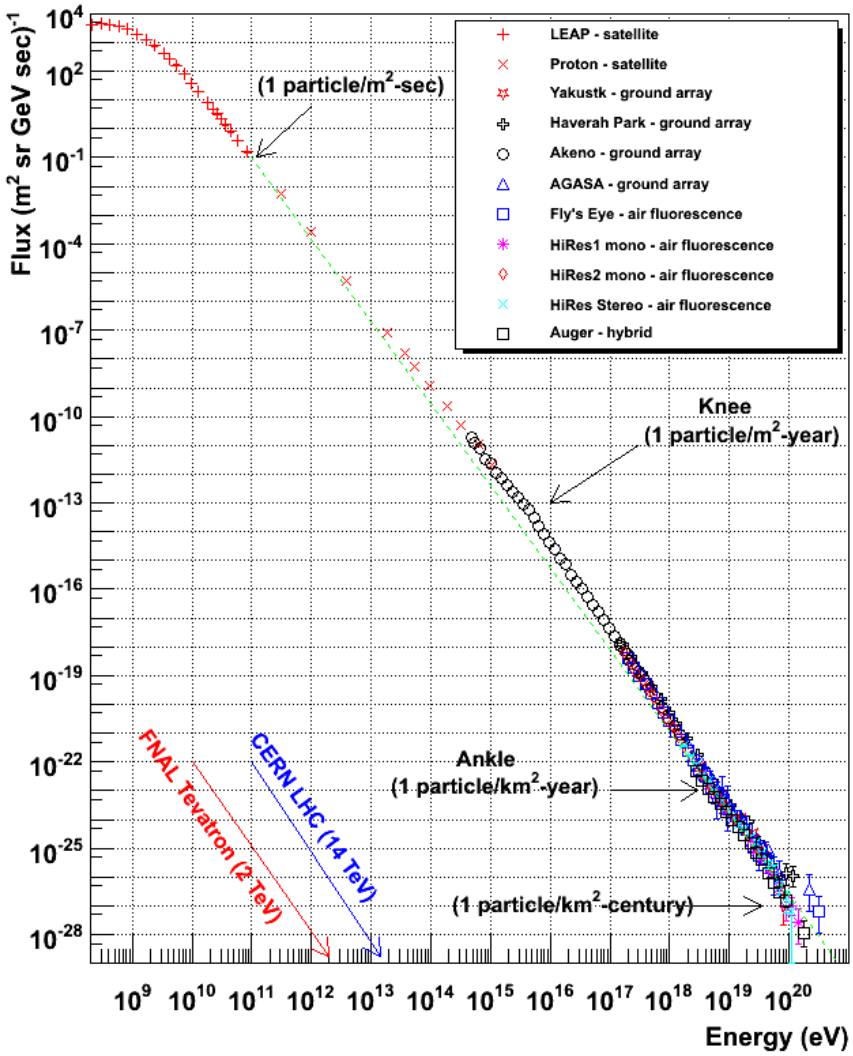

Figure 2.2: Cosmic ray spectrum observed from Earth. Figure taken from [3].

ergies that span a very wide range. As we can see in the Figure, the number of CRs decreases with increasing energy. For example, the flux of CRs entering the atmosphere with energy around 1 GeV is about 1 m^{-2} s^{-1}, but becomes 1 m^{-2} yr^{-1} at 10^6 GeV and even only 1 km^{-2} century^{-1} at the highest energies of the order of 10^{12} GeV. The shape of the spectrum can be described by powerlaw functions [4, 5]:

$$\frac{dN}{dE} \propto \begin{cases} E^{-2.67} & 100 \text{ GeV} < \text{E} < 3 \text{ PeV} \\ E^{-3.10} & 3 \text{ PeV} < \text{E} < 3 \text{ EeV} \\ E^{-2.75} & \text{E} > 3 \text{ EeV} \end{cases} \tag{2.1}$$

Two slope changes can be seen: the first around 1 PeV (known as the "knee"), the second around 1 EeV (known as the "ankle"). It is thought that below 1 GeV the composition of CRs consists of particles from the solar system (since the solar magnetic field blocks less energetic particles from outside), between 1 GeV and knee the composition is galactic, and between 1 PeV and 1 EeV a transition from galactic to

extragalactic CRs occurs. In addition, it is seen from the Figure that the spectrum beyond 10 EeV undergoes a cut-off, called GZK cut-off [6, 7], due to interactions with CMB photons.

Cosmic-rays acceleration

In 1949, Enrico Fermi proposed a mechanism that could explain the acceleration processes involved in CRs [8]. This mechanism, called "shock acceleration", is based on the acceleration of CRs due to their repeated crossing of shock fronts. The mechanisms depend on the properties of the moving plasma and are called first and second-order Fermi acceleration.
First-order Fermi acceleration occurs when a CR travelling through a shock wave encounters magnetic field inhomogeneities. Variations in the magnetic field encountered cause the particle to bounce back and forth across the shock. This causes the gain of energy by the particle (ΔE/E), and it can be shown that this is proportional to the velocity of the shock: $\Delta E/E \propto \beta$, where β represents the average velocity of the shock in units of the velocity of light c.
Second-order Fermi acceleration of a moving charged particles occurs in the presence of a moving magnetized cloud. In this process, $\Delta E/E \propto \beta^2$.
The environments in which CRs are generated are not yet fully understood. However, it is possible to find shock waves in objects like SuperNova Remnants (SNRs), or in Gamma Ray Burst (GRBs) or in jets of AGNs. The Hillas diagram [9] in Figure 2.3 plots the magnetic field of the sources as a function of their size, showing the most plausible candidates for the formation of CRs at a given energy.

2.1.2 Gamma-rays

The most intuitive and frequently used messenger is the electromagnetic radiation, commonly referred to as light. Photons are massless and neutral particles. The directional arrival of photons directly correlates with the origin from which they are emitted. The electromagnetic spectrum outlines the set of possible frequencies of electromagnetic radiation, spanning a continuum from radio waves to infrared radiation, proceeding through the visible spectrum, extending to x-rays, and culminating in the most energetic gamma-rays, as illustrated in Figure 2.4.
Within the scope of this thesis, our primary emphasis lies in the description of gamma-rays. Specifically, we categorize them into distinct energy ranges:

- Low Energies (LE): Ranging from 100 keV to 30 MeV.
- High Energies (HE): Ranging from 30 MeV to 100 GeV.
- Very High Energies (VHE): Ranging from 100 GeV to 30 TeV.
- Ultra High Energies (UHE): Ranging from 30 TeV to 30 PeV
- Extremly High Energies (EHE): with Energy $>$ 30 PeV

When discussing the electromagnetic spectrum, it is essential to consider the absorption probability of photons upon entering Earth's atmosphere, dependent upon their energy (or wavelength or frequency). As depicted in Figure 2.5, the Earth's

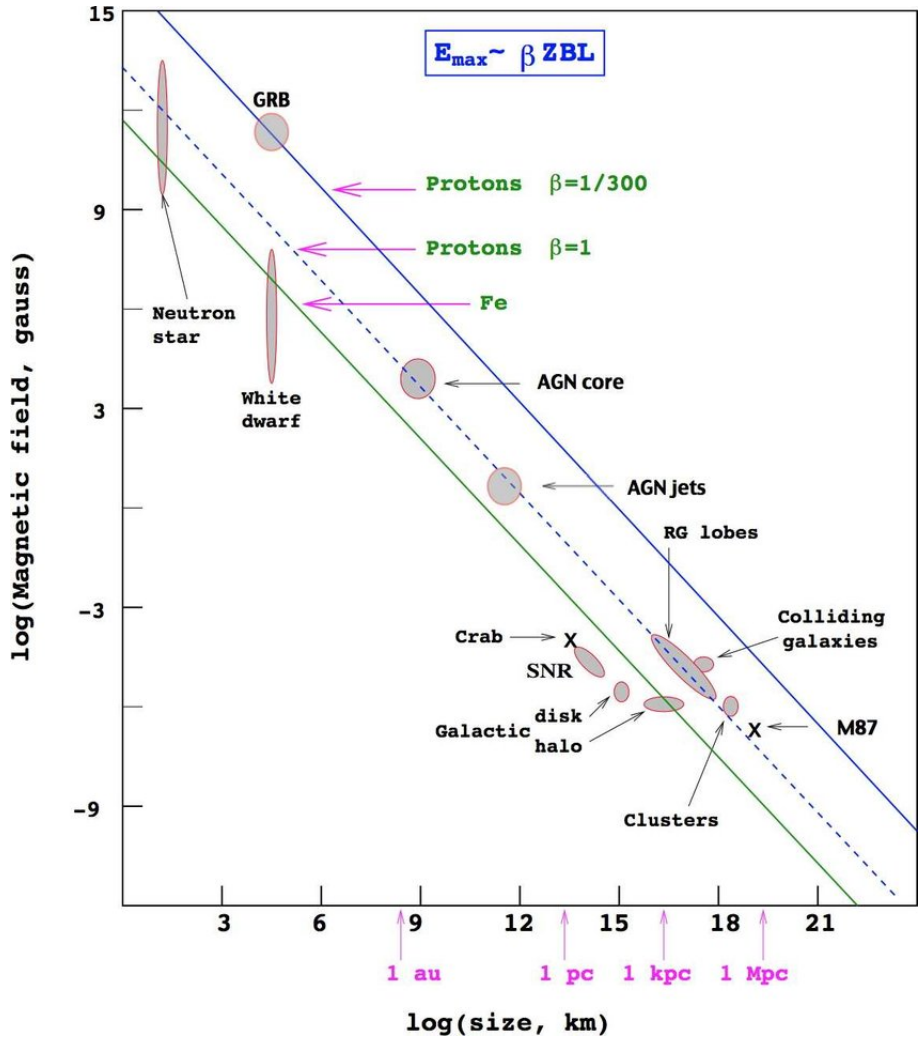

Figure 2.3: Hillas plot for candidate acceleration sites, relating their size and magnetic field strength. To accelerate a given particle species above 100 EeV objects must lie above the corresponding lines. Figure taken from [10].

atmospheric composition generates the absorption of nearly all photons surpassing the energy threshold of the ultraviolet band, thus precluding direct observation by ground-based telescopes. This phenomenon has significant importance in explaining the necessity of using indirect detection methodologies, such as those used by the Cherenkov telescopes (as explained in Chapter 3). Actually, there exists minimal uncertainty regarding the presence of UHE and EHE photons [11]. Gamma-rays have been indisputably detected only in the MeV, GeV and TeV ranges. This lies in the fact that at the most extreme energies the interaction between gamma photons and what is called Extra-galactic Background Light (EBL) becomes increasingly important. EBL photons, which are photons belonging to the all radiation accumulated in the Universe due to star formation processes (composed mainly of starlight and starlight absorbed/reprocessed by dust), can interact with photons in the VHE domain and above, generating electron-positron pairs. In this way, the gamma-ray flux at these very high energies gets attenuated. The behavior beyond approximately 30 TeV is indeed inferred through extrapolation from data acquired at lower energy levels

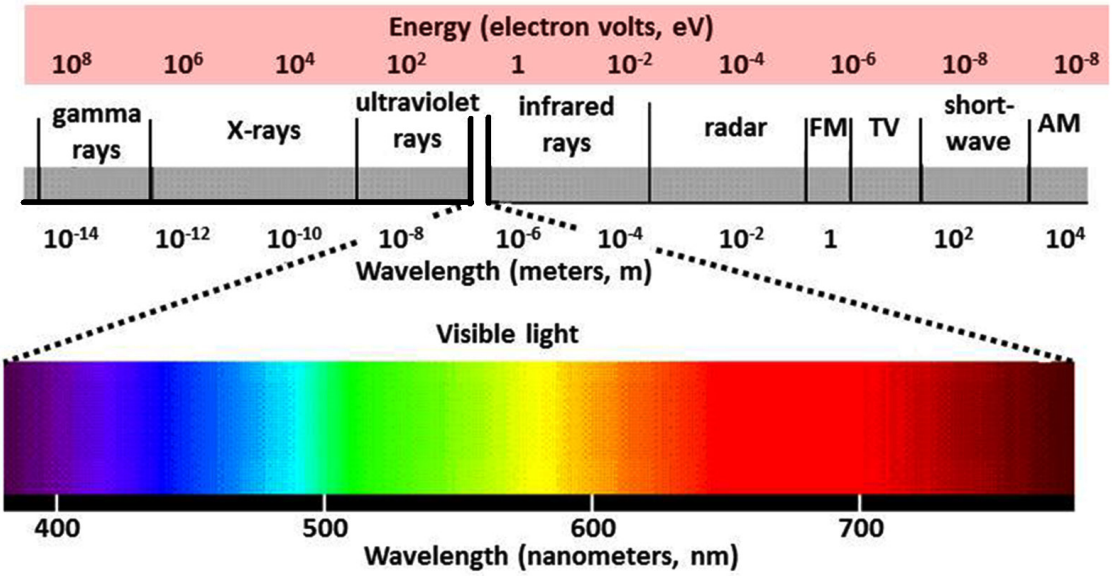

Figure 2.4: Scheme of the electromagnetic spectrum.

and confined by experimental upper limits.

The generation and attenuation of gamma-rays

Typically, gamma photons are generated in natural environments through non-thermal processes, which encompass various mechanisms:

- **Synchrotron radiation:** Ultra-relativistic electrons (or protons) accelerated spirally around the magnetic field can emit synchrotron radiation.

- **Inverse Compton scattering:** It is a phenomenon wherein an ultra-relativistic electron interacts with a lower energy photon. For instance, the photon involved might originate from synchrotron radiation emitted by electrons. During this interaction, the photon gains energy, transitioning into a gamma photon, while the electron undergoes a reduction in energy. A special situation occurs when photons emitted by synchrotron radiation are upscattered by the same electrons that produced them. This process is called Synchrotron Self-Compton (SSC).

- **Electron-positron pair production:** Through this mechanism, a photon with energy in the VHE domain can decay into an electron-positron pair. This mechanism accounts for the attenuation of gamma-rays as they propagate from the source toward Earth, a consequence of their interaction with the EBL.

- **P-gamma interactions:** In environments where the density of soft-energy photons is large, relativistic protons interact with low-energy photons and give neutral and charged pions, producing a Δ^+ resonance which immediately decays:

$$p + \gamma \rightarrow \Delta^+ \rightarrow \begin{cases} p + \pi^0 \\ n + \pi^{\pm} \end{cases} \tag{2.2}$$

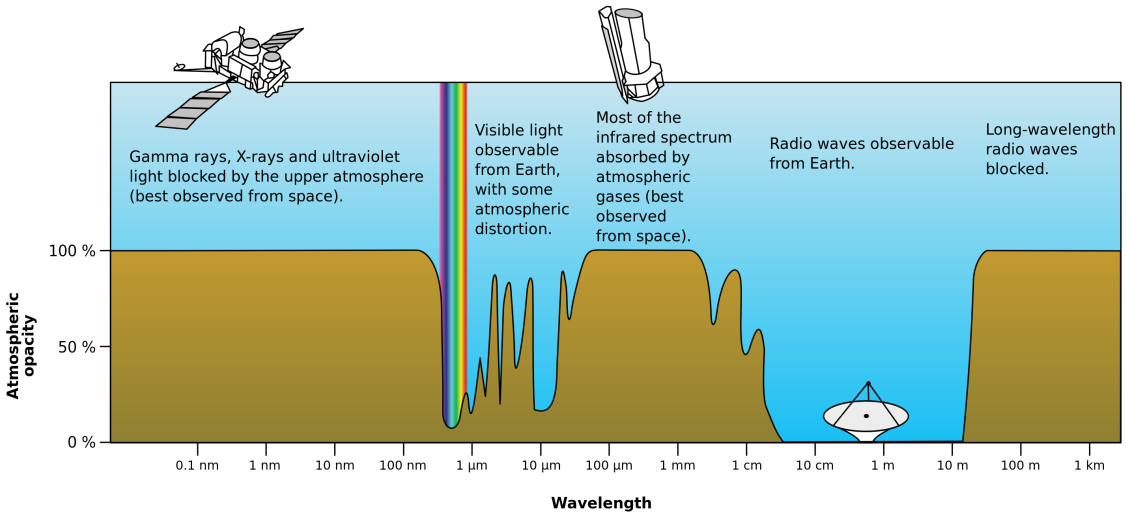

Figure 2.5: Atmospheric transparency of the Earth. Credit: NASA

Gamma photons can be generated from the decay of neutral pions:

$$\pi^0 \rightarrow \gamma + \gamma \tag{2.3}$$

It is important to note that neutrinos are also formed in this process due to the decay of charged pions, and after that, from the decay of charged muons:

$$\pi^+ \rightarrow \mu^+ + \nu_\mu \tag{2.4}$$

$$\pi^- \rightarrow \mu^- + \overline{\nu_\mu} \tag{2.5}$$

$$\mu^+ \rightarrow e^+ + \nu_e + \overline{\nu_\mu} \tag{2.6}$$

$$\mu^- \rightarrow e^- + \overline{\nu_e} + \nu_\mu \tag{2.7}$$

- **P-p interactions:** A relativistic proton can interact with a proton (or more generally with a nucleus N) from the interstellar medium, producing many unstable particles, including neutral and charged pions:

$$p + N \rightarrow \pi^{0,\pm} + K^\pm + X + ... \tag{2.8}$$

where X represents another type of nucleus and K represent kaons and ... represents the presence of higher mass mesons and baryons. Then neutral pions decay into gamma photons, charged pions decay into muons and muons decay into neutrinos, in the same way as before.

- **Bremsstrahlung radiation:** Gamma rays can be emitted from the deflection of an energetic CR caused by an electric field. In particular, deflection of UHECRs can produce VHE gamma-rays even though this radiation has never been observed so far.

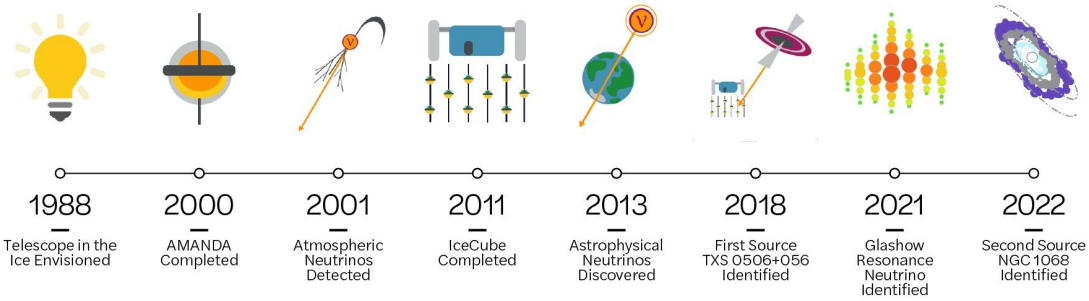

Figure 2.6: History of neutrino astronomy in Antarctica. Credit: IceCube Collaboration

2.1.3 Astrophysical neutrinos

Neutrinos are fundamental particles that, similarly to photons, have no charge and therefore give direct information about the direction of origin. For many years it was thought that they were also massless, but in 2008 it was found that they have mass different from zero, although very small [12]. They can also oscillate in different flavours [13, 14, 15]; there are 3 types of neutrinos: electron neutrinos (ν_e), muon neutrinos (ν_μ) and tauon neutrinos (ν_τ). This discovery also led to the Nobel Prize in 2015 for physicists Takaaki Kajita and Arthur McDonald. The key characteristic of neutrinos is their interaction exclusively via the weak interaction, resulting in infrequent interactions with matter. Consequently, neutrinos can traverse exceedingly vast distances without experiencing energy alterations, yet their detection remains notably challenging. For this reason, efforts have been made in recent years to use these particles to probe the far areas of the primordial universe in search of cosmological neutrinos. So far, only the following extraterrestrial neutrino sources are known: the Sun, the 1987A supernova, the neutrino background from our own galaxy, and a diffuse flux of astrophysical neutrinos (most likely generated by sources such as AGNs permeating the Universe).
For the purpose of this thesis, we focus on the study of astrophysical neutrinos, which, unlike solar or 1987A supernova neutrinos that have been detected by instruments such as Super-Kamiokande in the MeV range, have much higher energies of the order of TeV and have been measured by IceCube, for the first time, only in 2013 (Figure 2.6). Finally, in the PeV and EeV range, cosmogenic neutrinos are found, which are produced by the GZK cutoff mechanism, as discussed before.
Astrophysical neutrinos can originate from the processes outlined in Equations 2.2-2.8, involving interactions among hadrons or between hadrons and photons. The spectrum of astrophysical neutrinos typically follows a power-law distribution (refer to Figure 2.7), implying that the measurement of these neutrinos becomes progressively challenging as their energy increases.

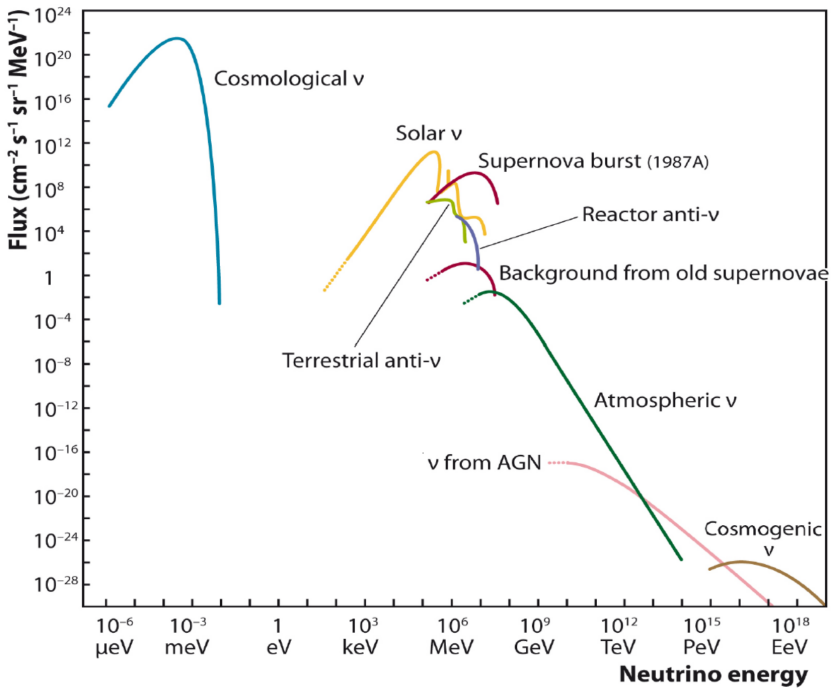

Figure 2.7: Energy flux of different types of neutrinos. Figure taken from [16].

2.2 Multi-messenger sources

Let us now delve into comprehending the interrelation among these three messengers and elucidate the significance of combining the outcomes of their observations. Gamma-ray emitters can be divided into galactic objects, such as SNRs, Pulsar WInd Nebulae (PWNs), X-ray binaries and extragalactic sources, e.g. GRBs and AGNs. These sources are not only emitters of gamma-ray photons but they also constitute optimal settings for the acceleration of charged particles, thereby favoring the genesis of CRs. Furthermore, these environments facilitate the creation of astrophysical neutrinos, thus establishing a nexus between these three cosmic messengers.
For the scope of this analysis, our attention will be directed towards AGNs, given their capacity to furnish environments capable to accelerating particles up to the utmost energies. Specifically we will focus on the subclass of AGNs known as blazars (Figure 2.8), distinguished by their main feature of possessing ultra-relativistic jets oriented towards the line of sight of observation. These unique objects offer direct insight into the mechanisms governing particle acceleration processes.

2.2.1 Blazars

The term AGN denotes bright galactic nucleus manifesting intense and persistent activity attributable to the accretion of matter onto a central Super-Massive Black Hole (SMBH). The influx of accretion material onto the black hole generates non-thermal emissions spanning a broad spectrum, ranging from radio waves to gamma rays.
The typical structure of an AGN includes several key components (see Figure 2.9). At the core of the AGN resides a SMBH (probably spinning), characterized by an immense

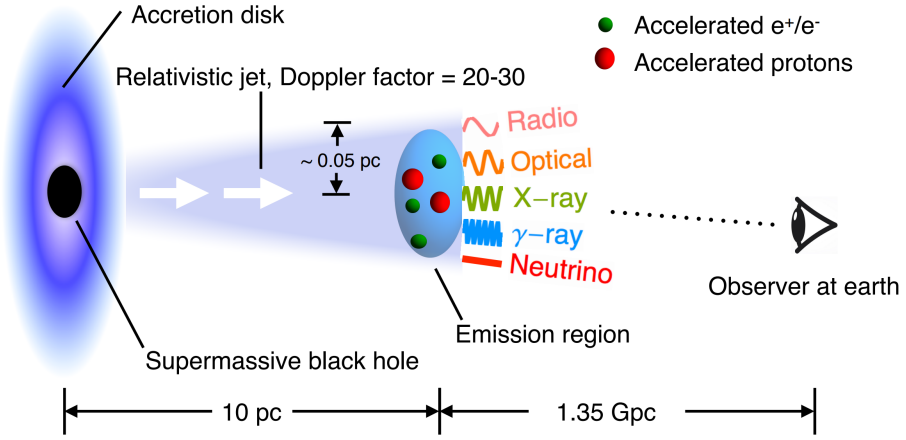

Figure 2.8: Schematic representation of a blazar. Figure taken from [17].

gravitational pull resulting from its colossal mass, between $10^6 M_\odot < M < 10^{10} M_\odot$. Surrounding the SMBH, there exists an accretion disk composed of matter drawn from the AGN's surrounding environment. This disk is where gravitational energy is converted into radiation. Its emission is thermal peaked usually in the optical-UV, more specifically its spectrum can be described by a superposition of Planckian distributions of different temperatures. The Broad-Line Region (BLR) resides in close proximity to the accretion disk, typically positioned at distances ranging from 0.01 to 1 parsec. It comprises gas clouds characterized by velocities ranging from approximately 10^3 - 10^4 km/sec and possessing a density exceeding 10^9 cm^{-3} [19]. Owing to the substantial velocities of the gas clouds, spectral lines emitted within the optical spectrum undergo broadening, a phenomenon attributed to the Doppler effect. A little further away from the central engine, there is the Narrow-Line Region (NLR), typically positioned at distances exceeding 300 parsecs. It comprises gas clouds characterized by velocities ranging from approximately 10^2 - 10^3 km/sec and possessing a density surpassing 10^3 cm^{-3}. Due to the comparatively lower velocities of the gas clouds, spectral lines observed within the optical emission spectrum exhibit narrow profiles, a consequence of the Doppler effect. The toroidal dust structure within an AGN comprises numerous optically thick clouds encircling the central region. This configuration primarily emits radiation within the infrared band, through thermal processes. Its spatial extent spans from tens to hundreds of parsecs. Finally, jets (if present) consist of ultra-relativistic plasma and are oriented perpendicular to the plane defined by the accretion disk and toroidal structures. Within these jets, charged particles undergo acceleration to velocities approaching the speed of light. Remarkably, the dimensions of AGN jets frequently surpass those of their host galaxies, spanning scales of megaparsecs. AGN jets are regarded as among the most potent particle accelerators known in the cosmos. The emissions emanating from these jets are predominantly non-thermal in nature and encompass a vast range across the electromagnetic spectrum, extending from radio wavelengths to gamma-rays.

AGNs can be categorized into two primary classifications depending on their emission characteristics in both radio and UV/optical spectra: radio-quiet AGN, characterized

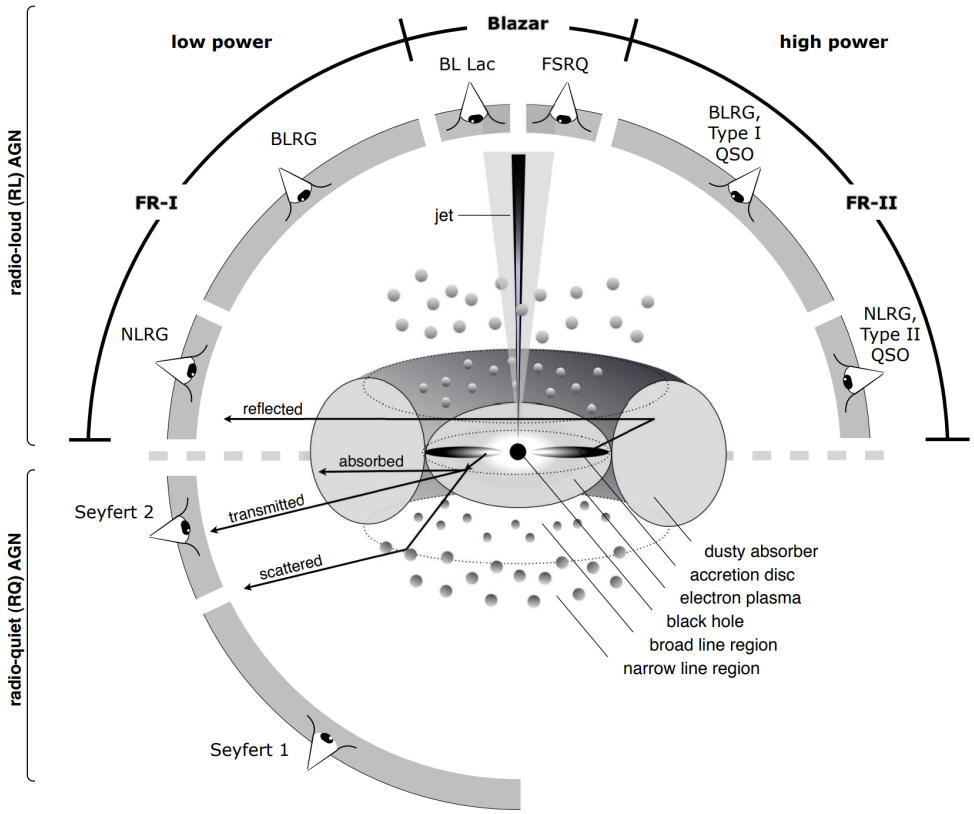

Figure 2.9: Schematic representation of an active galactic nucleus. The different classifications of AGN can be understood as results dependent on different angles of observation. Figure taken from [18].

by radio emissions at frequencies at 5 GHz that is less than the optical emission (these AGNs are typically without jets) and radio-loud AGN, characterized by radio emission at 5 Ghz bigger than the optical emission [20] (these AGNs show typically relativistic jets). Within each group, AGNs are systematically categorized based on their emission line properties (broad lines: AGN type 1, narrow lines: AGN type 2, unusual lines: AGN type 0), and based on their luminosity (Seyfert galaxies and radio galaxies at low luminosity and quasar at high luminosity), as delineated in Figure 2.10.
The classification based on different properties of AGNs appear to derive solely from variances in the observational perspective of the AGN relative to the observer (refer to Figure 2.9). Consequently, it is posited that all AGN share the same physical behavior. This framework is denoted as the unified scenario.
The classification of AGNs into type 1 or type 2 depends on the obscuration of the luminous nucleus. In addition, the classification of a radio-loud AGN as a blazar or as a radio galaxy/quasar depends on the alignment of the relativistic jet with the observer's line of sight. For example, the presence and orientation of the dusty torus assume significative importance within this framework. When the jet is observed in a lateral view, the central engine of the AGN becomes obscured. Conversely, observation from a face-on perspective, renders the accretion disk directly visible. In addition, gas clouds exert a substantial influence on delineating the emission spectrum of an AGN. Notably, the width of emission lines depends on the extent of Doppler broadening,

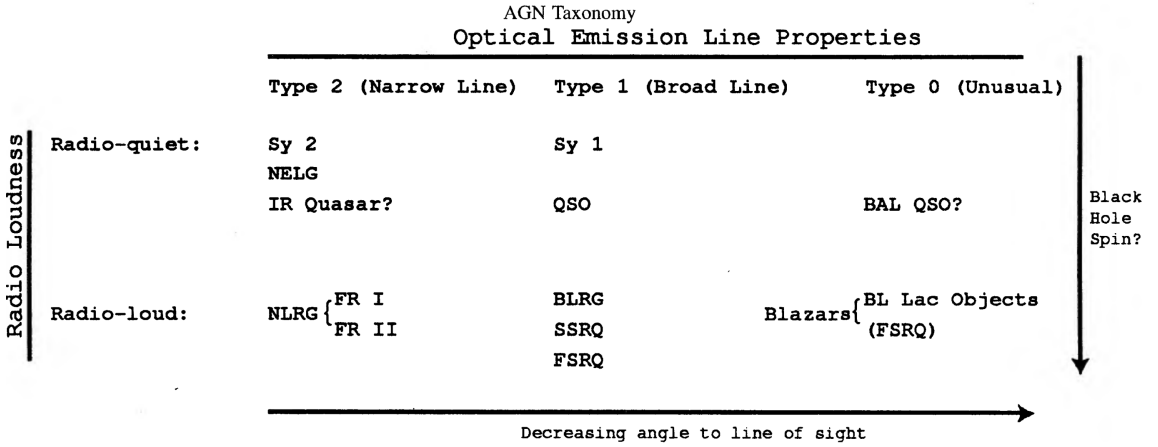

Figure 2.10: AGN classification. Figure taken from [19].

which is correlated with the distance of the gas clouds from the gravitational center. For the scope of this thesis, our attention is directed towards the classification of type 0 AGNs, which are hypothesized to maintain a small angle of inclination relative to the line-of-sight (usually $< 10°$ [21]). The term Type 0 is related to "close to 0° angle" objects [19]). These AGNs are called "blazars". Blazars are a sub-class of radio-loud quasar with relativistic jets pointing directly towards Earth. They exhibit rapid variability which spans on time-scale from years down to days (due to relativistic effects) [22] and extreme emission across the entire electromagnetic spectrum (expecially in the X-ray and gamma-ray energy ranges). Blazars are the most luminous and energetic objects known in the Universe (with a luminosity of the order of 10^{44} - 10^{48} erg/s [21]) and are one of the most powerful natural particle accelerators. The interactions of the accelerated particles generates secondary by-products such as photons and neutrinos that can be used to probe the innermost regions of their jets.
The main features of the spectrum of blazars are:

- the SED has two broad peaks;
- the spectrum is variable, at all frequencies, but especially at high energies;
- the spectrum is a power law in restricted frequency ranges;
- the variability of the spectrum is often (but not always) coordinated and simultaneous in different energy bands;
- the high energy bump of the SED increases its relevance as we increase the bolometric luminosity.

Classification

The frequency of peaks in the SED, emission lines and luminosity are the main features on which blazar classification is based. We can distinguish two subclasses of blazars:

- **Flat Spectrum Radio Quasars (FSRQs):** represent the most luminous subclass of blazars, characterized by the first peak emission occurring within the

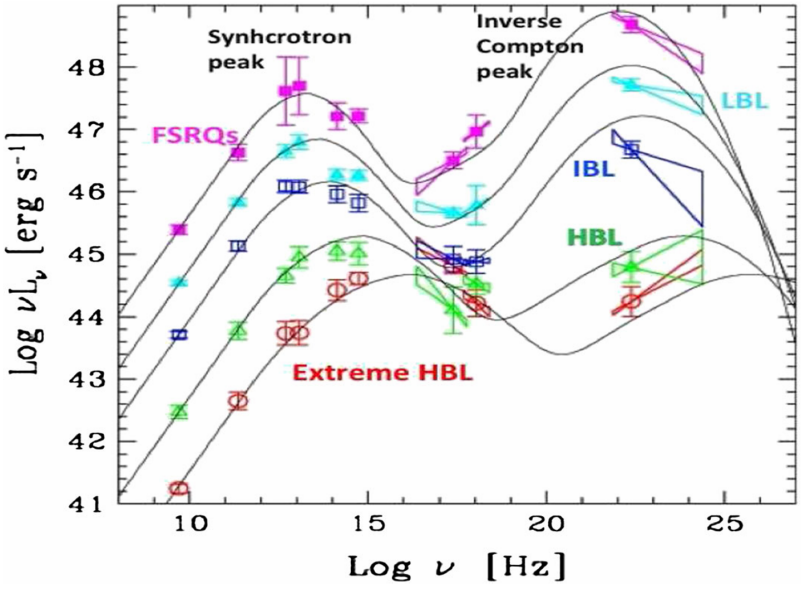

Figure 2.11: The overall spectral energy distribution of BL Lac and FSRQ blazars. It is possible to observe the variances in the relative intensities and frequencies of the two emission peaks across different types of blazars. Figure taken from [23].

infrared-optical spectrum. Notably, FSRQs exhibit strong optical emission lines indicative of their energetic nature.

- **BL Lac objects:** this class of blazars typically shows faint or non-existent emission lines and appears bluer in comparison to FSRQs, denoting higher peak frequencies for both peaks. They are further classified into four distinct categories based on the energy of their first peak: low-energy peak (LBL), characterized by a peak emission in the infrared spectrum; intermediate-energy peak (IBL), exhibits peak emission within the optical range; high-energy peak (HBL), shows peak emission in both soft and hard X-ray regimes. Extreme high-energy peak (EHBL) extend their peak emission in the hard X-ray and gamma-ray domain.

We can see the different SED characteristics of the types of blazars in Figure 2.11. This behavior is referred to as blazar sequence [24].

Emission models

The SED exhibits two non-thermal emission peaks. Existing models are able to reasonably explain the shape of the SED. However, the debate whether it is protons or leptons that give rise to the emission is still ongoing. Predicated upon the nature of these parent particles, two distinct models have emerged: leptonic model and lepto-hadronic model.
Let us begin by describing the leptonic model. The assumption used is to have a blob with a homogeneous medium with a randomly oriented magnetic field moving along the jet toward the observer. The blob is assumed to consist of relativistic electrons. In this model, the first peak of the SED (at lower energy) is due to synchrotron radiation by the relativistic electrons, while the second peak is caused by the effect of

inverse Compton scattering by relativistic electrons with low-energy photons. The place where low-energy photons come from depends on the scenario being considered. Regarding BL Lacs, usually, low-energy radiation is coming from the synchrotron photons, generating the lower energy hump itself (SSC scenario). Instead, regarding FSRQs, low-energy radiation is mainly coming from regions outside the jet, such as the accretion disk, the dusty torus or the cosmic microwave background. This phenomenon is called the external Compton scenario.
Now let us focus on the lepto-hadronic model. Even in this case, the initial peak arises from synchrotron radiation generated by relativistic electrons. Conversely, the occurrence of the second peak is attributed to the existence of an additional population of relativistic protons and the presence of an exceptionally strong magnetic field. These conditions facilitate synchrotron emission emanating from the relativistic protons.
The key feature to distinguish between the two scenarios is to conduct multi-messenger observations. In the case of the lepto-hadronic scenario, we expect the occurrence of neutrino production, which we do not expect in the leptonic scenario.
In the context of lepto-hadronic scenario, relativistic protons interact with the low-energy photon field via p-gamma interactions. This interaction generates gamma rays through the decay of neutral pions, as well as through the decay of charged pions into electron/positron pairs which, subsequently, emit synchrotron photons, leading to the production of gamma photons and a cascade effect (as shown in Equations 2.2-2.7). The cascade process stops when the internal optical depth permits gamma-rays to escape without further interaction. The resulting photons are detectable by gamma-ray satellites in space or by ground-based Imaging Atmospheric Cherenkov Telescopes (IACTs) (as we will see in Chapter 3). In principle, in a blazar, p-p reactions could also occur. However, in this ambient, the low-energy photon density significantly exceeds the particle density in the jet, therefore p-gamma reactions hold a competitive advantage. As seen before, p-gamma interactions also yield neutrino production. Consequently, the detection of a neutrino coinciding with a blazar is a smoking gun signature of hadronic-type acceleration in the source.
Figure 2.12 shows an example of SED models in the two leptonic and lepto-hadronic contexts, applied to a given blazar.

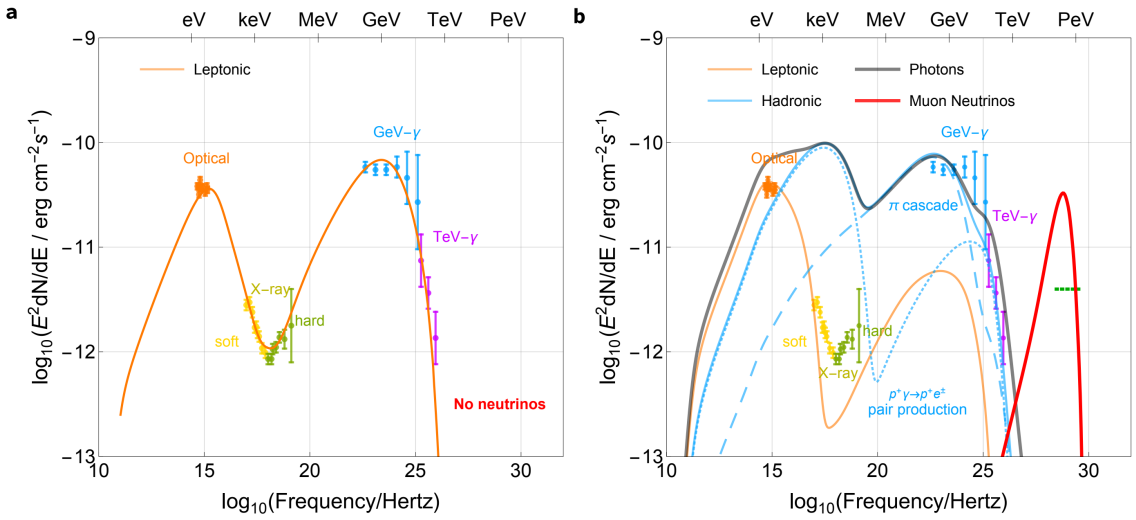

Figure 2.12: Example of SED models applied to the BL-Lac blazar TXS 0506+056. Left: Purely leptonic model. Right: Hadronic model. Figure taken from [17].

Chapter 3

HIGH ENERGY INSTRUMENTATION

As discussed in the previous chapter, since on Earth gamma-rays are shielded by the atmosphere, a direct detection of these photons is possible only through a space-based satellite. If observations are made from space, the sky in gamma rays becomes dotted with many sources located, mainly, in the galactic plane (Figure 3.1). Nevertheless, these instruments face technical challenges which limit their observational capabilities in the VHE domain and above [25]. As a result, this led to the development of different techniques which can provide indirect detection of gamma-rays from the ground.
In this chapter I will present an overview of the direct (Section 3.1) and indirect (Section 3.2) gamma-ray detection techniques, based on photon energy, focusing on the description of the instruments relevant to the purposes of this thesis, namely the Fermi Large Area Telescope (LAT) and the Major Atmospheric Gamma-ray Imaging Cherenkov (MAGIC) telescopes (Section 3.3). Finally, I will describe high-energy neutrino detection techniques (Section 3.4) focusing on the IceCube neutrino telescope.
Before proceeding with the description of instruments that can detect gamma rays, it is very important to have a look at how they are classified according to their energy [26]. The gamma range is the largest domain in the electromagnetic spectrum; therefore it covers several major detection methods: in the LE gamma-ray range Compton telescopes (in balloons or in satellites) are used; in the HE gamma-ray range Pair-creation telescopes (in satellites) emerge as indispensable instruments. Conversely, when contemplating phenomena with energy bigger than VHE gamma-ray domain, reliance on ground-based instrumentation becomes imperative. In the VHE range Imaging Atmospheric Cherenkov Telescopes (IACTs) are used, in the UHE range are employed Extensive Air Shower (EAS) arrays and, ultimately, in the EHE range atmospheric fluorescence telescopes are utilized. The performance of a detector is determined by its values in the following properties:

- **Field of view:** is the sky area that the telescope can observe at simultaneous time.
- **Angular resolution:** is the ability of the telescope to determine the direction of the incoming photon.

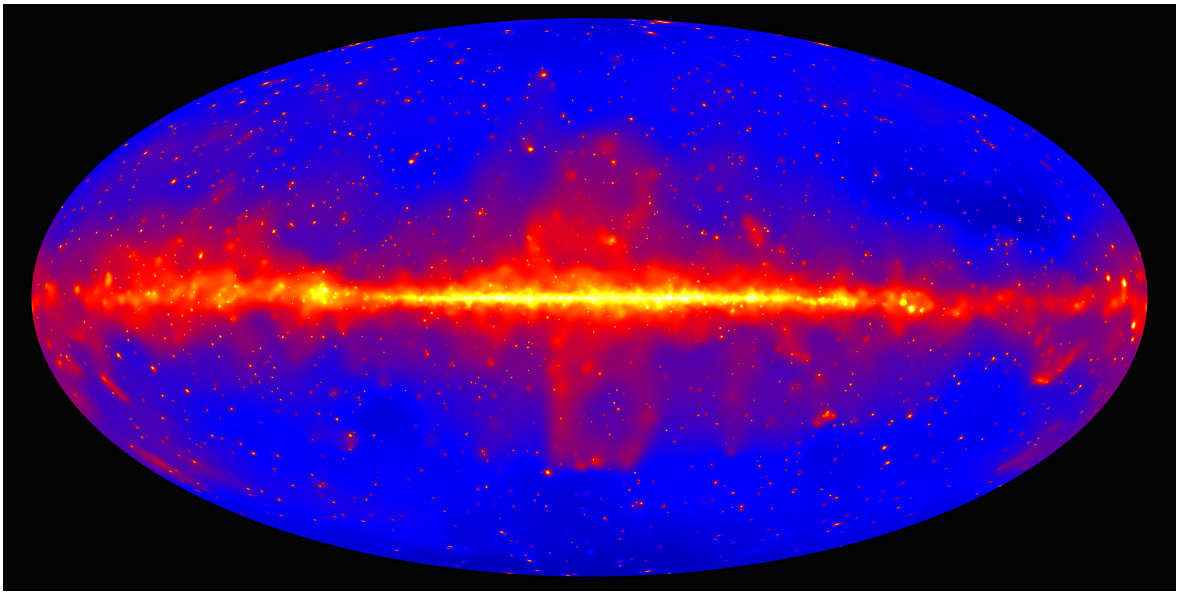

Figure 3.1: The sky map seen by Fermi-LAT. Utilizing data accumulated over a span of nine years through observations conducted by the Fermi Large Area Telescope, this map presents an overview of the gamma-ray sky. Colors from blue to yellow indicate an increasing scale in gamma flux. Credit: NASA/DOE/Fermi-LAT Collaboration.

- **Energy resolution:** is the capability of the telescope to discern the energy of the photon.
- **Duty cycle:** is the fraction of the total time effectively observed by a telescope.
- **Sensitivity:** is the minimum flux the telescope can detect, observing for a given time.

Achieving optimal values across all these properties simultaneously is presently unattainable. Consequently, it is important to combine observations from multiple telescopes exhibiting varied performance characteristics when observing the same source. This amalgamation enables more accurate estimations of the parameters associated with the studied source.

3.1 Direct gamma-ray detection techniques

To directly observe gamma photons, it is necessary to perform observations in space. In order to build telescopes capable of detecting them, it is necessary to investigate their interactions depending on the detector material (Z) and photon energy (E). Observing Figure 3.2, it becomes apparent that there exist three principal interactions:

- **photoelectric effect** (dominant at energies < 1 MeV);
- **Compton scattering** (dominant at energies ~ 1 MeV);
- **pair production** (dominant at energies > 100 MeV).

Therefore, what is conventionally done with optical telescopes, namely, the confine-

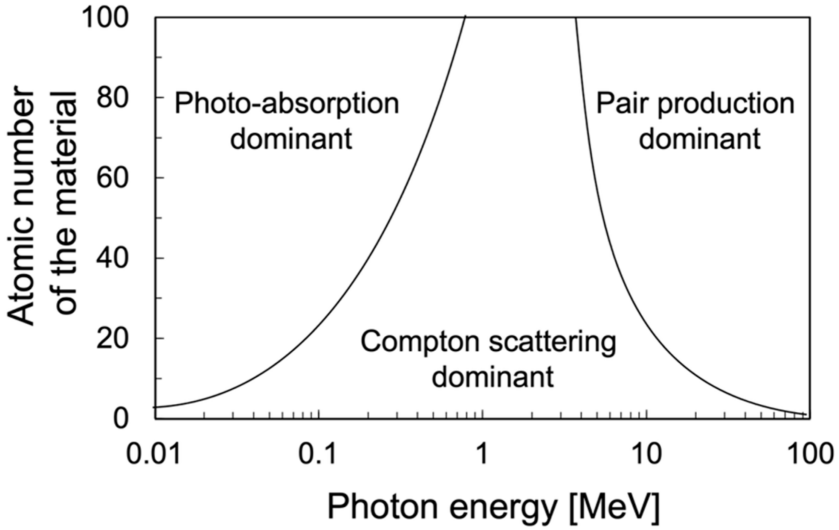

Figure 3.2: Three main types of gamma-ray interaction. The plot shows the energy (E = hν) at which photoelectric effect, Compton scattering, and pair production become dominant with respect to the atomic number (Z) of the detector material. Figure taken from [27].

ment of photons within a specific area to amplify their signal, proves unfeasible within the gamma-ray energy domain. This limitation arises due to the manner in which gamma-rays interact with detector materials, as expressed by the plot shown in Figure 3.2. Consequently, within high-energy instrumentations, the methodology revolves around measuring the charged particles generated as a consequence of these interactions. Given the charged nature of these particles, they can be readily concentrated within a defined area to facilitate the study of their properties and extrapolate information pertaining to the initial gamma-rays. The typical procedure entails the conversion of photons entering the detector into electrical signals, enabling the determination of their arrival time, direction, and energy, followed by transmission of this data to ground stations [11]. However, as detailed in Chapter 2, it is acknowledged that stray charged particles (CRs) permeate space, serving as background interference for such measurements. To mitigate this background interference, an anti-coincident (AC) shield is constructed. This shield serves to safeguard the detector by discerning the passage of charged particles from external sources and subsequently rejecting them [28].
Now let us explore the principal gamma-ray detection techniques, based on optimization depending on the energy range in consideration.

Photoelectric detectors

A LE photon primarily interacts with matter via the photoelectric phenomenon. The photoelectric effect is a phenomenon in which electrons are emitted from a material when it absorbs electromagnetic radiation. This effect occurs when photons of sufficient energy strike the material, causing electrons to be ejected. The emitted electrons are called photoelectrons, and their energy depends on the frequency of the incident photons. Subsequently, the electron traverses the medium possessing an energy equivalent to the initial photon's energy subtracted by the binding energy. Consequently,

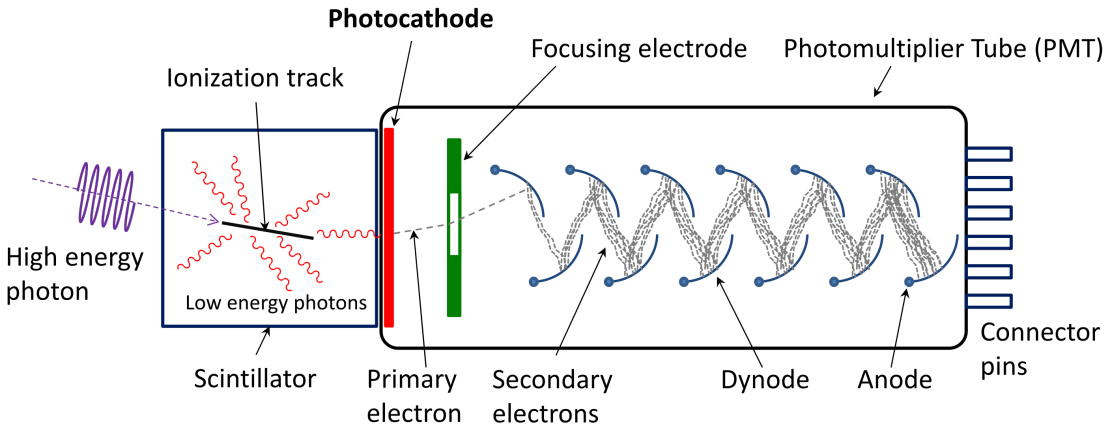

Figure 3.3: Schematic representation of a scintillation detector. Figure taken from [26].

this process generates an electrical signal, which can ultimately be detected, enabling us to deduce the original energy of the gamma-ray.
We can employ various types of detectors for this purpose. One such example is scintillator detectors (Figure 3.3), constructed from materials such as thallium-doped sodium iodide NaI(Tl) or bismuth germanate BGO, which have the capability to generate optical photons when exposed to high-energy photons. In this process, the high-energy photons excite the material, leading to the emission of optical photons through scintillation, which are then detected by photomultipliers [29]. These telescopes offer the advantage of rapid response times, making them well-suited for studying transient celestial objects. However, they suffer from limitations in angular and energy resolution. An instance of a scintillator detector is the Gamma-ray Burst Monitor (GMB), deployed aboard the Fermi satellite.

Compton detectors

Compton telescopes typically comprise two detectors: the initial encounter involves the gamma-ray interacting with the first detector, typically composed of organic liquid scintillator, via Compton scattering. Consequently, the photon undergoes scattering, altering its energy and trajectory, before reaching the second detector, typically constituted by an inorganic crystal scintillator, where it is absorbed [30]. Utilizing specialized techniques that consider the Compton cone and associated scattering formulas governing the photon's energy pre and post scattering, as well as the deflection angle, estimates regarding the direction of origin can be derived. A schematic representation of such a telescope is provided in Figure 3.4. An exemplary instance is COMPTEL [31]. Telescopes operating within this challenging energy range offer a broad field of view but exhibit lower sensitivity.

Pair production detectors

When a photon possesses energy ranging between 100 MeV and 100 GeV, the predominant interaction mechanism is pair production, particularly when employing a material with high atomic number Z. Upon entering the instrument, the photon initiates the

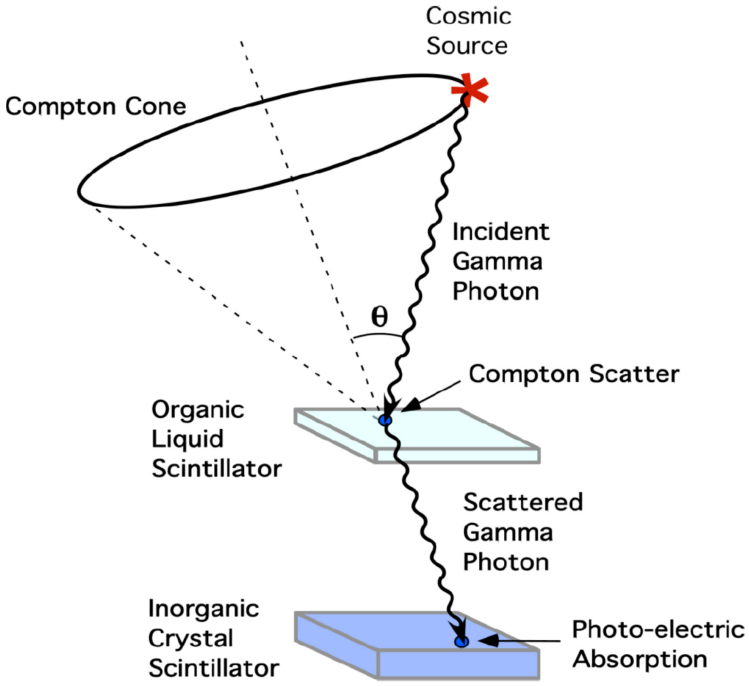

Figure 3.4: Schematic representation of a Compton detector. Figure taken from [26].

production of an electron/positron pair, the trajectories of which are subsequently monitored to measure the direction of the primary photon. A calorimeter positioned at the base is utilized to quantify the energy of the particles, thereby facilitating the determination of the primary photon's energy [32]. An exemplar of such telescopes is Fermi-LAT, which is now described in more detail.

3.1.1 Fermi Large Area Telescope

The Fermi Large Area Telescope (LAT) is a space-based instrument designed to observe gamma-rays with energies ranging from 20 MeV to over 300 GeV. Fermi-LAT is part of NASA's Fermi Gamma-ray Space Telescope mission, launched in 2008 [33]. The Large Area Telescope is formally characterized as an imaging gamma-ray telescope boasting a wide Field-of-View (FoV) and large effective area, coupled with good energy and angular resolution capabilities (see Table 3.1).
Fermi-LAT continuously monitors the gamma-ray sky for transient events and time variability in gamma-ray sources. This allows astronomers to study phenomena such as GRBs, flaring AGNs, and pulsar emissions on various timescales, from milliseconds to years.
The Fermi-LAT functions as a pair conversion detector, wherein gamma-rays traverse the detector and interact with a high atomic number (Z) converter material, notably tungsten, leading to the production of an electron/positron pair. These pairs are subsequently tracked throughout the instrument utilizing silicon strip detectors. Due to the considerably higher energy of gamma-rays compared to the rest mass of the electron and positron, both constituents of the pair predominantly maintain their trajectory in alignment with the incident gamma-ray. Consequently, the reconstructed direction of the incoming gamma-ray is primarily constrained by the multiple scatterings of the

Parameter	Value/Range
Energy Range	20 MeV to 300 GeV
Energy Resolution	$< 15\%$ for E $>$ 100 MeV
Effective Area	> 8000 cm^2
Field of View	2.4 sr

Table 3.1: Main characteristics of Fermi-LAT [8].

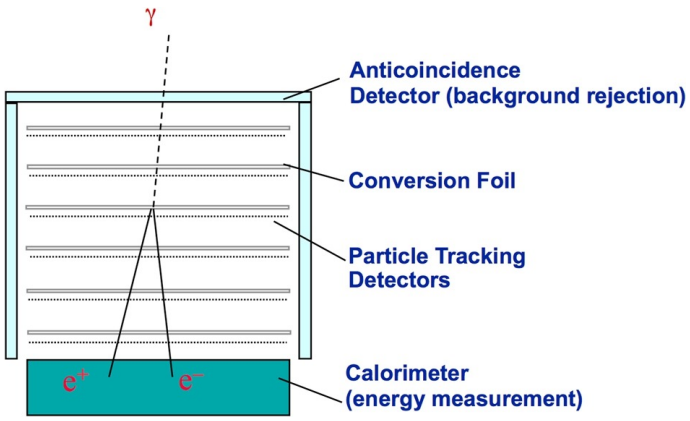

Figure 3.5: Schematic representation of Fermi-LAT. Figure taken from [35].

pair components within the tracker material, as well as the spatial resolution of the tracker itself.
A calorimeter composed of thallium-doped cesium iodide CsI(Tl) is positioned at the base of the LAT, which possesses sufficient thickness to afford accurate energy measurements of the pairs within the LAT's designated energy band. In addition, it is also present an AC detector, to shield the telescope from CRs. The LAT produces signals when charged particles interact with its tracker and calorimeter, depositing energy in specific regions. From the position of these pulses, the trajectory and the energy losses of the particles can be reconstructed [34]. Through analyses conducted both onboard and on the ground, it is possible to reconstruct the tracks of charged particles. This process allows for the identification of the interaction that gave rise to the charged particles. Moreover, it facilitates the differentiation between events originating from photons and background noise, as well as the determination of the incident photon direction and the estimation of energy levels.

3.2 Indirect gamma-ray detection techniques

As previously demonstrated, the direct detection of HE photons from ground is not possible. Moreover, for direct detection of VHE photons, the construction of space-borne instruments suitable for their detection is unfeasible. This limitation arises due to the extremely low flux of such photons, necessitating instrument areas that exceed practical limits for deployment in space [36]. The underlying physical reason behind the low flux of photons with energies >VHEs can be attributed to the following primary factors:

- The gamma-ray spectrum follows a power law, wherein the flux diminishes with escalating energy levels, both within the hadronic and leptonic contexts.

- Photons originating from the EBL and Cosmic Microwave Background (CMB) induce absorption effects on the most energetically photons.

Hence, the only possible approach for the detection and analysis of VHE photons entails the construction of ground-based instruments capable of indirectly detecting them.
When entering into the atmosphere, these photons interact with atmospheric particles, giving rise to a cascade known as Extensive Air Showers (EAS) comprised of secondary particles. From these secondary particles it is possible to deduce information about the primary gamma-ray. In such methodologies, the atmosphere serves as an integral component of the detector. Nevertheless, executing this methodology is not without complexities. Gamma-rays are not the exclusive generators of EAS; CRs also generate EAS phenomena. Given the greater abundance of CRs compared to gamma-rays, they introduce significant noise into the observation. Hence, it becomes imperative to investigate the distinguishing characteristics between the two types of EAS: those arising from gamma-rays (referred to as electromagnetic showers) and those coming from CRs (referred to as hadronic showers). Such differentiation enables the mitigation of background noise and facilitates accurate gamma-ray detection and analysis.

3.2.1 Electromagnetic Extensive Air Showers

Let us clarify the manner in which a photon can collide with a target material, which, in our context, refers to the atmosphere. As previously shown in Figure 3.2, it is established that a VHE photon primarily undergoes pair production. Upon entry into the atmosphere, a VHE photon interacts with a nucleus, thereby generating an electron and a positron. Subsequently, these highly energetic particles can undergo further interactions, emitting photons via Bremsstrahlung mechanism, initiating a EAS. Describing the general scenario of electromagnetic EAS entails inherent complexity. Notably, the mean free path of photons, electrons, or other particles generated depends on the atmospheric density, rendering it a variable parameter in both temporal and spatial dimensions. Furthermore, Bremsstrahlung photons emitted by each electron/positron pair can be multiple, thus adding complexity to the electromagnetic EAS modeling. Nevertheless, it is feasible to conceptualize the process in a simplified manner by employing the Heitler's model [37]. Before explaining Heitler's model it is necessary to introduce the main quantities that define a shower:

- **Energy of the primary particle:** The energy of the primary particle E_0 is the initial energy of the particle that induces the shower. In the case of electromagnetic showers this particle may be a gamma-ray, electron or positron.

- **Atmospheric depth:** The atmospheric depth X is a measure of the thickness of the atmosphere along the path traversed by a particle. It is often expressed in units of grams per square centimeter (g/cm^2). It provides a measure of the amount of material a particle encounters as it travels through the atmosphere.

The atmospheric depth X can be calculated using the formula:

$$X = \int_0^h \rho(h')\, dh' \tag{3.1}$$

where $\rho(h')$ is the atmospheric density, h' is the altitude at which the particle is located. Practically, the atmospheric depth is often tabulated for various altitudes and locations, allowing researchers to estimate the depth of the atmosphere encountered by particles of interest during their propagation through the Earth's atmosphere.

- **Radiation length:** The radiation length X_0 represents the mean distance over which a high-energy electron (or positron) or photon loses a significant fraction (approximately 63.2%) of its energy due to bremsstrahlung radiation or pair production in a medium. The radiation length is determined by the atomic and electronic structure of the material and is given [38] by:

$$X_0 = \left[4\alpha r_e^2 \frac{N_A}{A} Z^2 \ln(183 Z^{-1/3})\right]^{-1} \tag{3.2}$$

where α is the fine structure constant, r_e is the classical radius of the electron, Z is the atomic number, A is the atomic mass number and N_A is the Avogadro number. If the primary particle is an electron or positron, ${X_0}^e = 36.7$ g/cm^2 [39]. If the primary particle is a photon: ${X_0}^\gamma = \frac{7}{9}{X_0}^e$. The relationship between the atmospheric depth X and the radiation length X_0 can be expressed in terms of the number of radiation lengths n traversed by a particle through a medium:

$$X = nX_0 \tag{3.3}$$

- **Critical Energy:** The critical energy E_c is defined as the energy threshold at which the shower development stops. When secondary photons reach the critical energy (E_c), they predominantly undergo interactions such as Compton scattering or photoelectric absorption, thereby impeding further development of the cascade. Similarly, for electrons or positrons, energy loss via ionization processes becomes predominant at energies near the critical energy. In dry air at standard atmospheric pressure (1 atmosphere), the critical energy is $\sim$ 87 MeV.

- **Depth of the shower maximum:** The depth of the shower maximum X_{max} refers to the depth of the atmosphere at which an EAS reaches its maximum density of secondary particles. This depth is a crucial parameter in the study of air showers as it provides valuable information about the characteristics of the primary particle.

In the framework of Heitler's model for the description of the electromagnetic shower, the following assumptions are made [40]:

- Electron and photon radiation length are equal: ${X_0}^\gamma = {X_0}^e$;
- X_0 remains independent of the energy of the primary particle (E_0);

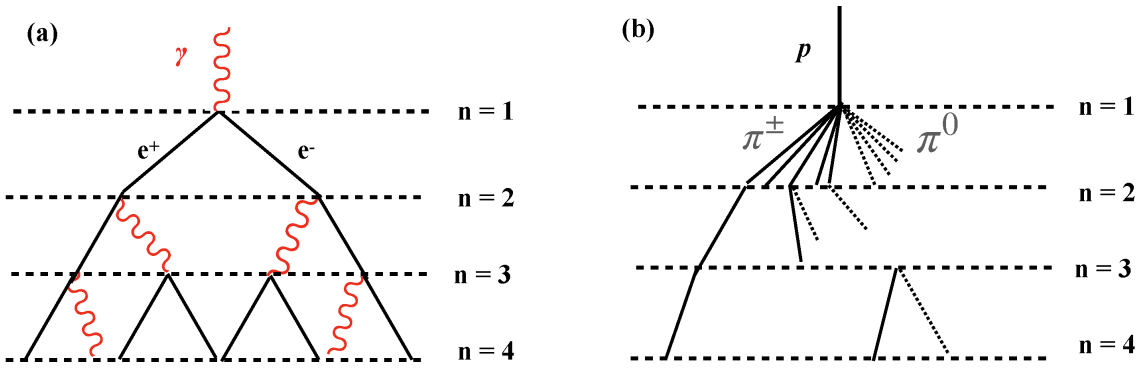

Figure 3.6: Heitler model of Extensive Air Showers. Left: Electromagnetic shower. Right: Hadronic shower. Figure taken from [40].

- the processes involved are pair production and Bremsstrahlung; ionization and excitation effects are neglected;
- omit the scenarios of multiple electron/positron pairs generated by the incident photon, and neglect the emission of multiple Bremsstrahlung photons from the electron-positron pair;
- the energy E_0 is evenly distributed following the creation of each new secondary particle, represented as $E_N = \frac{E_0}{N}$, where N is the total number of particles created in the shower and it is equal to 2^n, where n is the radiation length.

A schematic representation of the longitudinal development of an electromagnetic shower following Heitler's model is illustrated in Figure 3.6. Suppose a photon (the analogous scenario holds for an electron or positron) with energy E_0 penetrates the atmosphere. Upon traversing a certain radiation length denoted by X_0^γ (where n=1), it interacts with an atmospheric nucleus, generating an electron-positron pair. These particles divide the initial energy, resulting in $E_0/2$ for each. Subsequently, each particle emits a Bremsstrahlung photon (where n=2) with an energy of $E_0/4$. This multiplication process iterates until the energy E_N equals the critical energy E_C. At this point, the shower development attains its maximum ($X=X_{max}$) and the secondary particles experience a significant loss of energy, terminating the shower's progression. The maximum number of particles is approximately equivalent to E_0/E_C. Assuming $E_0 = 1$ TeV, the estimated number of particles produced is of the order of 10^{10} [41]. This quantity of particles within a shower is commonly defined as the "shower size". The altitude above sea level at which this criterion is met is denoted as the height of the maximum shower (H_{max}). It exhibits an inverse relationship with the logarithm of the energy of the incident primary gamma ray. Consequently, exceedingly energetic gamma-rays penetrate deeper into the atmosphere. Heitler's model demonstrates the ability to accurately replicate the longitudinal progression of EM showers. Nonetheless, it is constrained by the assumptions discussed previously. To attain a more faithful description of the shower phenomenon, recourse to Monte Carlo simulations becomes necessary.

3.2.2 Hadronic Extensive Air Showers

The effort to model the hadronic showers is challenging due to the nature of their development, characterized by the production of many different types of particles including pions, neutrinos, muons, electrons/positrons, and photons. The development of the hadronic shower can be summarized as follows.
When a CR penetrates the Earth's atmosphere, it interacts with atmospheric nuclei, resulting in the production of a significant nuclear fragment alongside numerous pions (both charged and neutral) and a portion of kaons. Approximately half of the energy carried by the primary CR is transferred to the secondary particles generated in the collision, while the remainder is divided to the nuclear fragment, often referred to as the "leading particle". It is notable that, in terms of quantity, the population of positive, negative and neutral pions are roughly equivalent to each other [11, 42]. Afterwards, neutral pions undergo decay into VHE photons, which subsequently initiate electromagnetic sub-showers:

$$\pi^0 \longrightarrow \gamma + \gamma \tag{3.4}$$

The charged pions and kaons subsequently undergo further interactions with atmospheric nuclei, or with the leading particle, resulting in the generation of additional sub-particles consisting of both neutral and charged pions, as well as kaons. This cascade of interactions leads to the initiation of successive electromagnetic sub-showers, perpetuating the process iteratively. As the count of particles within the cascade escalates, the energy per individual particle diminishes accordingly. Consequently, particles disperse, undergoing energy dissipation, with many particles diverging from the cascade. The particle count attains a maximum at a specific depth X_{max}, which is dependent upon the energy, the primary particle's characteristics, and the particle interactions within the cascade. This phenomenon corresponds to the point at which the particle's energy equals the critical energy. After that, the energy per particle undergoes such degradation that energy losses replaces the process of particle multiplication. At a certain point, even the charged pions and kaons attain a sufficiently diminished energy level, prompting their decay into muons and neutrinos, in accordance with the following equation:

$$\pi^+ \longrightarrow \mu^+ + \nu_\mu \tag{3.5}$$

$$\pi^- \longrightarrow \mu^- + \overline{\nu_\mu} \tag{3.6}$$

The resulting muons proceed in their trajectory towards the Earth's ground. The progression of the muon cascade continues to expand and achieves its culmination, with a slower decay rate attributable to the relative stability of muons and less energy loss through processes such as ionization and pair production. Finally, muons undergo decay into electrons/positrons and neutrinos.

$$\mu^+ \longrightarrow e^+ + \nu_e + \overline{\nu_\mu} \tag{3.7}$$

$$\mu^- \longrightarrow e^- + \overline{\nu_e} + \nu_\mu \tag{3.8}$$

It is possible to construct a model for a proton-induced shower (applicable in a majority of cases, considering that CRs predominantly consist of protons) by employing the Matthews approach [41]. A representative schematic illustration is depicted in right

Figure 3.6. Various distinctions can be used to distinguish hadronic and electromagnetic showers [40]:

- The hadronic interaction length is larger: if we consider a proton in air $X_0^p = 80$ g/cm^2, therefore hadronic showers begin deeper in the atmosphere.
- Hadronic showers evolve at a notably faster pace compared to the electromagnetic scenario.
- After the initial interaction, only a portion of the primary energy E_0 is allocated to the generation of secondary particles, denoted by the parameter k, referred to as inelasticity. Specifically, $\frac{2}{3}kE_0$ is utilized in the production of N_{ch} charged pions, while $\frac{1}{3}kE_0$ remains available for the formation of neutral pions, thereby constituting the electromagnetic component.
- The critical energy E_c is defined as the energy below which charged pion decays dominate.
- The transverse development of the hadronic shower occurs in a much more dispersive manner than that of the electromagnetic shower.
- There exists a disparity in the temporal evolution of the showers: those initiated by gamma-rays can progress to completion in under 3 nanoseconds, whereas those instigated by hadrons require more than 10 nanoseconds.

As we will see, due to these distinctions, IACTs can effectively discriminate gamma photons from the predominant isotropic cosmic background by analyzing the morphological features of the showers.

3.2.3 Imaging Air Cherenkov Telescopes

The indirect method employed for the investigation of gamma-rays within the energy range spanning from GeV to TeV is the imaging technique. This methodology relies on the examination of Cherenkov radiation emitted by atmospheric nuclei during EAS, triggered by the passage of secondary particles through the atmosphere. By analyzing this radiation, significant features of the primary particle that initiated the shower, including its type, energy, and trajectory can be derived.

Cherenkov Radiation

For a particle to emit Cherenkov radiation, it must satisfy the following criteria:

- the particle must possess an electric charge;
- the velocity (v) of the particle must surpass the phase velocity of light in the medium (c/n), where "n"represents the refractive index of the medium through which the particle is traversing.

Therefore, when a charged particle moves through a dielectric medium, such as air, at a speed greater than the speed of light in that medium, the particle undergoes asymmetric polarization along its trajectory, and by disturbing the electromagnetic field of the medium, it causes the emission of electromagnetic radiation in the form of

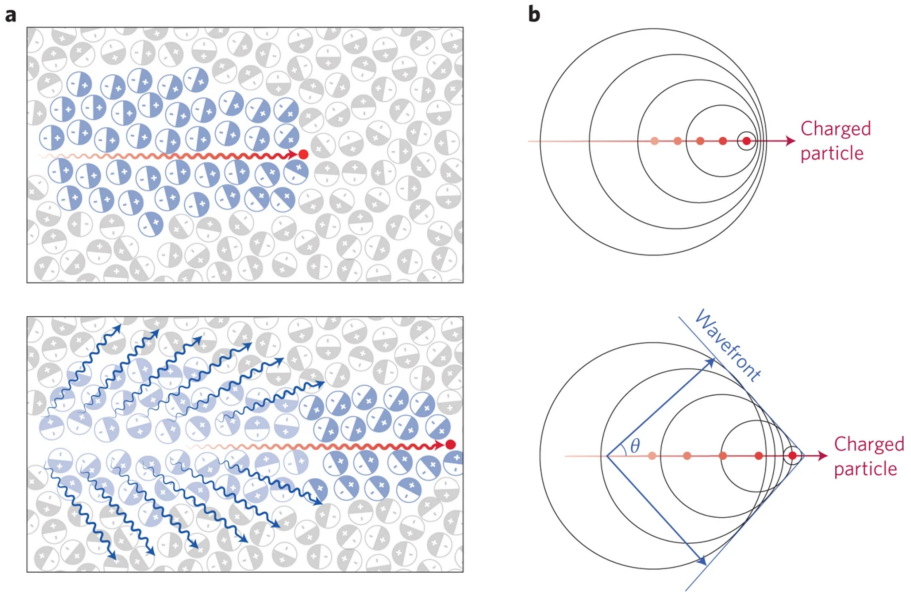

Figure 3.7: Cherenkov emission mechanism. A: When a charged particle (illustrated by the red dot) traverses a medium at a velocity exceeding that of light, the medium undergoes polarization. B: Upon relaxation to its ground state, blue-light emission occurs in a forward direction. Analogous to a sonic boom, coherent waves are generated via the Cherenkov effect, culminating in the formation of a photon wavefront. As the particle progresses forward, the photon wavefront propagates at an angle θ in the forward direction, resulting in light emission aligned with the particle's trajectory. Figure taken from [43].

photons (Figure 3.7). This emission, called "Cherenkov Radiation"[44], occurs along the path of the charged particle and forms a cone of radiation, known as Cherenkov cone, usually of the order of about 1 degree for air. The emission generated is in the range from 300 to 600 nm (optical/UV). The angle of the Cherenkov cone, θ, is determined by the particle's velocity (β = v/c) relative to the speed of light in the medium, according to the equation [45]:

$$cos\theta = \frac{1}{\beta n(\lambda)} \tag{3.9}$$

The emission of Cherenkov radiation is isotropic in the rest frame of the particle, resulting in a cone of light spreading out in all directions around the particle's path. The opening angle of the cone depends inversely on the particle's velocity, with faster particles producing narrower cones. Consequently, electrons and positrons, which are typically the fastest particles in an EAS, produce the most intense and focused Cherenkov cones. Generally, Cherenkov photons exhibit a propensity to disperse extensively, delineating a circular region with an approximate diameter of 300 meters when situated at an altitude of 2200 meters. The density of Cherenkov photons at ground level fundamentally depends upon three principal factors:

- **Energy of the primary particle:** As the energy of the primary particle escalates, the diameter of the Cherenkov cone becomes smaller, leading to an increase in its density due to the increased emission of photons.

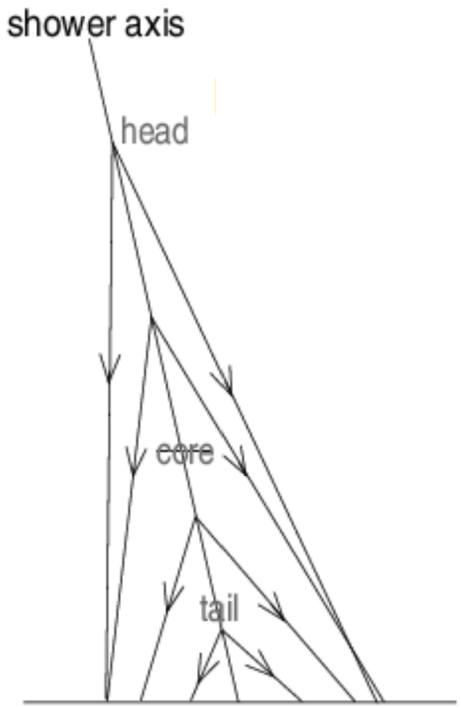

Figure 3.8: Schematic representation illustrating the variation of the Cherenkov emission angle at different altitudes within an atmospheric shower [26].

- **Zenith angle:** For larger zenith angles, the Cherenkov photons emitted necessitate traversing a greater atmospheric distance before reaching the telescope. Consequently, their density diminishes, while the diameter of the cone enlarges.
- **Telescope altitude:** Electrons within the EAS emit Cherenkov light at varying altitudes (h). Therefore, the accurate model for deducing the Cherenkov light triggered by electrons must encompass atmospheric fluctuations as h undergoes alteration. Assuming that the atmospheric density ρ is represented by the equation:

$$\rho = \rho_0 \exp -h/h_0 \tag{3.10}$$

  where $h_0 = 7.1$ km is the scale–height, and $\rho_0 = 0.0013$ g/cm^3 is the air density at sea level. It can be inferred that with an increase in altitude, the diameter of the Cherenkov cone ascends, reaching a peak at heights ranging between 10 and 20 kilometers [26]. Correspondingly, the density of Cherenkov photons also undergoes a concurrent increase. Moreover, as illustrated in Figure 3.8, it becomes apparent that the contribution of light from the shower tail is characterized by larger θ angles, therefore a shorter distance from the ground. Consequently, the diameter of the Cherenkov cone is reduced.

Furthermore, as depicted in Figure 3.9, it is observed that the emission spectrum experiences attenuation within the atmosphere. Given that the majority of Cherenkov photons are emitted at altitudes within the range of 10-20 kilometers, before they reach the IACTs, typically situated at an altitude of 2000 meters, a portion of these photons undergo absorption by the atmosphere.

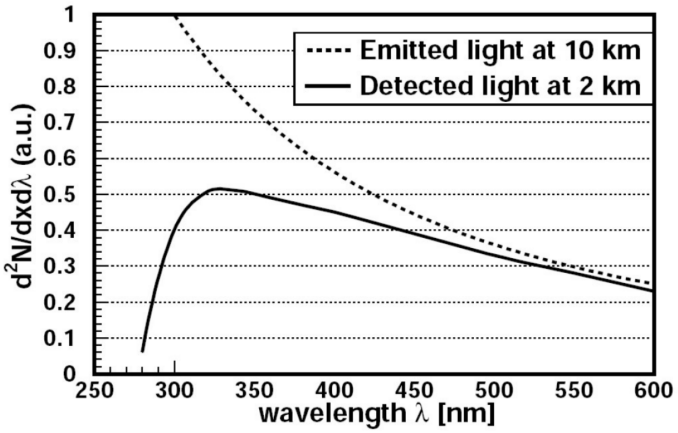

Figure 3.9: The impact of atmospheric absorption on Cherenkov light. Figure taken from [26].

Imaging Atmospheric Cherenkov Telescopes

IACTs represent sophisticated Cherenkov telescopes engineered to indirect detect VHE gamma-rays from Earth, leveraging the atmosphere as an integral component of the detection apparatus. The method used by IACTs is called imaging technique. When a VHE photon enters into the atmosphere, it initiates the formation of an EAS, resulting in the emission of Cherenkov light by atmospheric nuclei. IACTs are designed with the goal of capturing the maximum extent of Cherenkov emission caused by these secondary particles, with the aim of extracting spatial and temporal information of the primary event, thereby deriving information about the nature, energy and direction of the incident gamma ray [46]. In essence, the apparatus comprises:

- **Large reflectors:** a sizable segmented mirror used to reflect Cherenkov light onto an array of photomultiplier tubes or silicon photomultipliers (SiPM), thereby optimizing photon collection efficiency.
- **Rotating structure:** a rotating structure is essential for the tracking of candidate gamma-ray emitters.
- **Rapid electronic systems:** it is imperative for these instruments to be equipped with very fast response pixels, because of the rapid development of the showers, occurring within nanosecond timescales.
- **Trigger systems:** this system plays a key role in the discrimination and separation of background events; it is designed to selectively register "events"solely when adjacent pixels surpass a predetermined threshold within a brief temporal window.

Moreover, employing an array of such telescopes, positioned in proximity to one another, confers several advantages including enhanced sensitivity and background subtraction, as a result of a more accurate estimation of both energy and direction of the primary event. This is called **stereoscopic technique** and it allows the three-dimensional reconstruction of the shower, as depicted in Figure 3.10.

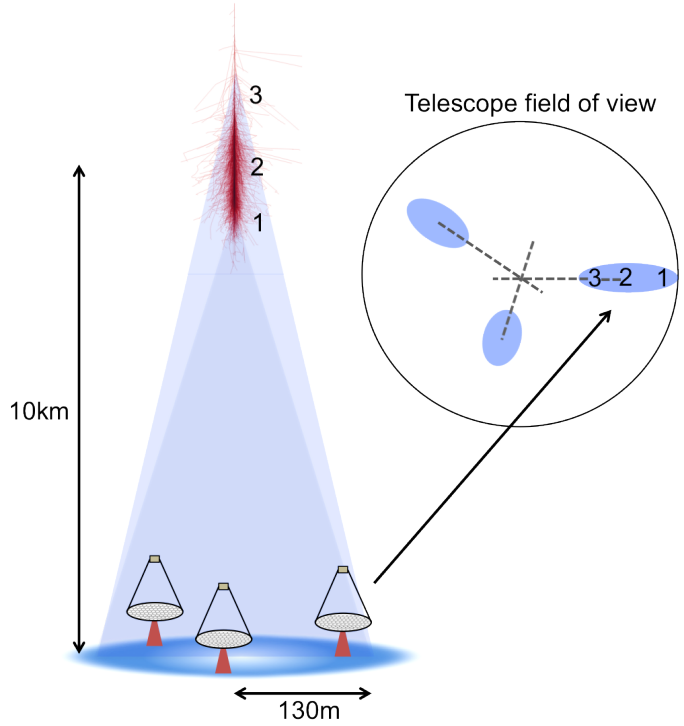

Figure 3.10: Scheme illustrating the principles of the stereoscopic technique in IACTs. Figure taken from [46].

Cherenkov photons exhibit a distribution pattern resembling an elliptical shape, with its extremities representing the head and tail of the shower, and the inner pixels corresponding to the core of the shower. The elliptical image can be characterized by a defined set of parameters, named image parameters, facilitating interpretation of the primary particle.
Several challenges may arise in the operation of IACTs, including:

- **Effect of sky conditions:** IACTs necessitate dark environments for optimal performance as Cherenkov light becomes undetectable under illuminated conditions, thereby restricting their operational window. For this reason, the Cherenkov radiation is susceptible to interference from the Night Sky Background (NSB), such as those originating from the moon, stars, or light pollution.
- **Hadronic background:** Hadronic showers and individual muons naturally cause Cherenkov emissions, which contribute to background noise in observations.

To mitigate these challenges, observation sites with minimal light pollution and observations on moonless nights are necessary. Moreover, data analysis procedures are devised to address these issues comprehensively. Discriminating against the very large hadronic background (the ratio of gamma-rays to CRs is very small, $\sim 10^{-4}$) involves the consideration of the different properties that characterize hadronic showers from electromagnetic showers, using these distinctions to identify and exclude hadronic events from analysis. Furthermore, muons generate a characteristic ring image, facilitating their differentiation from other sources of background noise.

Figure 3.11: The MAGIC telescopes at the Roque de Los Muchachos Observatory in La Palma. Credit: Giovanni Ceribella.

Currently, there are four operational IACT experiments: the High Energy Stereoscopic System (H.E.S.S.) [2], in Namibia; MAGIC [47] and the First G-APD Cherenkov Telescope (FACT) [48], in La Palma; the Very Energetic Radiation Imaging Telescope Array System (VERITAS) [49], in Arizona.
Furthermore, since 2018, a new telescope has commenced observations from La Palma in the Canary Islands, catering to these energy bands. This telescope marks the inaugural prototype, known as LST-1, of the Cherenkov Telescope Array (CTA) project [50]. The CTA project is planned to comprise over 100 telescopes, categorized into three distinct types: the Large Size Telescopes (LST) with a diameter of 23 meters, the Medium Size Telescopes (MST) with a diameter of 12 meters, and the Small Size Telescopes (SST) measuring 5 meters in diameter. These telescopes will be positioned in two astronomical sites: one located in the northern hemisphere in La Palma and the other situated in the southern hemisphere in Chile.

3.3 The MAGIC telescope system

The MAGIC Telescopes represents a stereo system of IACTs situated at the Roque de los Muchachos Observatory in La Palma, in Canary Islands, positioned at an altitude of approximately 2200 meters. The MAGIC collaboration comprises contributions from multiple nations. The inaugural MAGIC telescope was constructed in 2004 and operated autonomously for a period of five years. Subsequently, in July 2009, the second MAGIC telescope (MAGIC-II) commenced data collection, positioned at a distance

Figure 3.12: Camera and mirror images of MAGIC telescopes. Left: Foreview of the camera. Right: Individual segments of the mirror.

of 85 meters from the first. The MAGIC telescopes can also perform observations under moon-light conditions, enhancing the duty cycle up to 40% compared to exclusive dark night observations. This extended operational window facilitates improved temporal coverage, a factor of particular significance for the investigation of transient phenomena such as flares originating from AGNs, GRBs, or the follow-up observations of neutrinos and gravitational waves.

3.3.1 Structure, readout and trigger systems

The MAGIC telescopes, designated as MAGIC I and MAGIC II (refer to Figure 3.11), share a similar structural configuration, comprising a camera, a reflector, and a supporting structure.
The **structure** is characterized by its rigidity and lightweight design, weighing less than 20 tons. Constructed predominantly from carbon fiber materials, this configuration facilitates swift and agile movement of the telescope.
The **reflector** (right Figure 3.12) possesses a parabolic shape with a diameter of 17 meters, ensuring a Point Spread Function (PSF) of less than 10 millimeters [51].
Each **camera** accommodates 1039 UV light-sensitive Photo-Multiplier Tubes (PMTs). The camera (left Figure 3.12) is shielded from environmental elements by a Plexiglas window, while movable covers provide protection from sunlight and other external agents. The signals captured by the PMTs undergo initial conversion into optical signals before being transmitted to the Counting House (CH). Within the CH, essential components including the trigger, the readout electronics, and the Data AcQuisition (DAQ) system are accommodated. Here, the electrical signal undergoes bifurcation into distinct branches: the trigger branch and the readout branch. In the trigger branch, the signal traverses through a sequence of hierarchical levels.
The **trigger system** serves as a mechanism for the selective identification, based on predefined criteria, of events deemed suitable for analysis, while disregarding those that fail to meet the requirements. Within the framework of the MAGIC observatory, this system is structured into three levels denoted as L_0, L_1, and L_3:

- **L_0:** Operates individually for each telescope and accepts pixels registering a

charge exceeding a predefined threshold. This threshold is determined through the utilization of a tool known as Individual Pixel Rate Control (IPRC), a software tool capable of adjusting the threshold based on external factors such as lunar illumination levels. For instance, during a full moon, an increased number of event triggers are anticipated, prompting the IPRC to elevate the trigger level energy threshold accordingly.

- **L_1:** Identifies events from L_0 that occur concurrently and are spatially proximate.
- **L_3:** Searches for temporal coincidence by comparing events detected in L_1 for MAGIC I with those in L_1 for MAGIC II, which are situated approximately 80 meters apart. This comparison takes into account the time differential, dependent upon the direction of pointing, for the shower to reach the different positions of the two telescopes.

In the **Readout System**, the Domino Ring Sampler version 4 (DRS4) serves as the intermediary, storing the signal while awaiting the trigger decision. Following the trigger response, the accumulated charge is digitized by an Analog-to-Digital Converter (ADC), after which the data are retrieved by the DAQ.
The MAGIC telescopes are equipped with two alternative trigger systems aimed at enhancing performance at lower energies: the Sum Trigger [52] and the Topo Trigger [53]. These triggers facilitate the inclusion of additional events and atmospheric showers, consequently lowering the energy threshold.

3.3.2 Atmospheric Monitoring Instruments

Observations are frequently influenced by meteorological conditions; hence, it is important to deploy instrumentation capable of monitoring atmospheric parameters. This is particularly crucial in discerning the presence of clouds in the atmosphere, given their propensity to absorb Cherenkov light. The quality of the atmosphere exerts influence on the measured Cherenkov radiation through two distinct mechanisms:

- Increased atmospheric density correlates with heightened photon-scattering of Cherenkov light, consequently resulting in a greater proportion of light exiting the FoV of the telescope.
- Augmented atmospheric density corresponds to heightened absorption during the transmission of radiation to the telescope, thereby leading to attenuated observed radiation.

The principal instruments employed by MAGIC to monitor weather conditions include the Pyrometer instrument, the Starguider camera and the LIDAR system:

- **Pyrometer:** Positioned within MAGIC I, Pyrometer is oriented parallel to the observation direction and serves to measure the sky's temperature. By assessing the temperature, it provides insights into the presence of clouds. Clouds, reflecting Earth's thermal radiation, raise the measured temperature. Utilizing atmospheric temperature data, Pyrometer calculates the parameter "cloudiness", offering an assessment of cloud presence at the given time. This parameter is derived by comparing the temperature recorded by the Pyrometer with the typical

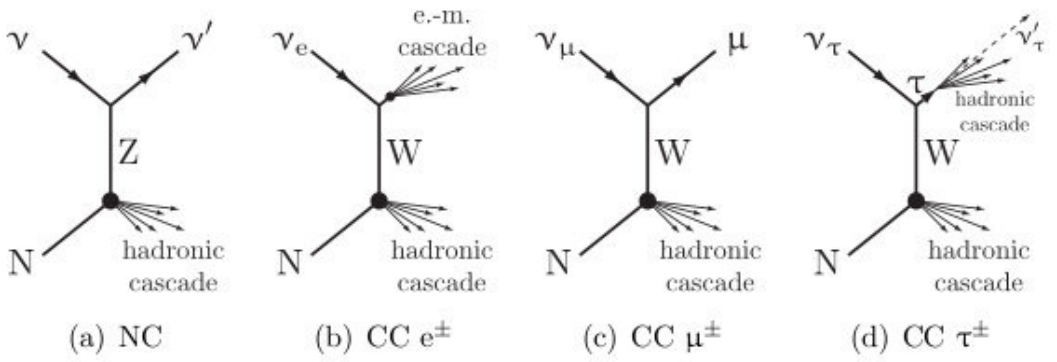

Figure 3.13: Feynman diagrams for neutrino/nucleus interactions. Figure taken from [57].

temperature under clear weather conditions.

- **Starguider:** Functioning as a camera, the Starguider quantifies the quantity of stars within the FoV of MAGIC. It serves as a supplementary tool for cloud detection by comparing the observed star count with a reference value obtained under optimal weather conditions.
- **LIDAR:** The LIght Detection And Ranging (LIDAR) system is used as a valuable instrument for assessing atmospheric transparency, LIDAR operates by emitting laser beams and analyzing the resultant scattered light. It facilitates transparency measurements at various altitudes. However, LIDAR encounters limitations under full moon conditions, during which Pyrometer assumes monitoring responsibilities. LIDAR software can calculate atmospheric transmission, but it is not always possible to correct the energy and spectrum estimates, depending on the transmission value. As a result, data are typically classified into different quality classes based on their calculated transmission at 9 km (T9km), since 10 km is the average height at which showers develop. LIDAR can calculate transmission at 3 km, 6 km, 9 km and 12 km.

3.4 High energy neutrino detector techniques

Neutrinos are very challenging to detect due to their minimal interaction cross-section, necessitating the use of vast detector volumes. To address this, large natural ice and water bodies on Earth serve as effective detection media. Notable neutrino detectors include IceCube, with a 1 km^3 detector volume in Antarctic ice, and ANTARES, a Cherenkov detector in the Mediterranean Sea. Future enhancements include the IceCube-Gen2 [54], which will significantly expand IceCube's volume and capabilities, and the KM3Net project, which will deploy two massive sea water Cherenkov detectors in the Mediterranean, increasing the detection volume compared to ANTARES [55]. Although the neutrino cross section is very small (for neutrino energies between 1 MeV and 10 TeV, the interaction cross section between a neutrino and a proton is approximately $\sigma_{\nu p} \sim 10^{-38}$), the interaction probability depends significantly on the energy of the neutrinos [56]. In particular, as the energy of the neutrinos increases, these interactions become more likely, enabling the indirect detection of neutrinos

through two types of interactions with the detector: charged current (CC) interactions and neutral current (NC) interactions.
When a neutrino reaches the detector, two processes can take place:

- **Charged Current (CC) interactions:** a neutrino (ν_l) exchanges $W^{\pm}$ bosons with a nucleon (N), producing a same-flavor lepton (l) and transforming the nucleon into a new hadronic state (X):

$$\nu_l + N \longrightarrow l^- + X \tag{3.11}$$

  where l = e, ν, τ (see Figure 3.13b, 3.13c, 3.13d). This reaction is a kind of scattering.

- **Neutral Current (NC) interactions:** a neutrino (ν_l) exchanges Z^0 bosons with a nucleon (N), resulting in a same-flavor neutrino (ν_l) and transforming the nucleon into a new hadronic state (X) (see Figure 3.13a):

$$\nu_l + N \longrightarrow \nu_l + X \tag{3.12}$$

In both cases, the X nuclei will induce a hadronic cascade. Additionally, in the case of a CC interaction, the resulting charged lepton (l) will propagate, creating what is known as a track. After some time, this lepton will decay, leading to a secondary cascade: an electromagnetic cascade if l = e, and a hadronic cascade if $l = \mu, \tau$.
Neutrino detection is facilitated through the observation of showers and tracks. Specifically, the detection technique relies on the identification of Cherenkov photons, similar to the method used in IACTs. These photons are produced by charged particles traveling faster than light in the detector medium, which is ice for IceCube and water for ANTARES. Charged particle-induced cascades deposit energy over a short distance, allowing precise energy determination but with poor directional accuracy (3-10°). High-energy leptons (usually muons, $l = \mu$), conversely, travel long distances, offering good directional accuracy (0.5°) but poor energy resolution [58].

3.4.1 IceCube Neutrino Telescope

The IceCube Neutrino Observatory is a large-scale detector located at the South Pole, designed to detect high-energy neutrinos. It consists of a cubic kilometer of clear Antarctic ice, instrumented with 5160 Digital Optical Modules (DOMs) arranged on 86 vertical strings. These DOMs are buried deep in the ice, between 1450 meters and 2450 meters below the surface. A schematic representation of IceCube is shown in Figure 3.14.
IceCube detects neutrinos by capturing the Cherenkov light emitted when neutrinos interact with the ice, producing secondary charged particles that travel faster than the speed of light in the ice. These interactions create a faint blue light, which is detected by the DOMs. The data collected allows scientists to study neutrinos from astrophysical sources, such as supernovae, GRBs, and AGNs, as well as atmospheric neutrinos. As seen before, CC and NC interactions give different products and therefore will leave different signatures in the detector.

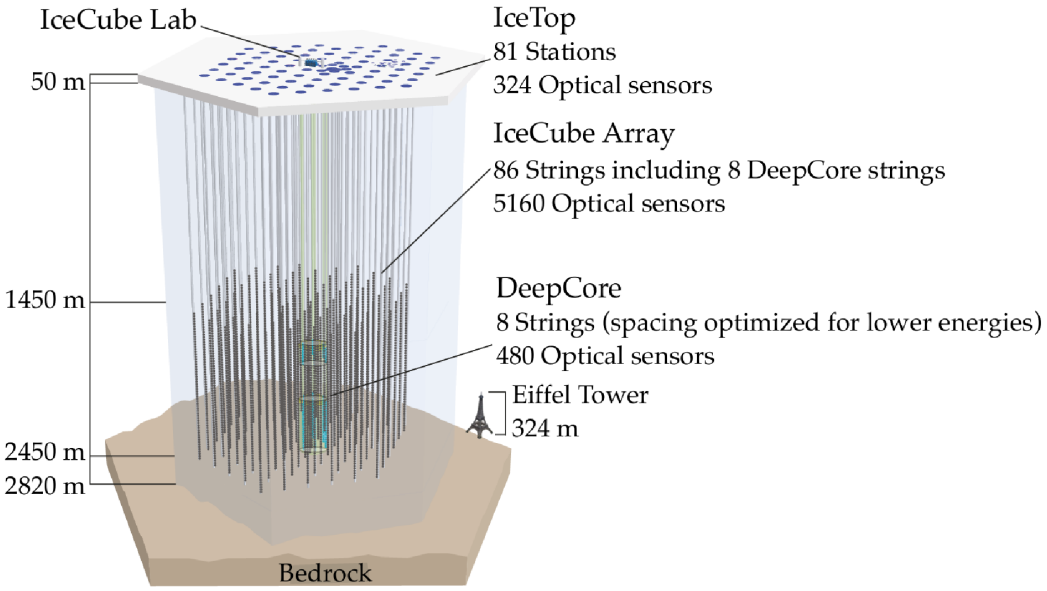

Figure 3.14: schematic representation of IceCube detector. Figure taken from: [59].

The electromagnetic or hadronic showers produced by neutrino interactions extend over several meters. However, compared to the sensor spacing in IceCube, these showers are almost point-like. The Cherenkov light emitted by the decay products of these showers forms a nearly spherical light pattern, which is detected by the array of DOMs embedded in the ice. Muon tracks generate a distinctive elongated pattern of light, contrasting with the spherical shape produced by showers. We can see the different types of signal characterizing these two events in Figure 3.15 (top panels). Also, we can distinguish events caused by hadronic EAS (bottom panels).
The major contamination of astrophysical neutrino observations from an instrument like IceCube comes from two contributions:

- **Down-going atmospheric muons:** Muons are generated in the detector not only through CC interactions by neutrinos but also predominantly from CR showers, which are downward-going (i.e. originated in the southern hemisphere). This makes it challenging to distinguish between muons produced by neutrinos and those from CRs. To mitigate this background contamination, IceCube has an outer veto layer designed to identify and flag muons originating from outside the detector, tagging them as background.

- **Atmospheric neutrinos:** The greatest source of contamination comes from atmospheric neutrinos produced in hadronic EAS. Distinguishing an astrophysical neutrino from an atmospheric one is almost impossible. To address this, only up-going tracks (those originating from the northern hemisphere) are typically considered as true signals.

Distinguishing between muon tracks generated by atmospheric or astrophysical neutrinos within the detector presents a challenge. As a result, only up-going muon tracks are considered as potential signals, as they are more likely to originate from astrophys-

ical neutrino interactions. However, even among down-going atmospheric neutrinos, some are vetoed due to the presence of muons produced in the same CR air shower. This veto strategy helps reduce the atmospheric neutrino background, particularly in the southern sky region.

IceCube alert system

IceCube boasts a remarkable ability to observe the entire sky continuously (the uptime is $\sim 99.8\%$). This continuous operation renders IceCube conducive to real-time studies, prompting alerts to the astrophysical community whenever remarkable events are detected. There are two main types of IceCube alerts that concern the detection of:

- **High-energy neutrino:** these alerts are submitted in a public way via Astrophysical Multi-messenger Observatory Network (AMON) as Gamma-ray Coordinate Network (GCN) notices. This high-energy neutrino has a probability of being of astrophysical origin.
- **Neutrino flares:** these alerts are treated by the Gamma-ray Follow-Up (GFU) alert system. These alerts target known gamma-ray emitters, which are presumed to be potential sources of high-energy neutrinos. GFU alerts related to neutrino flares are kept private and shared exclusively with partner VHE telescopes for follow-up observations. For example the MAGIC collaboration has the Neutrino Triggered Target of Opportunity (NToO) program. Whenever a neutrino event was detected coming from the direction of a predefined list of objects, a trigger was sent and MAGIC attempted to observe the object within a specified time window [61].

The alerts sent by IceCube give information regarding energy, direction, angular uncertainty, and the likelihood of the event being astrophysical [62]. The most important example of such alerts includes the coincident detection of the high-energy neutrino event 170922A and the observation of enhanced gamma emission from the blazar TXS 0506+056 (see Appendix A).

Significance pre/post trial

A specific algorithm, called Time-Clustering algorithm, is used to derive the pre-trial probability of a neutrino flare through the Test Statistic (TS). This algorithm conducts multiple likelihood analyses across various event combinations. However, this iterative process gives a bias in the evaluation of the significance. As we increase the number of analyses on signals from monitored sources, the probability of encountering a result that appears statistically significant purely due to random background fluctuations also rises. This phenomenon occurs because each additional trial introduces another opportunity for background noise to mimic a true signal, thus inflating the chance of false positives. Consequently, extensive analyses can lead to misleading conclusions about the significance of observed events. Thus, the pre-trial probability necessitates correction for these trials. Doing this is not easy; calculating the post-trial significance requires a specific, non-trivial procedure [63].

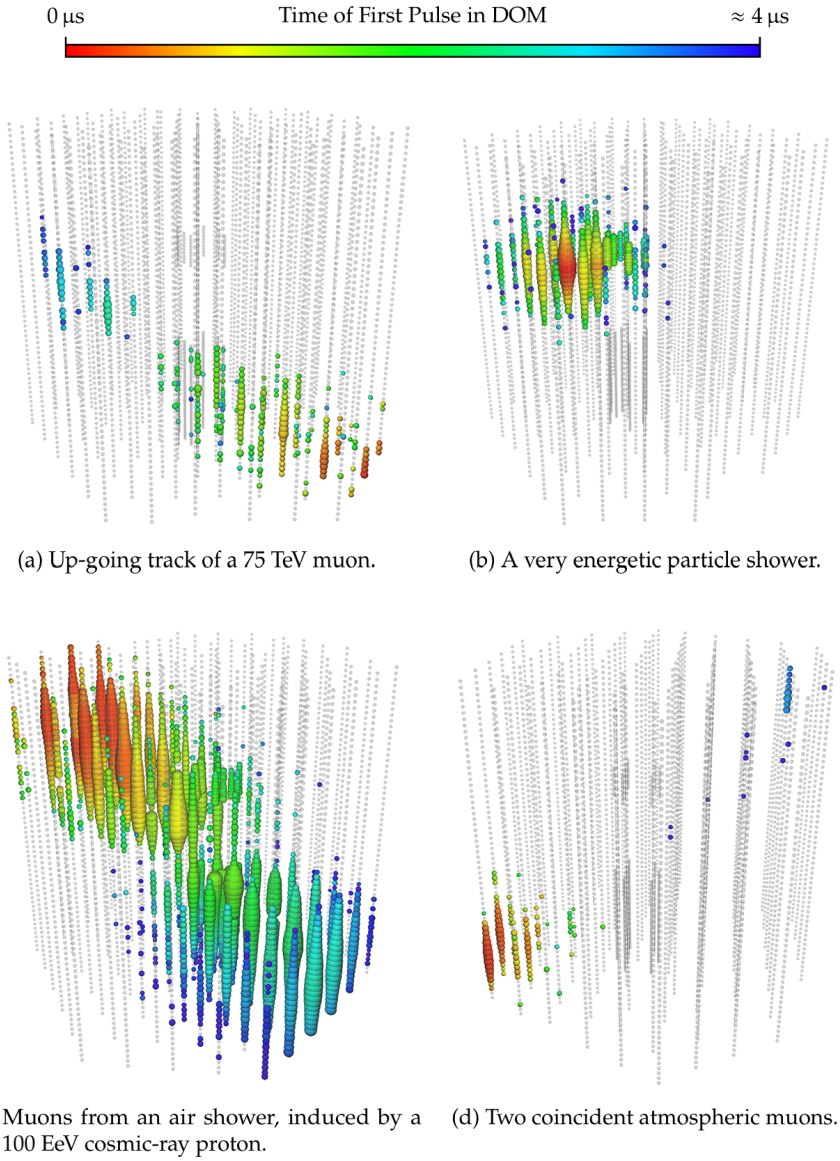

(a) Up-going track of a 75 TeV muon.

(b) A very energetic particle shower.

(c) Muons from an air shower, induced by a 100 EeV cosmic-ray proton.

(d) Two coincident atmospheric muons.

Figure 3.15: IceCube event signatures. Colors correspond to the time of the first photon recorded in a DOM, ranging from red for the earliest to blue for the latest. The size of each bubble reflects the logarithm of the observed charge. Figure taken from: [60].

Chapter 4

MAGIC DATA ANALYSIS

In this chapter, I will present the detailed analysis chain used to reconstruct the relevant primary particle properties (type, direction and energy) of the observational data collected by the MAGIC telescopes. In Section 4.1, I will introduce the possible methods of data taking. In Section 4.2, I will describe the Monte Carlo simulations used to calibrate and optimize the event reconstruction processes. In Section 4.3, I will present the MAGIC Analysis and Reconstruction Software (MARS), the official tool developed by the Collaboration to process and interpret the MAGIC observational data.

4.1 Data-taking procedure

Since MAGIC collects the UV-optical light coming from the Cherenkov flashes, its data will be also affected by the background of natural sky light. Specifically, the efficiency of the telescope is maximized during periods of minimal ambient light, such as in the absence of lunar illumination, such that its efficiency attains a peak duty cycle of 18% [64]. Nevertheless, MAGIC retains the capacity to conduct observations even under moonlight or twilight conditions, achieving a duty cycle of 40% [64]. In addition, telescopes are subject to deterioration as they are exposed to atmospheric agents, requiring continuous maintenance, repair, and calibrations. Consequently, the background noise and the electronic noise must be determined and the acquisition of different types of data on a nightly basis is necessary.
The collected data are:

- **Pedestal subtraction runs:** These runs are taken with the camera system in a closed configuration, serving to calibrate the baseline of the DRS (Domino Ring Sampler) capacitors and set the zero level to 10000 counts.
- **Calibration runs:** These runs serve for data calibration, using a laser emitting light pulses at a constant frequency of 300 Hz. This periodic illumination of the camera system enables the assessment of pixel functionality and calibration integrity by scrutinizing the photomultiplier response to the incident light.
- **Pedestal runs:** These runs are employed to evaluate the impact of the NSB.

Conducted at a frequency of 25 Hz, these runs serve to gauge the influence of ambient sky illumination on observational data.

- **Observational data runs:** These runs collect the data of the targeted sources, typically characterized by an observation duration of 15-20 minutes.

The pedestal subtraction runs are typically taken once nightly or whenever the electronic is warmed up during the night. Pedestal and calibration runs are taken once at the beginning of the night and each time a new source is observed.

4.1.1 ON/OFF pointing mode

Unlike space telescopes characterized by wide FoV, Cherenkov telescopes are limited by a remarkably narrow FoV of 3-4° [47], thus requiring precise pointing toward the celestial sources to be observed. We call the ON region the region that should collect all the signal, while we denote as the OFF region the region used to measure background contamination. Different source pointing modes have been devised: the conventional ON/OFF mode and the contemporary wobble mode. The ON/OFF mode represents the approach to source observation, wherein the center of the camera points directly towards the desired source. To assess background levels, a separate sky observation is conducted independently, within an area devoid of gamma sources but at the same zenith (i.e. same background conditions). Challenges associated with this method include the waste of observation time and dependence on meteorological fluctuations in sky conditions, resulting in variability between ON and OFF observations, when collected even at slightly different times.

4.1.2 Wobble pointing mode

The wobble pointing mode, also known as the False Source Tracking Method, is the standard approach for MAGIC observations. In this methodology, the estimated true position of the source is not centered in the camera. Instead, it is shifted by a specific angle referred to as the "offset angle", typically set at 0.4° for a point-like source. This method mitigates the issues encountered with the ON/OFF mode approach. Specifically, it enables the simultaneous observation of both the source (ON region) and the background (OFF region), thereby eliminating the challenges previously associated with separate observations (refer to the left Figure 4.1). Nevertheless, despite its innovativeness, this method presents some challenges. The accuracy of the background estimate, obtained from a camera position distinct from that of the source, can be affected by the inhomogeneities of the camera responses.
However, significant improvements can be achieved to mitigate these challenges. Mitigating the impact of non-uniform camera responses can be accomplished by incorporating various wobble positions. By exploiting the apparent motion of the sky and, consequently, the motion of the targeted source, together with simultaneous observations of different OFF regions (see the right Figure 4.1), this strategy offers greater accuracy and robustness. The wobble positions, typically, consist of four distinct locations designated as W1, W2, W3, and W4. W1 denotes a slight offset position relative to the source, aligned with the positive direction of the Right Ascension (RA) axis

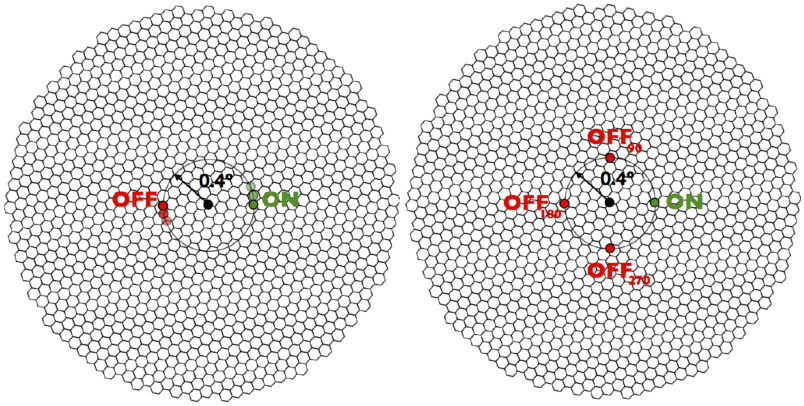

Figure 4.1: Schematic representation of a wobble pointing mode position. The camera center (black dot) and the OFF region (red dot) are located at an angular distance of 0.4° from the source (green dot). Left: Wobble mode of observation in the case of 1 OFF region. Right: Wobble mode of observation in the case of 3 OFF regions. Figure taken from [65].

(0°), while W2 aligns with the negative direction of the same axis (180°). Additionally, positions W3 (90°) and W4 (270°) are situated on the axis perpendicular to the line connecting positions W1 and W2. Furthermore, it is customary to employ at least three OFF regions simultaneously. This practice facilitates a more robust correction for potential background fluctuations. Alternative wobble pointing modes can also be implemented. For instance, if an optical star is positioned at the W1 location, this scenario can introduce alterations to the background. In such case, a "custom" wobble is performed. Instead of pointing in the standard wobble configuration, the telescope is directed to a slightly shifted position (+35°). This adjustment ensures a deviation from the vicinity of the star while still maintaining at constant distance of 0.4° relative to the source. Consequently, W1 angle corresponds to 35°, and similarly, W2 angle corresponds to 215°, W3 angle to 125°, and W4 angle to 305°. This approach effectively safeguards against the star's influence on the background estimate in a straightforward manner.

4.2 Gamma-ray Monte Carlo simulations

Since Cherenkov techniques rely on indirect methods, the utilization of simulations, specifically Monte Carlo (MC) simulations, becomes necessary for data calibration and the subsequent reconstruction of primary particle characteristics. These simulations are typically generated through software known as CORSIKA (COsmic Ray Simulations for KAscade) [66], which is specifically designed for this purpose. CORSIKA facilitates the emulation of particle behavior upon entry into the atmosphere, resulting in EAS. Importantly, this program also enables the simulation of telescope responses to the events under consideration, incorporating various parameters such as the nature, direction, zenith, azimuth, energy of the primary particle, as well as the atmospheric model employed. The atmospheric model utilized by the MAGIC collaboration is denoted as "MagicWinter", which comprises a composition of gases including nitrogen (N_2) at 78.1%, oxygen (O_2) at 21.0%, and argon (Ar) at 0.9%. The

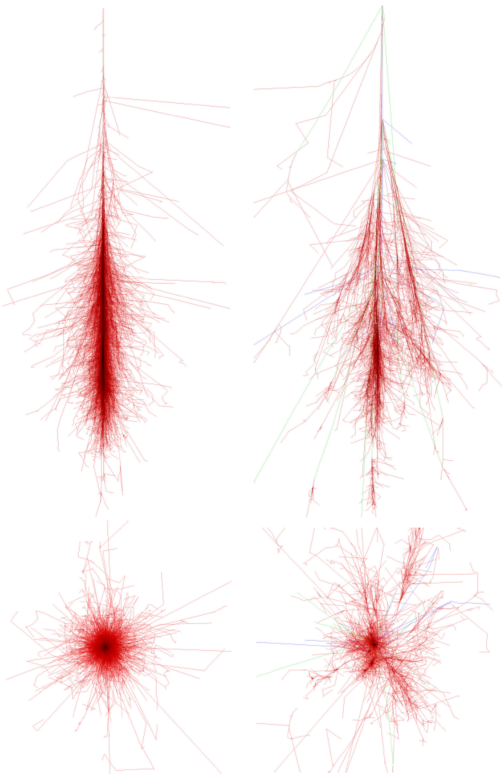

Figure 4.2: MC simulation of a 100 GeV EAS. Top left: Vertical profile of gamma-ray shower. Top right: Vertical profile of proton shower. Bottom left: Transverse profile of gamma-ray shower. Bottom right: Transverse profile of proton shower. Figure taken from [65].

parameters governing the generated images (see left Figure 4.2) facilitate direct comparison with real observational data. For the purpose of analysis within the context of MAGIC, the inclusion of hadronic MC simulations is deemed unnecessary. This is attributed to the practice of employing observations of sky regions lacking significant gamma-ray emissions (OFF observations) as proxies for proton simulations. Consequently, solely gamma-ray MC simulations are employed in this thesis. In the selection of MC simulations, three principal factors must be considered:

- **Pointing mode:** MC simulations should be derived in the same observational mode employed in MAGIC data collection. Specifically, my analysis adopts observations conducted using the wobble pointing mode, featuring a 0.4° off-set ring centered in the camera. Thus, MC simulations must adhere to a similar configuration, known as MC ring-wobble.
- **Range of zenith:** MC simulations should be generated within corresponding zenith ranges as those of MAGIC data acquisition. These zenith ranges are categorized into three main intervals: low (5-35 degrees), medium (35-50 degrees), and high (50-62 degrees).
- **Period of analysis:** MC simulations undergo updates to reflect upgrades or alterations in the telescope hardware system. Consequently, the selection of MC simulations depends on the period when the data where taken. For the OP 313 recent data analysis during 2023-2024, I used MC simulations corresponding to

the period from 2020/03/03, during which data were taken in STereo (ST) mode. This period is called ST.03.20. For the OP 313 historical data analysis in 2021, I used MC simulations corresponding to the period 2020/10/24-2021/09/29, during which data were taken in ST mode. This period is called ST.03.12.

4.3 Standard Magic Analysis and Reconstruction Software

During data taking, the intensity of Cherenkov radiation (measured in photo-electrons) and the respective arrival times for each pixel are recorded. Data are stored in RAW files which, subsequently, are used as inputs to the MAGIC data analysis software, referred to as "Magic Analysis and Reconstruction Software" (MARS). MARS contains several programs in C++ language, implemented in ROOT libraries. It is possible to divide the analysis into three main levels (Figure 4.3):

1. **Low-level analysis:** data conversion from RAW file to ROOT file (program `merpp`) and calibration (program `sorcerer`), image cleaning and parameterization (program `star`).

2. **Intermediate level analysis:** stereo parameter reconstruction (program `superstar`), data quality selection (program `quate`), nature, direction and energy reconstruction of the events (programs `coach` and `melibea`).

3. **High level analysis:** signal significance (program `odie`), sky map reconstruction (program `caspar`), spectral energy distribution and light curve estimation (programs `flute` and `foam`), unfolding spectrum (program `fold`).

4.3.1 Calibration, image cleaning and parameterization

The initial phase of the analysis, commonly referred to as the low-level analysis, constitutes the most time-intensive aspect of the processing procedure, demanding substantial computational resources in terms of CPU time. Typically, this phase is performed to the OnSite Analysis (OSA) system.

Calibration

The initial stage in the analysis chain is the conversion of RAW data into ROOT data format. This process is performed with the `merpp` program (MERging and Preprocessing Program). Subsequent to this, the `sorcerer` program (Simple, Outright Raw Calibration; Easy, Reliable Extraction Routines) is engaged for calibration purposes. This program employs the F-factor method to convert ADC counts into a corresponding count of photo-electrons [67].
Thus, this approach enables the derivation of both the charge (quantified in photo-electrons) and the arrival time of the signal for every pixel within each event.

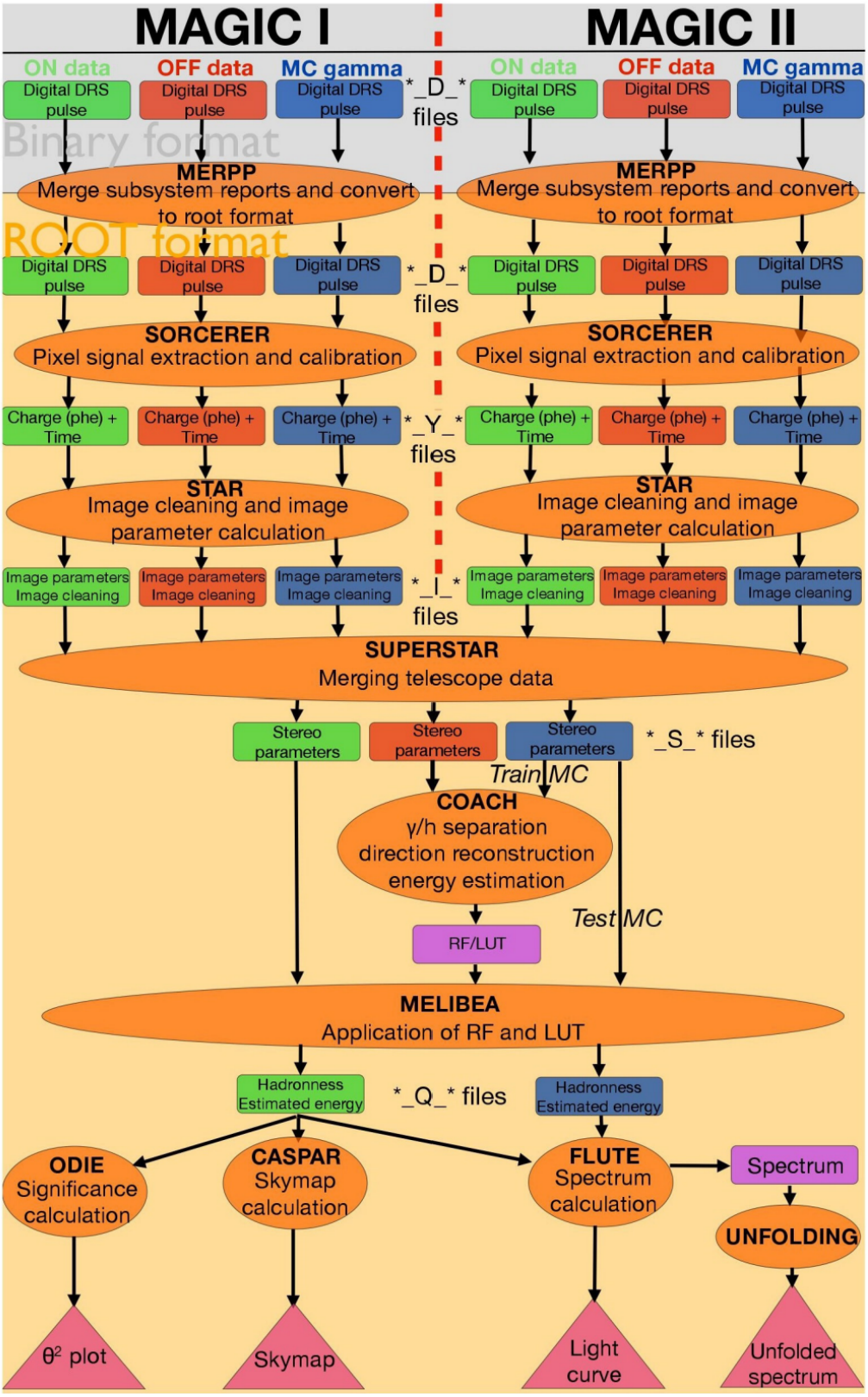

Figure 4.3: Scheme of MAGIC analysis chain. Figure taken from [65].

Image cleaning

The goal is to eliminate pixels devoid of pertinent information regarding the shower, retaining only those most likely due to the gamma-ray signals. The core pixels must comply to the following criteria [47]:

- They must have a charge above a specified threshold, denoted as Q_c (usually set to 6 photoelectrons).
- They must be surrounded by a minimum number of neighboring pixels with recorded signals (usually set between 2 and 4). The standard configuration sets the number equal to 3.
- The arrival times of the core pixels must be closely aligned, within a tolerance of Δ_{tc}= 4.5 ns.

Subsequently, a selection of neighbour pixels is made, governed by the following criteria:

- The charge of these pixels must exceed another predefined threshold, denoted as Q_b (usually set to 3.5 photoelectrons).
- Each contour pixel should encompass at least one core-pixel in its vicinity.
- The arrival times of boundary pixels should be closely aligned, typically within a tolerance of $\Delta_{tb} = 1.5$ ns.

The choice of these thresholds is optimized to ensure background subtraction while retaining comprehensive information regarding the totality of the shower. Naturally, these values are subject to variation depending upon sky conditions, such as the presence of the moon.
An illustrative example of the effect of a cleaning procedure is shown in Figure 4.4.

Parameterization

Upon completion of background removal from the image, the parameterization of the gamma-ray shower becomes feasible. Following this process, the cleaned-up image typically assumes an elliptical configuration within the camera plane. To quantify this ellipse, a fitting procedure is applied, commonly referred to as the "Hillas ellipse", as depicted in Figure 4.5. Thus, it is possible to calculate the so called "Hillas parameters" [69]. The main ones are:

- **Size:** This parameter is the sum of the charge of all pixels. It depends on the primary energy (if the shower exhibits greater energy, it will has a larger size).
- **Center of gravity (CoG):** This parameter represents the center of gravity of the shower image; it is the weighted mean signal of x and y coordinates in the camera plane. The X and Y values are the first moments of the charge distribution in the image.
- **Length:** This parameter is the length of the major semi-axis, it depends on the longitudinal development of the shower. It is important in the determination of

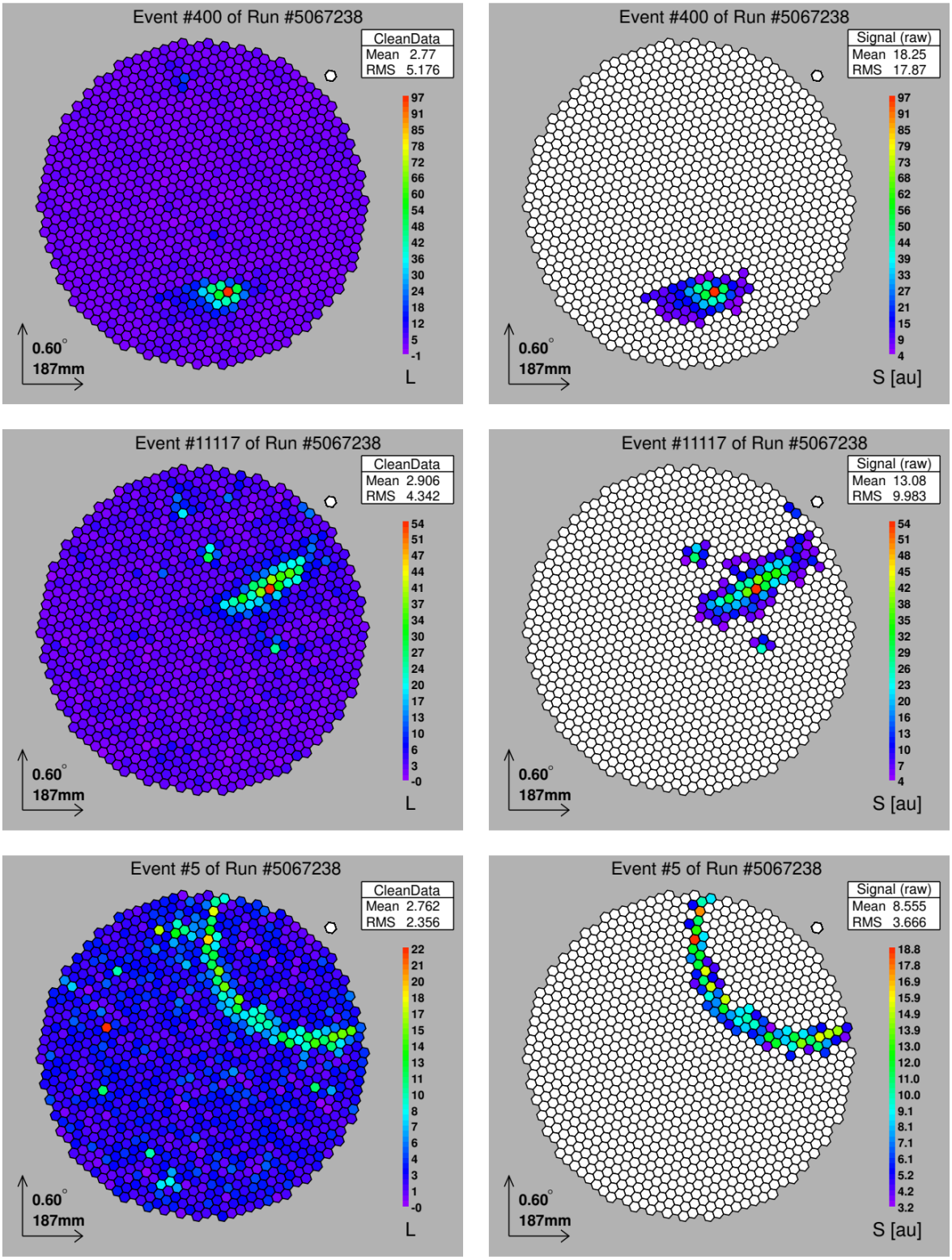

Figure 4.4: Image cleaning of a gamma-like (top), hadron-like (middle) and muon-like (bottom) event. Left: Images of the three events before the cleaning. Right: Images of the three events after the cleaning. Figure taken from [68].

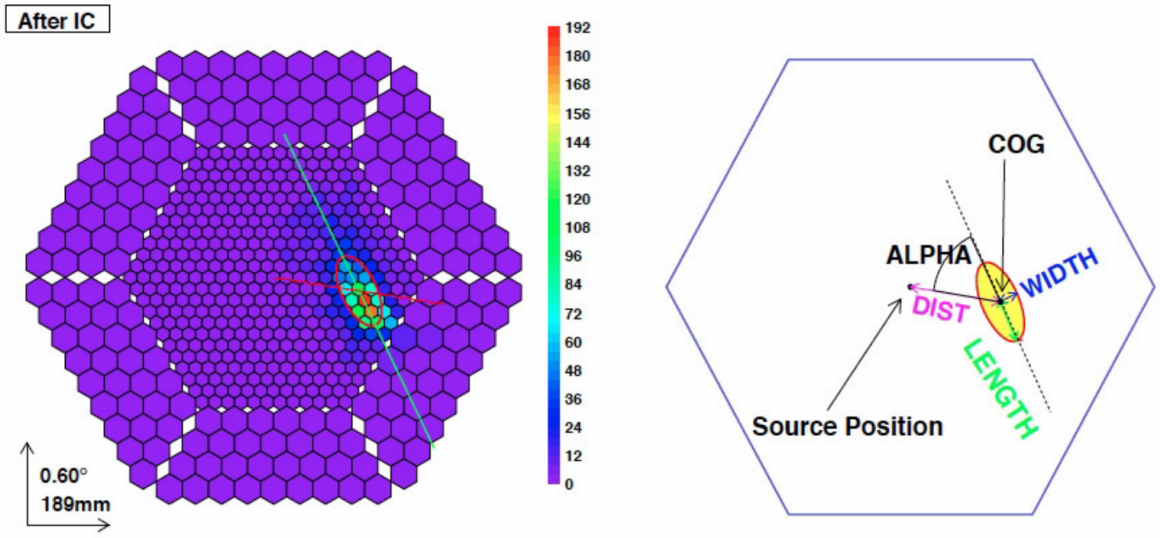

Figure 4.5: The Hillas parameters. Left: The Hillas ellipse fitted to the shower pixels that survived the cleaning. Right: Some of the main Hillas parameters.

the nature of the primary particle, in fact this parameter is generally larger for hadron-induced showers than for gamma-induced showers.

- **Width:** This parameter is the length of the minor semi-axis. It depends on the transverse development of the shower. It is important in the determination of the nature of the primary particle, in fact (as seen in Figure 4.2 and as presented in Section 3.2), heightened transverse development of the shower suggests a predominantly hadronic nature of the primary particle.

- **Conc(N):** This parameter quantifies the charge contained in the N brightest pixels, and this provides information regarding the maximum of the shower and its compactness. It is important for the estimate of the nature of the primary particle. Typically, the value N is set to 2, based on MC simulations.

Moreover, the source-dependent parameters related to the physical properties of the shower are determined:

- **Dist:** This parameter represents the angular separation between the assumed source position (reference point in the camera) and CoG of the shower. It gives information about the distance of the shower maximum from the telescope axis.

- **Alpha:** This parameter is the angle between the major axis of the Hillas ellipse and the line connecting the expected source position to the CoG of the camera image. This parameter is important for the estimate of the primary particle's nature (gamma-rays tend to exhibit small alpha angles, whereas hadrons typically demonstrate an isotropic distribution across the sky, resulting in a more uniform distribution of alpha angles).

- **Time gradient:** This parameter represents the linear slope of pixel arrival times along the major axis of the ellipse. It gives the significance of the temporal correlation between the recorded signals and it provides insight into the direction

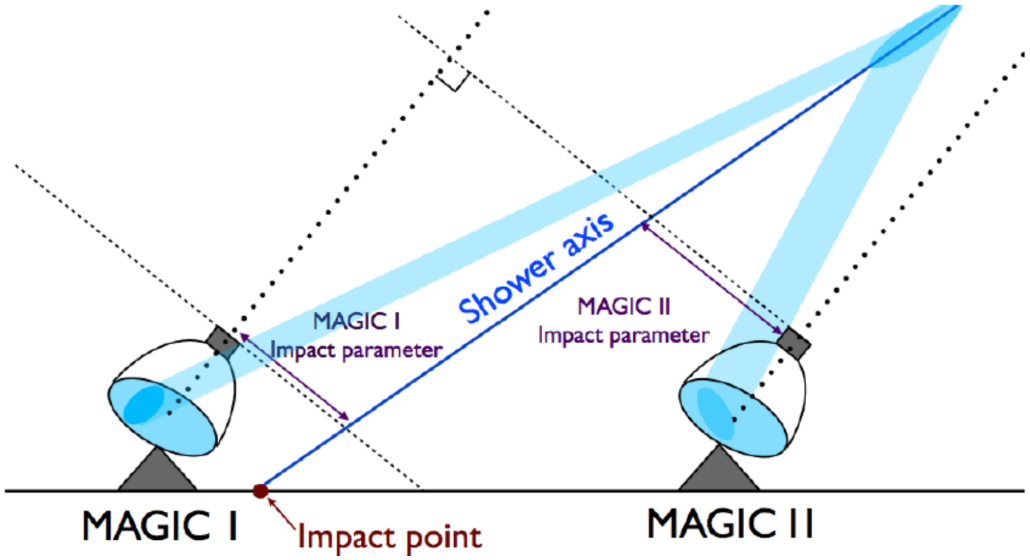

Figure 4.6: Schematic illustration of the main stereoscopic parameters. Figure taken from [65].

of shower propagation.

- **Asymmetry:** This parameter provides the sign of the direction between the CoG and the brightest pixel; it is important in determining the positioning of the head and tail of the EAS.

All these parameters fitting is done by the program `star`.

4.3.2 Stereo reconstruction and data quality selection

Under standard conditions, devoid of factors such as lunar interference or hardware malfunctions, the analysis starts processing stereo data, in the so-called intermediate stage of data processing.

Stereo parameter reconstruction

Up to this point, we have relied on data collected from MAGIC I and MAGIC II telescopes individually. Subsequently, we integrate the information from both telescopes to derive stereoscopic parameters, enabling the reconstruction of the shower in three dimensions. This process is done by the program `superstar`. A schematic representation of the main stereoscopic parameters is presented in the Figure 4.6. These parameters include:

- **Shower axis:** This parameter provides us the direction of the shower. It is computed through the intersection of the two major axes of the Hillas ellipses derived from MAGIC I and II images, also using information about the position and pointing of the telescope [70], [71].
- **Impact parameter:** This parameter represents the distance between the axis of the shower and the pointing direction.

- **Height of shower maximum:** This parameter denotes the altitude at which the EAS attains its maximum particle count. Its value depends on the energy of the primary particle (higher energy particles penetrate deeper into the atmosphere, resulting in a maximum occurring closer to the telescope, and vice-versa).

Data quality selection

Data integrity is frequently affected by weather conditions or technical anomalies, necessitating the establishment of criteria for rectification or exclusion of certain data. To fulfill this requirement, the program `quate` is employed. This program uses a set of parameters across multiple runs of star or superstar data, subsequently executing data selection and classification procedures. For instance, selections can be made based on zenith and azimuth angles, atmospheric transmission, or Direct Current (DR) (the latter is particularly advantageous for discerning moon-night conditions).

4.3.3 Type, direction and energy reconstructions of the event

To extract useful information regarding the primary particle, it is necessary to:

- differentiate between showers initiated by primary gamma particles and those induced by hadronic interactions;
- reconstruct the direction of the primary gamma particle;
- estimate the energy of the primary gamma particle.

In order to do this, Random Forest (RF) is employed. Initially, a RF is constructed through the use of the program `coach` (train phase). Subsequently, it is applied to the observed data and MC using the program `melibea` (test phase). The RF algorithm comprises a collection of decisional "trees", typically 100 by default.

Nature estimation

In order to perform the discrimination between gamma-rays and hadrons, gamma-ray MC simulations serve as essential input for the RF. These simulations reproduce the behaviour of gamma-rays across varying energy ranges, directions, zenith angles and analysis periods. Additionally, the RF necessitates a representation of the background attributed to hadrons. This role is fulfilled by the so-called OFF data, derived in a simple way from MAGIC observations conducted within a region devoid of gamma-rays. While theoretically possible, an alternative approach could involve employing MC simulations of protons instead of utilizing OFF data. However, such simulations are significantly more complex to handle. Primarily, to construct the RF, a parameter (X) is randomly chosen. Subsequently, the RF seeks the "cut value" (A) for this parameter, defined as the value that optimally separates hadronic events from gamma events. Consequently, all events that satisfy the condition $X < X_A$ are directed to one branch, while those satisfying $X > X_A$ are directed to another. As a result, one branch predominantly comprises gamma-like events, while the other predominantly comprises hadron-like events. The cut value is chosen by minimizing the Q-Gini [72],

which is a parameter defined as follows:

$$Q_{Gini} = 4\frac{N_\gamma}{N}\frac{N_h}{N} \tag{4.1}$$

Whenever the Q-Gini value is minimized, the separation between gamma and hadrons is maximized. At this point, the procedure iterates: another parameter is selected, as the parameter value that optimally distinguishes between hadrons and gamma particles. Consequently, sub-branches are formed from these initial sub-samples of the two particle types. This iterative process persists until a complete division between gamma and hadrons is achieved, thereby resulting in the creation of a tree. Subsequently, these steps are reiterated, generating a designated number of trees. Upon completion of each tree, an event is classified as either a hadron or a gamma particle. This task is executed by the `coach` program. While `melibea` processes each individual `superstar` event sequentially through each of the 100 trees. At the conclusion of each tree, a value of 1 is assigned if the tree identifies the event as a hadron, or a value of 0 if the event is classified as a gamma particle. Subsequently, the values obtained from all 100 trees are averaged, yielding what is termed the "hadronness parameter". This parameter, ranging from 0 to 1, serves as an indication of the event's probability of being a hadron.

Direction reconstruction

If the goal is to reconstruct the direction of the primary particle, the RF method can be employed. However, the construction of the RF in this instance differs slightly from the previous approach. Whereas the previous RF was utilized for discrete classification, the present RF must allow for continuous classification. To achieve this, a parameter known as the "DISP-parameter" is used, which is associated with the center of gravity of the image. This parameter is determined by the following formula:

$$\text{DISP} = \text{A(size)} + \text{B(size)}\frac{\text{width}}{\text{lenght} + \eta(\text{size}) \cdot \text{leakage2}} \tag{4.2}$$

where A(size), B(size) and η(size) are second order polynomials of the logarithm of the image size. The additional term appended to the length parameter compensates for the truncation of sizable images occurring at the camera's periphery, expressed in relation to the leakage parameter. These terms are optimized considering gamma-ray MC simulations, using a regression method. Each MAGIC telescope calculates a DISP parameter using its respective image parameters. Through a dedicated procedure outlined in references [73] and [74], the reconstructed position of the source is derived.

Energy reconstruction

The estimation of energy can be achieved through either the RF method or the Look Up Tables (LUTs) method. The conventional approach involves the utilization of LUTs [75], which are tables derived from MC data, where the true energy is known. These tables provide estimates of how the energy of the primary particle correlates with stereoscopic parameters. The underlying assumption is that the energy of the

Energy Range	Hadroness	Size	θ^2
LE	< 0.28	> 60	< 0.02
FR	< 0.16	> 300	< 0.009
HE	< 0.1	> 400	< 0.007

Table 4.1: Standard predefined cuts in different energy ranges.

primary particle depends on the number of Cherenkov photons within the EAS, and thus, it is influenced by the size of the shower. By comparing the parameters of real data with the information stored in the tables, the primary energy can be inferred. On the other hand, the RF method offers enhanced accuracy. It employs a set of parameters to estimate the energies of events.

4.3.4 Signal significance and sky map reconstruction

We can now progress to the high-level data processing stage aimed at generating graphical outputs for scientific analysis, including signal significance, sky maps, spectra, and light curves.

Signal significance

It is important to generate signal histograms, also known as θ^2-plots, as they provide indications of the potential presence or absence of gamma-ray emission from the analyzed source. The θ^2 distance refers to the squared angular distance between the position reconstructed and the true position of the source (at which the telescope pointed). These θ^2 histograms illustrate the number of gamma-ray events recorded on the y-axis against the θ^2 values on the x-axis. Typically, two types of histograms are plotted: the ON-histogram and the OFF-histogram. In order to construct these histograms, we consider both the ON region and the average of the OFF regions. Events from each respective region are counted and distributed based on their θ values. In the OFF region, we will expect a uniform distribution of events with respect to θ. Essentially, three types of backgrounds contribute to the OFF-distribution: misreconstructed hadrons, diffuse gamma-rays, and electrons/positrons initiated showers. In the ON region, we will expect a distribution of events that peaks for small values of θ^2 denoting the presence of a source. An example of the θ^2-plot is shown in Figure 4.7 According to the energy range, cuts are imposed on the previously estimated parameters (hadroness, size, and θ^2) to optimize the discrimination of gamma-ray events from background hadronic events [47]. These cuts are optimized to maximize sensitivity for Crab Nebula observations, which serve as the standard candle in the VHE domain. Table 4.1 presents three predefined sets of standard cuts categorized as Low Energy (LE), High Energy (HE), and Full Range (FR). The number of excess events N_{ex} is given by:

$$N_{ex} = N_{on} - \alpha N_{off} \tag{4.3}$$

where α is the inverse of the number of OFF region used to build the OFF histogram. The significance of the gamma-ray excess is established by the significance of $Li\&Ma$

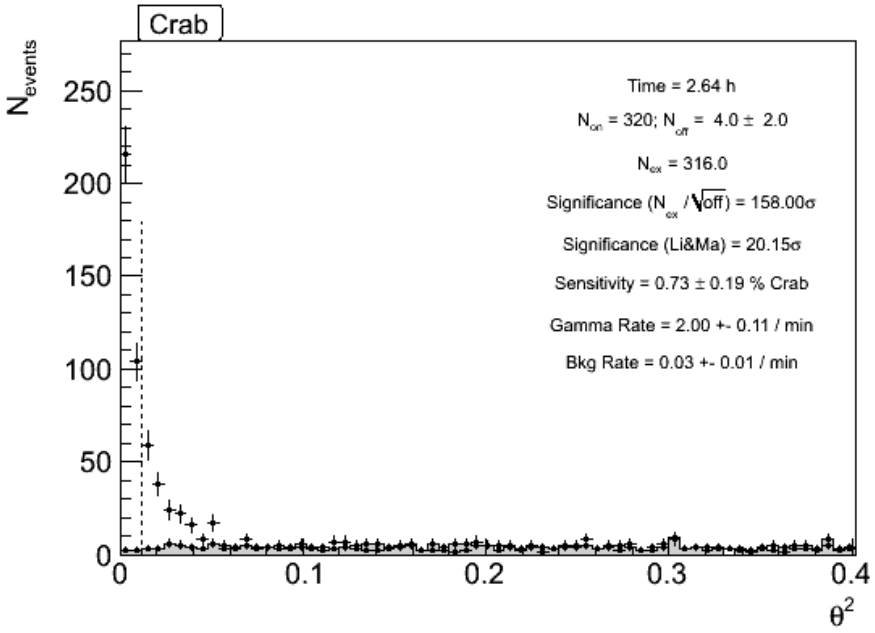

Figure 4.7: Example of a θ^2-plot of Crab Nebula data. In this case, LE cuts are used.

[76], given by:

$$\sigma_{Li\&Ma} = \sqrt{\left(2N_{on}\ln\left[\frac{1+\alpha}{\alpha}\left(\frac{N_{on}}{N_{on}-N_{off}}\right)\right] + N_{off}\ln\left[(1+\alpha)\left(\frac{N_{off}}{N_{on}-N_{off}}\right)\right]\right)} \tag{4.4}$$

When $\sigma_{Li\&Ma} > 3\sigma$, we refer to observational hint; when $\sigma_{Li\&Ma} > 5\sigma$, we refer to a real gamma-ray observation. These type of plots are generated using the program `odie`.

Sky map reconstruction

The program `caspar` constructs a two-dimensional histogram, also known as a sky map, representing the candidate source in equatorial coordinates, with the aim of depicting the arrival direction of gamma-rays. The estimation of background levels in sky maps presents considerable challenges due to dependencies on factors such as zenith and azimuth angles, magnetic field strength, and irregularities in pixel response, particularly when dealing with extended sources. Consequently, they are not recognized in the representation of signal data. To assess the significance of the sky signal, a statistical measure known as Test Statistics (TS) is employed. An example of sky map is shown in Figure 4.8. Each point within the sky map, defined by specific Right Ascension (RA) and Declination (Dec) coordinates, yields a corresponding TS value. It is expected that high TS values will only be observed in regions where the signal is present.

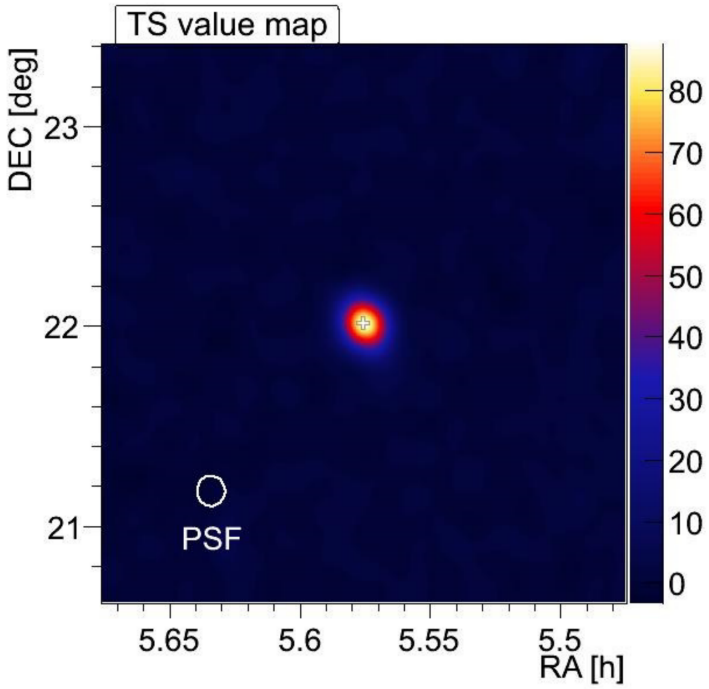

Figure 4.8: Example of sky map of Crab Nebula data. In this case, LE cuts are used.

4.3.5 Spectral energy distribution and light curve reconstruction

Through the `flute` program, the SED and Light Curve (LC) can be derived. First of all, it is essential to introduce certain physical quantities. The differential gamma-ray flux [cm^{-2} s^{-1} TeV^{-1}] is defined as the total number of photons detected, divided by the energy, area, and time unit:

$$\frac{d\phi}{dE} = \frac{dN_\gamma(E)}{dt_{eff} dA_{eff} dE} \tag{4.5}$$

where N_γ represents the excess number of gamma-rays over the background for a given energy bin. The effective time t_{eff} is defined as the total observation time minus the dead time of the data acquisition system. The effective area A_{eff} is the collection area of MAGIC system.
The integral flux [cm^{-2} s^{-1}] is the energy integral of the Equation 4.5:

$$\Phi_{E>E_{th}} = \int_{E_{th}}^{\infty} \frac{d\phi}{dE}\, dE \tag{4.6}$$

The SED [TeV cm^{-2} s^{-1}] is written as:

$$E^2 \frac{d\Phi}{dE} = E \frac{d\Phi}{d(\ln E)} \tag{4.7}$$

It is evident that to compute these quantities, we must determine the following three factors: N_γ, A_{eff}, t_{eff}. To determine the **number of gamma-rays**, a histogram is constructed with excess events, employing specific cuts tailored to each energy bin. The procedure is similar to that carried out in `odie`.
Through the application of Poissonian statistics, it is possible to derive the **effective observation time**, defined by the following formula:

$$t_{eff} = \frac{t_{elaps}}{1 + \lambda d} \tag{4.8}$$

where t_{elaps} is the total elapsed time used for observation, d is the "dead time" (namely the time during which the detector could not record events), λ is the rate of recorded events. Assuming that the dead time d after each event is constant, the total fraction of dead time is λd. The computation of the effective time is executed within `flute`, which uses the simple method called "fixed dead time" in which the user manually sets the amount of dead time per event (after the DAQ system upgrade in 2011 it is set at 26×10^{-6} seconds).
The **effective area** is the hypothetical size of a perfect detector that would detect gamma-rays at the same rate as the MAGIC detector. In computational terms, it is just the surface integral of the detector efficiency ϵ(x,y) in a plane orthogonal to the direction of the incident gamma-rays. For gamma-rays of a specific energy, the efficiency tends to remain relatively constant when telescopes are positioned within the Cherenkov light pool (it is roughly a circle with a radius of 120 meters for gamma-rays incident vertically at the altitude of the MAGIC site), maintains a relatively uniform density of Cherenkov light. However, beyond this region, the efficiency decreases rapidly as the distance of the telescopes to the light pool increases. The effective area depends on various factors, including the gamma-ray energy, its angle of incidence, and the alignment of the telescopes relative to it. Some of these dependencies can be easily predicted based on qualitative analysis, while others necessitate meticulous MC simulations for accurate estimation. For example, the effective area depends linearly on the energy of the primary gamma-ray: a higher energy of the primary particle corresponds to a larger effective area, as more Cherenkov light reaches the detector, and hence the higher the detector efficiency will be. In addition, as the zenith angle increases, indicating a greater distance from the telescopes to the shower, the atmospheric depth also increases. This makes the light pool larger but also dimmer. This leads to an increase of the threshold energy of the telescopes and a larger effective area. The effective area must be computed using the MC method, simulating a detector that captures gamma events at a rate similar to that of the MAGIC telescope. Typically, the simulation is performed so that the gamma-ray impact points are distributed over a large area A_{MC} orthogonal to the direction of the gamma rays, with the simulated IACT system in the center. The area must be large enough so that the probability of a gamma-ray beyond it being able to trigger the system and survive the entire analysis process is negligible. This obviously depends on the energy and direction, so A_{MC} is not fixed in the simulation. Since the distribution of events on A_{MC} is homogeneous, the effective area is the product of A_{MC} times the average efficiency, namely, the total number of MC gamma-rays after all analysis cuts divided by the total number of MC

gamma-rays generated:

$$A_{eff} = \frac{N_{\gamma,fin}(E; E + dE)}{N_{\gamma,sim}(E; E + dE) A_{MC}} \tag{4.9}$$

where $N_{\gamma,fin}$ is the final number of gamma-rays after all the analysis cuts have been applied, $N_{\gamma,sim}$ is the total number of simulated gamma-rays (including those not triggering the telescopes), in the given energy range [E; E + dE]. The program `flute` calculates the effective area for gamma rays in the MC (melibea) files provided as input.
Once the parameters N_γ, A_{eff}, t_{eff} have been calculated, `flute` derives the quantities in the Equations 4.5, 4.6, 4.7, generating SED and LC. During data analysis, since energy bins must be larger if a significant excess is to be obtained, an average A_{eff} needs to be calculated:

$$\langle A_{eff} \rangle_{[E_1;E_2]} = \int_{E_1}^{E_2} \frac{d\phi}{dE} A_{eff}(E) dE \tag{4.10}$$

It's evident that the spectrum of the source isn't always predetermined. Hence, to compute the effective area, an assumed spectrum is required.
The accuracy of the result varies depending on the disparity between the actual and assumed spectra. Furthermore, the binning of real data bins depends on zenith and azimuth angles. In `flute`, computations are consistently executed in distinct bins delineated by both energy and zenith angle. However, the inclusion of azimuth angle variability is discretionary, beacuse of the weaker dependence.

4.3.6 Energy spectrum unfolding

The exact energy of our events remains unknown, since the true energy of an event slightly deviates from the estimated energy due to statistical uncertainties in measurements (typically around 15% in MAGIC [47]). Instead, the effective area is characterized within bins of true energy derived from MC data. When using these two quantities, one categorized by estimated energy and the other by true energy, it results in what is known as event spillover or migration. Events falling within a certain energy range, $E_1 < E_{true} < E_2$, might not entirely reside within the corresponding range of estimated energy, $E_1 < E_{est} < E_2$; some may fall outside of it. Failure to consider this effect leads to inaccuracies in flux estimation, consequently affecting the spectrum and light curve determinations.
As a consequence, it becomes imperative to implement an unfolding procedure on the results obtained from `flute` so that we can correct for this effect. To achieve this, one can process `flute`'s output using, for example, the program `fold`. This can be done by constructing migration matrices (Figure 4.9), derived from gamma-ray MC simulations, particularly through the LUTs, which establish a correlation between gamma-ray energy and image parameters. The inputs needed by `fold` are ON and OFF source histograms (events vs E_{est}), effective time, MAGIC response function (A_{eff} vs E_{true} for each of the E_{est} bins), source spectrum and redshift. Given those, it is possible to calculate the expected number of gamma-rays (N_γ vs E_{est}). Then, one

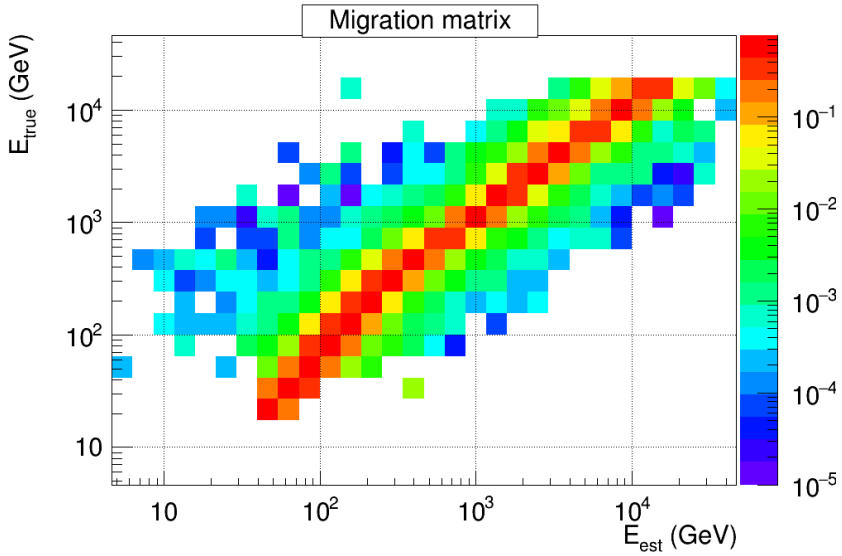

Figure 4.9: Example of migration matrix from estimated energy (x-axis) to true energy (y-axis).

can calculate the poissonian likelihood of the spectrum, given the ON/OFF observations. Ultimately, it gives an estimate of spectral parameters and their uncertainties, alongside SED as the output display.

Chapter 5

DATA ANALYSIS OF THE BLAZAR OP 313

Located billions of light-years away from Earth, in December 2023, the blazar OP 313 became the most distant AGN detected in the VHE energy range and it is the tenth FSRQ ever detected in the VHE regime.
Understanding OP 313's behavior not only sheds light on the intricate mechanisms governing blazar activity but also contributes to our broader understanding of cosmic particle acceleration, relativistic jets, and the evolution of galaxies hosting AGNs.
In this Chapter, I will describe the state of the art of the gamma emission coming from the blazar OP 313 during the last ten years, from 2014 until 2024, as well as its possible link with neutrino alerts from IceCube. Specifically, in Section 5.1 I will give some information about the blazar OP 313. In Section 5.2 I will describe all the historical results of OP 313 observed by MAGIC and Fermi-LAT. In Section 5.3 I will describe the detailed data analysis I performed on the MAGIC data of OP 313, from December 2023 to April 2024 and I will present the results obtained by Fermi-LAT during the same time period. Finally, in Section 5.4 I will describe the neutrino alerts from IceCube, received in 2012, 2020 and 2024.

5.1 Properties of the blazar OP 313

As we have seen in Chapter 2, blazars are a unique class of AGNs characterized by intense emissions across the entire electromagnetic spectrum. Particularly, OP 313 belong to the class of FSRQs. Typically, FSRQs are located at greater distances than BL Lacs [77], and thus are more affected by interaction with EBL photons, which causes flux attenuation at higher energies (including the VHE range), dependent on the redshift of the source. This results in greater difficulty in detecting more distant sources [78]. FSRQs are sources with high variability in the VHE band [79]. Therefore, follow-up observations in the VHE domain usually take place following alerts coming from lower energy ranges or following multi-messenger alerts, for example from the IceCube Neutrino Observatory.
Like all FSRQs, OP 313 exhibits a SED that shows two peaks, the first in the infrared

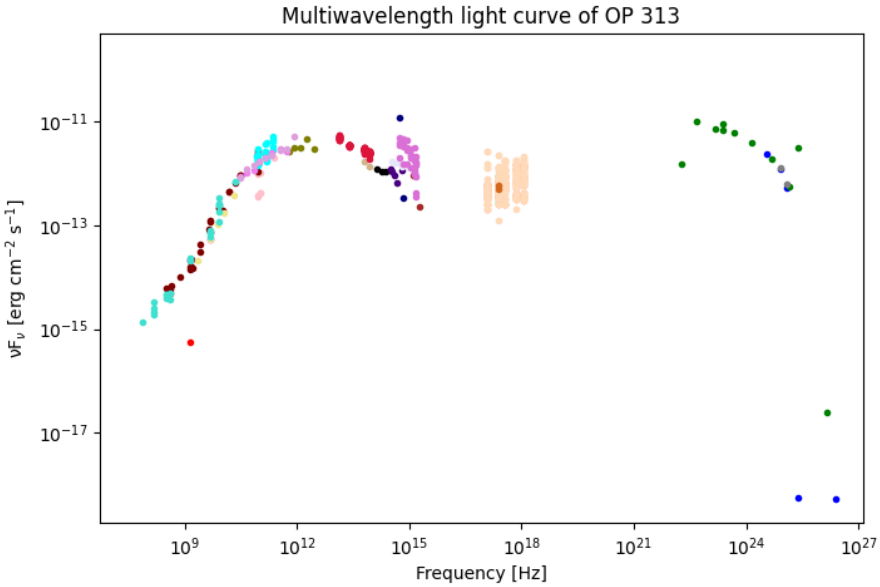

Figure 5.1: Multiwavelength SED of OP 313. To construct it, I used the archival data downloaded from the online tool *Firmamento* (`https://firmamento.hosting.nyu.edu`).

range ($\sim 10^{13}$ Hz), and the second in the gamma range ($\sim 10^{23}$ Hz), specifically $\sim$ GeV. It is possible to visualize this in Figure 5.1, in which I calculated a multiwavelength SED using numerous archival data in different catalogs, downloaded from the online tool *Firmamento*.
OP313 is located at RA = 197.65° and Dec = 32.35° [80] and at present, no definitive estimation regarding the mass of its central SMBH is available within the astronomical literature. OP 313 exhibits redshift z = 0.9980 ± 0.0005, as reported by Hewett and Wild in 2010 [81]. OP 313 stands out as a fascinating object of study, it is renowned for its dynamic behavior, particularly its intense gamma-ray flares. These flares, most probably, triggered by interactions between high-energy particles and magnetic fields in the vicinity of the SMBH at the blazar's center, offer valuable insights into the extreme astrophysical processes occurring within blazars.

5.2 Historical data analysis of the blazar OP 313

The characterization of the activity states of an AGN is essential to better understand the ongoing physical processes. OP 313 was monitored for several years covering the entire electromagnetic spectrum. Here I report the most important follow-up campaigns. In 2014, a flare was detected in gamma-ray range from a source positionally consistent with OP 313 [82], which resulted in its inclusion in the Fermi-LAT monitored sources catalog. Then, after a period of quiescence, since 2018 an enhanced state of activity was detected in gamma-ray wavelengths [83], optical [84, 85, 86] and NIR wavelengths [87]. In 2022, major flares were recorded from Fermi-LAT [88], Ferson telescope in Colgate University Foggy Bottom Observatory [89] and ATLAS telescope [90].

Date	T_{obs} [h]	MC	Zd range [°]
2014-04-28	4.67	ST.03.03	4–39
2014-05-01	0.63	ST.03.03	20-28
2014-05-03	0.55	ST.03.03	5-9
2014-05-04	0.63	ST.03.03	10-18
2014-05-05	0.63	ST.03.03	18-27
2014-06-02	0.61	ST.03.03	18-26
2014-06-03	0.58	ST.03.03	27-35
2019-06-21	0.60	ST.03.11	15-26
2019-06-23	0.68	ST.03.11	16-28
2019-12-25	0.66	ST.03.12	30-38
2019-12-27	0.63	ST.03.12	17-27
2019-12-28	0.93	ST.03.12	17-30
2019-12-29	0.70	ST.03.12	27-37
2019-12-30	0.60	ST.03.12	25-33
2019-12-31	0.60	ST.03.12	23-31
2020-06-19	1.23	ST.03.14	16-34
2020-06-20	0.55	ST.03.14	18-25
2020-06-23	1.02	ST.03.14	19-34
2021-02-20	**1.93**	**ST.03.12**	**3-28**
2021-04-18	**0.72**	**ST.03.12**	**22-32**
2022-06-23	0.78	ST.03.18	37-48
2022-06-27	0.93	ST.03.18	23-35
2022-06-28	0.95	ST.03.18	23-36
2022-06-30	0.25	ST.03.18	29-32
2022-07-01	0.97	ST.03.18	25-37

Table 5.1: MAGIC data of OP 313 collected from 2014 to 2022. For each observation date, I specified the total observation time, the MC simulations used in the analysis, and the zenith range at which the observations were taken. I analyzed the data highlighted in bold.

5.2.1 Results from MAGIC

No observations with MAGIC in the past years yielded relevant results. OP 313 seems to show a quiescent state in VHE range until 2023. In Table 5.1 I report all the OP 313 data analyzed from 2014 to 2022, and in Table 5.2, I report the total observation time and the significance of the emission calculated for each year, using standard cuts in LE range. Specifically, I analyzed data from 2021 (those highlighted in bold) and I found the θ^2-plot and the sky map shown in Figures 5.2 and 5.3. The analysis was cross-checked with Crab Nebula (see Appendix B.1).

5.2.2 Results from Fermi-LAT

In contrast to the observations of OP 313 with MAGIC, this source had shown important flares in the past with Fermi-LAT. The first was detected on 2014 April 14, with

Year	Observational time [h]	$\sigma_{Li\&Ma}$
2014	9.98	0.38
2019	5.03	0.28
2020	3.11	0.80
2021	2.65	-0.70
2022	3.98	0.60

Table 5.2: Observational times and significances of MAGIC data of OP 313 analyzed for each year from 2014 to 2022 [91].

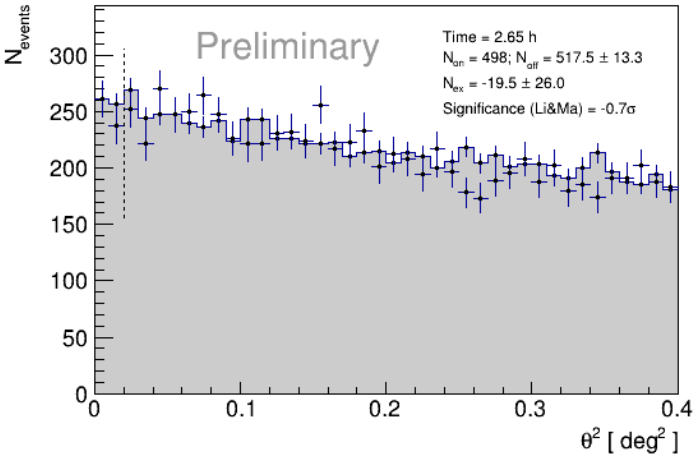

Figure 5.2: θ^2-plot of OP 313 for data taken in 2021.

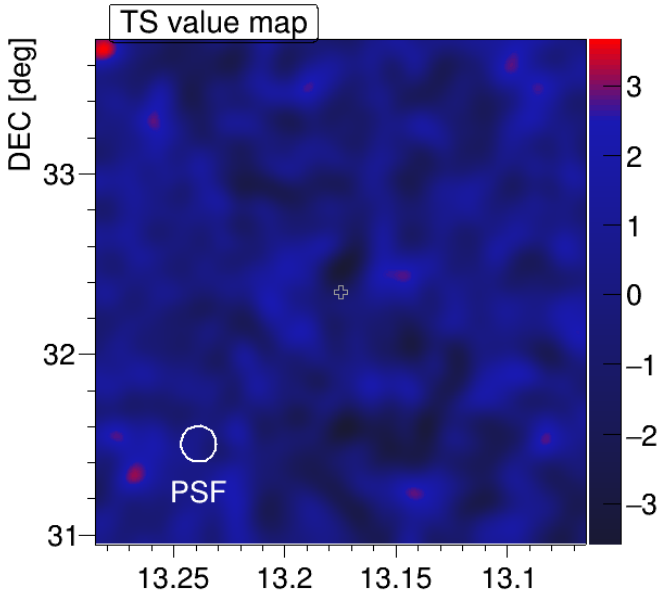

Figure 5.3: Sky map of OP 313 for data taken in 2021.

a daily averaged gamma-ray flux (E > 100MeV) of $4.8 \pm 1.2 \times 10^{-7}$ photons cm^{-2} s^{-1}. Another strong flare occurred in 2022, on June 27, with a daily averaged gamma-ray

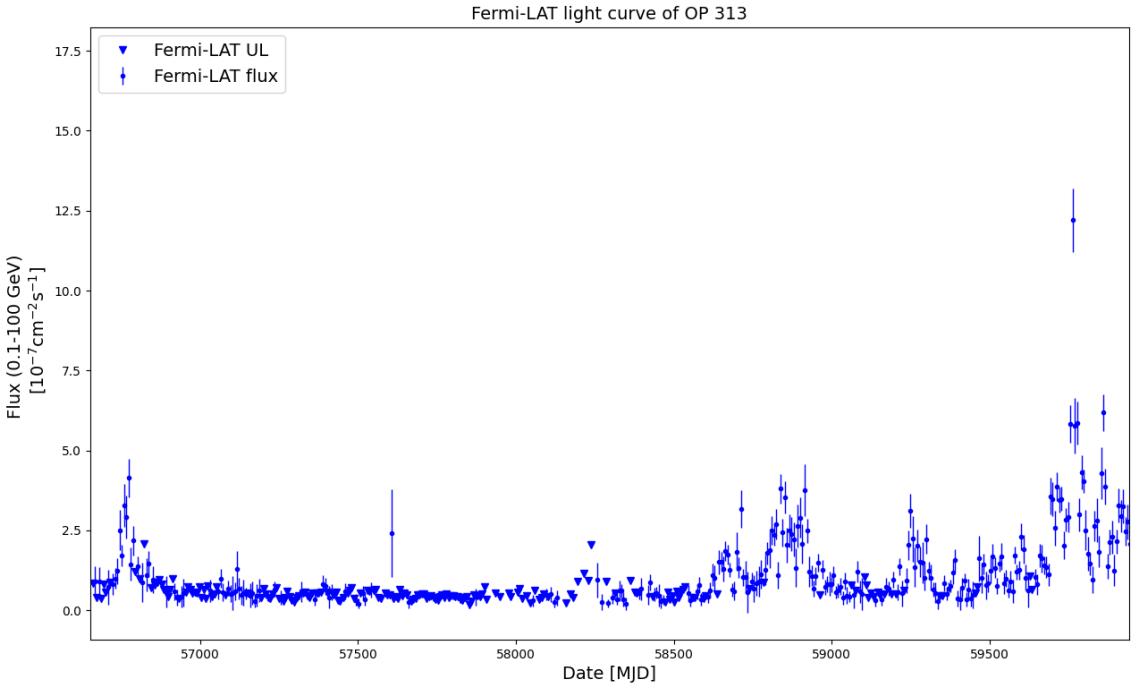

Figure 5.4: Fermi-LAT light curve of OP 313 from 2014 to 2022, using 1-week bin.

flux (E > 100 MeV) of $1.1 \pm 0.2 \times 10^{-6}$ photons cm^{-2} s^{-1}. This corresponds to a flux increase of a factor of 20 relative to the average flux reported in the 4FGL catalog. The corresponding photon index was 1.98 ± 0.14 [88].
Moreover, looking at the Figure 5.4 it is possible to see also small secondary flares occurred in August 2019, March 2020 and February 2021. The Upper Limits (ULs) of the flux are also shown.

5.3 Recent data analysis of the blazar OP 313

During the period 2023-2024 the source entered into an active enhanced state across several energy bands, most notably in optical from the T150 1.5m telescope at the Sierra Nevada Observatory and the 0.30m telescope of the Astronomical Observatory of the University of Siena, X-rays from Swift's X-Ray Telescope and gamma-rays from Fermi-LAT, MAGIC and LST-1 telescopes, as reported by the Astronomers' Telegram (ATels) [92, 93, 94, 95].

5.3.1 Results from MAGIC

The blazar OP 313 has been observed from December 2023 until April 2024 by MAGIC telescopes as a ToO, following alerts of high activity in the Fermi-LAT energy range. In Table 5.3 I present the main information about the MAGIC data of OP 313 that I analyzed, such as period of observations, observational time (T_{obs}), zenith (Zd) range and MC used. The analysis I conducted is a standard MAGIC analysis under moonless sky conditions. The main settings of the analysis are the following:

Date	T_{obs} [h]	MC	Zd range [°]
2023-12-10	1.33	ST.03.20	36-52
2023-12-11	1.13	ST.03.20	33-53
2023-12-12	0.97	ST.03.20	32-44
2023-12-16	1.18	ST.03.20	26-43
2023-12-17	1.58	ST.03.20	25-47
2023-12-18	1.60	ST.03.20	26-47
2023-12-19	1.57	ST.03.20	23-45
2024-01-09	0.93	ST.03.20	19-33
2024-01-10	0.93	ST.03.20	17-20
2024-01-14	0.93	ST.03.20	12-22
2024-01-19	0.93	ST.03.20	25-39
2024-01-20	0.93	ST.03.20	3-10
2024-02-02	2.83	ST.03.20	20-55
2024-02-03	2.13	ST.03.20	19-56
2024-02-05	2.05	ST.03.20	19-41
2024-02-07	2.88	ST.03.20	4-42
2024-02-08	2.90	ST.03.20	4-42
2024-02-11	3.17	ST.03.20	3-38
2024-02-13	1.85	ST.03.20	6-31
2024-02-17	2.25	ST.03.20	4-23
2024-02-29	0.20	ST.03.20	31-35
2024-03-04	6.05	ST.03.20	3-45
2024-03-05	1.90	ST.03.20	3-22
2024-03-06	1.58	ST.03.20	3-18
2024-03-07	1.90	ST.03.20	3-20
2024-03-09	2.23	ST.03.20	3-19
2024-03-10	1.85	ST.03.20	4-16
2024-03-11	2.10	ST.03.20	3-18
2024-03-12	1.88	ST.03.20	3-13
2024-03-15	4.73	ST.03.20	4-37
2024-03-18	2.07	ST.03.20	9-36
2024-03-19	1.13	ST.03.20	21-37
2024-04-04	2.17	ST.03.20	9-39
2024-04-08	0.95	ST.03.20	20-33
2024-04-11	0.15	ST.03.20	23-25

Table 5.3: MAGIC data of OP 313 collected from December 2023 to April 2024. For each observation date, I specified the total observation time, the MC simulations used in the analysis, and the zenith range at which the observations were taken.

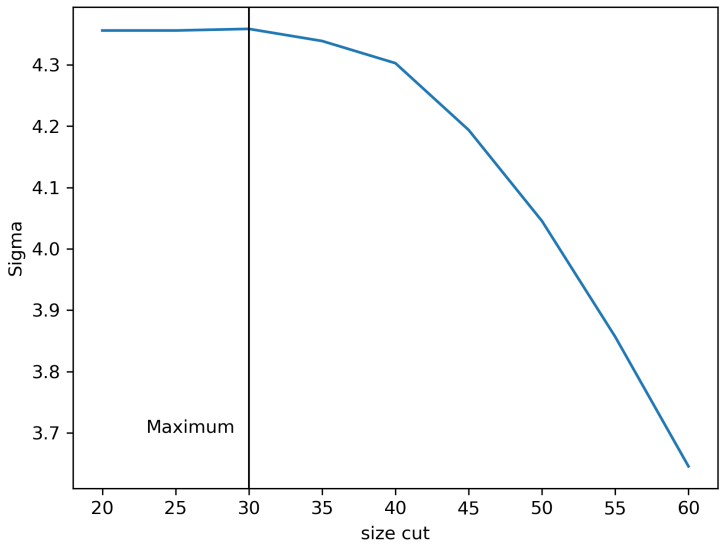

Figure 5.5: Plot of optimizations of the size cuts in energy. It is found that the size cut lowered to 30 photo-electrons provides the highest expected Li&Ma significance. Credit: Lea Heckmann & Axel Arbet-Engels (MAGIC Collaboration).

- I used the latest version of the MARS software (MARS V3-1-0), starting the analysis from the data processed by `superstar`.
- The data were taken in wobble mode with the standard offset of 0.4° from the center of the source.
- The hardware setting is standard full-stereo mode.
- To select data only in good weather conditions I used LIDAR, applying T9km > 0.8 and cloudiness < 35 in the program `quate`. To select data only in dark conditions I applied a cut in `quate` to the direct current: DC < 3000.
- For the OFF sample, I construct two separate RFs based on zenith values: one for 5-35 and another one for 35-50 Zd-ranges, because analyzing data belonging to the same zenith range facilitates a more accurate signal reconstruction. Given the weak nature of OP 313, even minor adjustments can yield significant differences.
- MC data used as train and test samples belong to the period ST.03.20.
- The entire analysis chain was cross-checked with data from the Crab Nebula over the same analysis period (see Appendix B.2).
- Some optimizations of the size cuts in energy were used for the high level analysis. Since OP 313 is a soft source, it was investigated if reducing the size cut to detect more low energy events can show more signal. After a study based on MC simulations, it was found that a size cut lowered to 30 photo-electrons provides the highest expected Li&Ma significance (see Figure 5.5). For this reason, performing the analysis of OP 313, I used size cuts lowered to 30 photo-electrons.

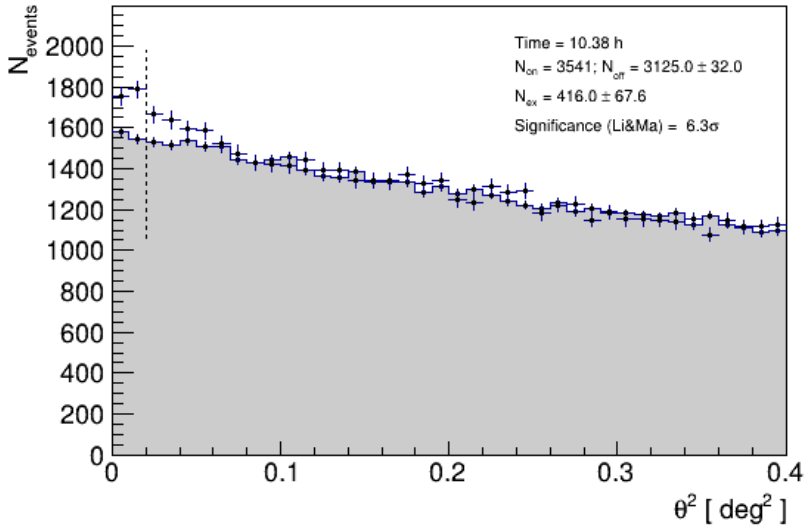

Figure 5.6: θ^2-plot of OP 313 for December 2023 data only.

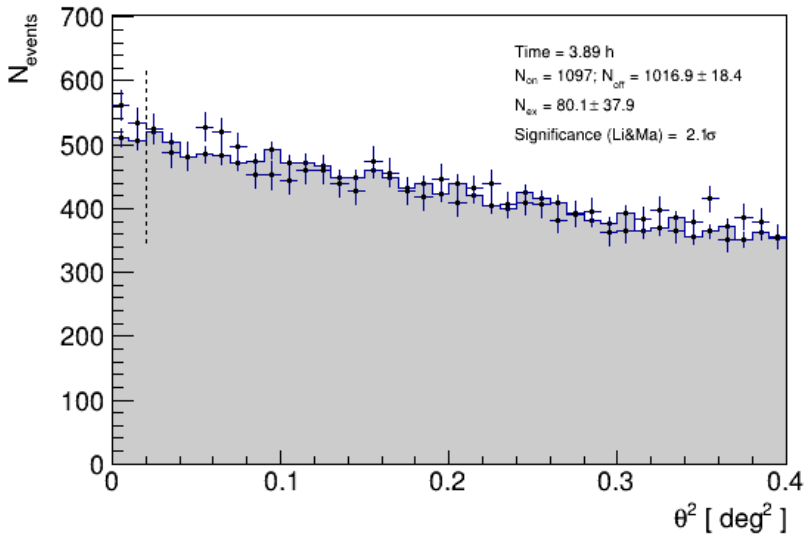

Figure 5.7: θ^2-plot of OP 313 for January 2024 data only.

It is important to note that, in particle physics, the significance required for a detection to occur is 3σ, which corresponds to a probability of 99.7% that the signal recorded by the camera is real [96]. Whereas the significance required to be a scientific discovery is 5σ, which corresponds to a probability of 99.99994% that the signal recorded by the camera is real [97]. After carrying out the procedure described in Chapter 4, I found the following θ^2-plots and sky map in LE range, shown in Figures 5.6-5.11. Specifically, I reported all significances with their respective observation times in Table 5.4.
From them, it has been calculated the significance of the flare of OP 313 that occurred between December 2023 and April 2024, corresponding to 13.8σ. Notably, the emission was strong in December and March, where respective significances of 6.3σ and 12.7σ were recorded. A major flare was observed by MAGIC telescopes on March 15th (see Figure 5.12). Following that, I executed the `flute` program on each dataset

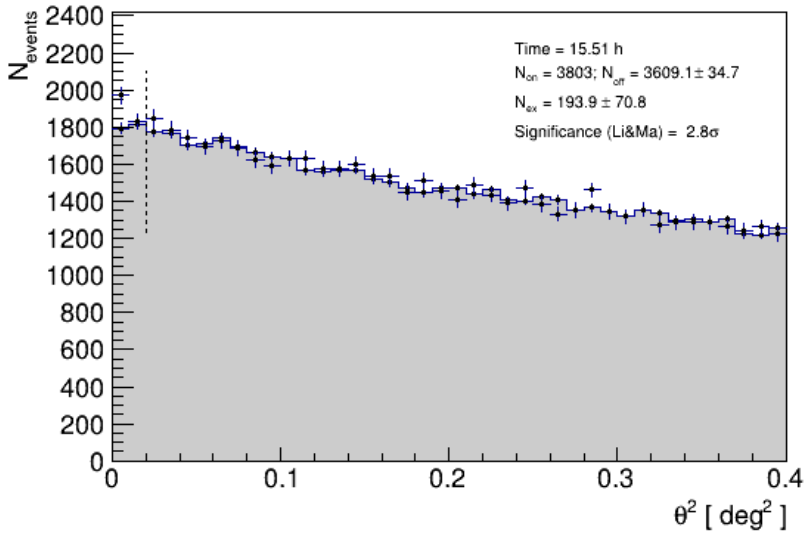

Figure 5.8: θ^2-plot of OP 313 for February 2024 data only.

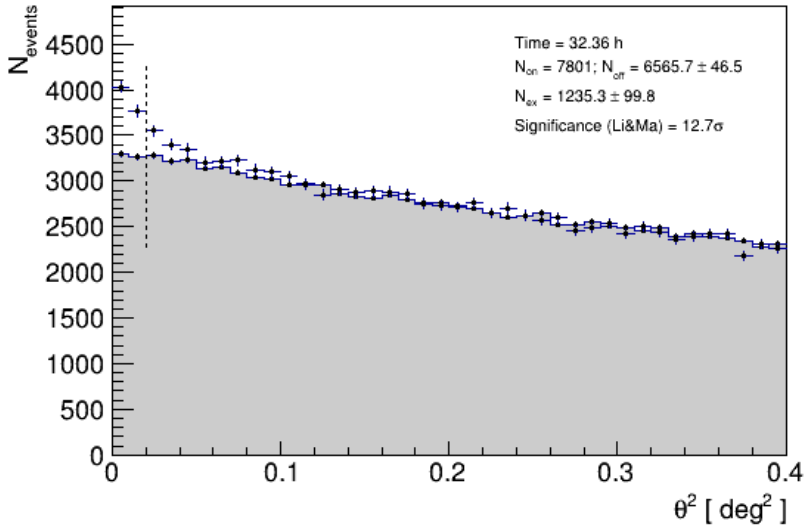

Figure 5.9: θ^2-plot of OP 313 for March and April 2024 data only.

corresponding to the Zd ranges 5-35 and 35-50, subsequently merging the outputs to obtain the SED through the `foam` program, while maintaining a reduced size cut of 30 photo-electrons.
For the `flute` inputs, I specified a minimum energy of 100 GeV (see Appendix C for more explanation) and a redshift of 0.997. I employed Dominguez's model [98] for the EBL and adopted a power law spectral shape before EBL absorption:

$$\frac{d\phi}{dE} = \phi_0 \left(\frac{E}{E_0} \right)^{-\Gamma} \tag{5.1}$$

Here, ϕ represents the integral gamma-ray flux [TeV^{-1} cm^{-2} s^{-1}], E denotes the gamma-ray energy, E_0 stands for the normalization energy (set at 100 GeV), and

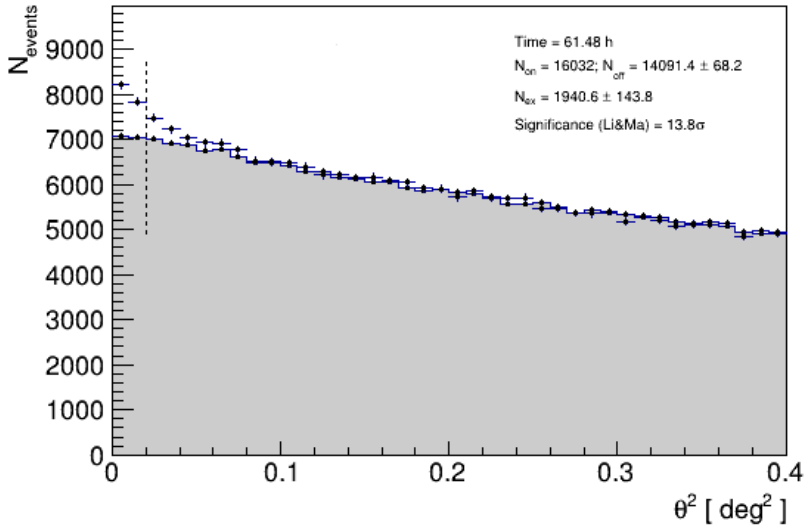

Figure 5.10: θ^2-plot of OP 313 for all data taken in 2023-2024.

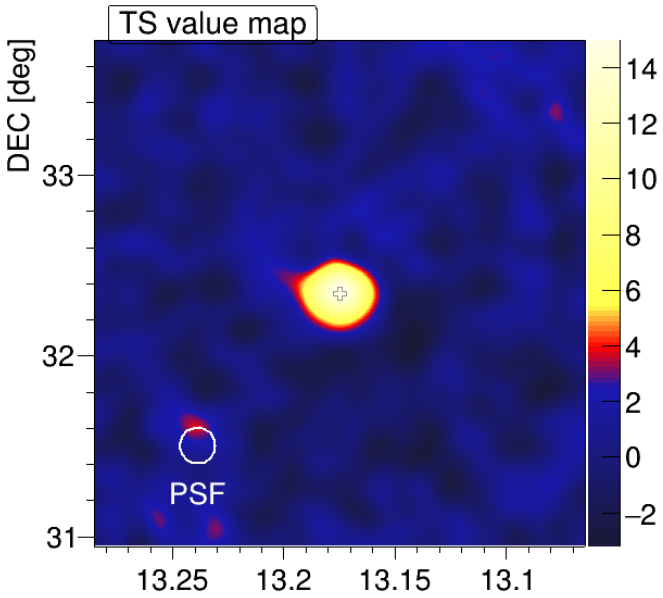

Figure 5.11: Sky map of OP 313 for all data taken in 2023-2024.

Γ is the spectral index (set at 2).
Running `fold`, I found the energy spectrum unfolding shown in Figures 5.13 and 5.14 for Decemeber and March-April (others are available in Appendix C). And I obtain the spectral parameters listed in Table 5.5.
What we can deduce is that the spectral index appears to undergo temporal variations, notably becoming steeper from December to April. Such fluctuations align with the typical spectral behavior observed in blazars [99]. Moreover, the resulting SED post EBL absorption show a prominent cutoff at the highest energies.
The MAGIC light curve from December 2023 to April 2024 is depicted in the top panel of the Figure 5.15.

Month	Observational time [h]	$\sigma_{Li\&Ma}$
December	10.4	6.3
January	3.9	2.1
February	15.5	2.8
March-April	32.4	12.7
Total	61.5	13.8

Table 5.4: Observational times and significances of MAGIC data of OP 313 analyzed for each month from December 2023 to April 2024.

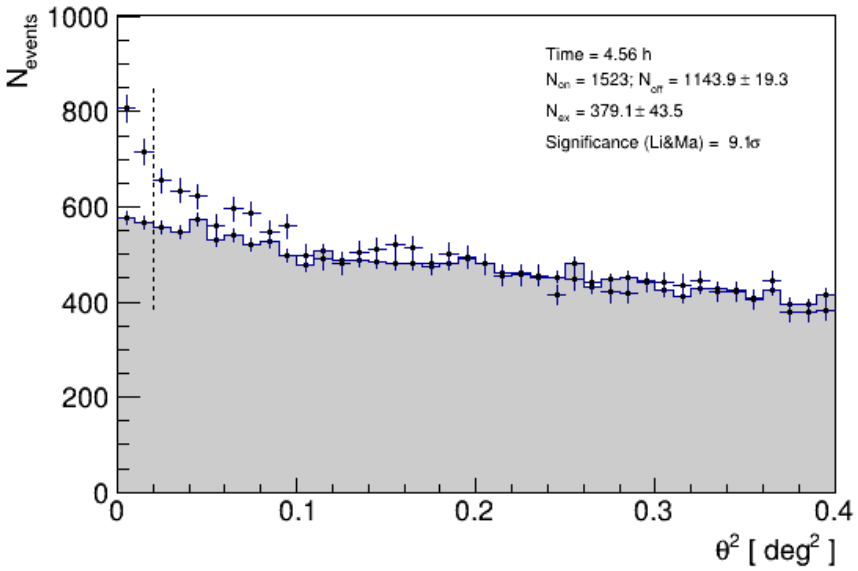

Figure 5.12: θ^2-plot of OP 313 for March 15th only.

5.3.2 Results from Fermi-LAT

In 2023, Fermi-LAT has detected heightened gamma-ray activity originating from a source compatible with the FSRQ OP 313 position [100]. Initial analysis suggests that this source exhibited intensified and hard gamma-ray emissions over the entire period from November 2023 to April 2024, peaking on February 27, with a daily averaged gamma-ray flux (E > 100MeV) of 3.1 ± 0.4 $\times 10^{-6}$ photons cm^{-2} s^{-1}. The corresponding photon index is 1.8 ± 0.1. The observed flux exhibits a remarkable increase, surging by a factor of 60 when contrasted with the average flux documented in the fourth Fermi-LAT catalog (4FGL). This constitutes the highest daily flux ever observed for this source by LAT. The overall light curve of OP 313 by Fermi-LAT is illustrated in the bottom panel of the Figure 5.15. The Figure show another important major flare on November 24, with a daily averaged gamma-ray flux of 1.8 ± 0.2 × 10^{-6} photons cm^{-2} s^{-1}. The corresponding photon index is 1.8 ± 0.06. [94].

Period	ϕ_0	ϕ_0 errors	Γ	Γ errors
Dec.	3.0×10^{-9}	$\pm\ 0.6 \times 10^{-9}$	-2.8	$\pm$ 0.8
Jan.	1.3×10^{-9}	$\pm\ 0.6 \times 10^{-9}$	-2.1	$\pm$ 1.3
Feb.	0.9×10^{-9}	$\pm\ 0.3 \times 10^{-9}$	-3.8	$\pm$ 0.8
Mar-Apr	1.0×10^{-9}	$\pm\ 0.2 \times 10^{-9}$	-4.3	$\pm$ 0.4

Table 5.5: Spectral parameters of OP 313 calculated from December 2023 to April 2024.

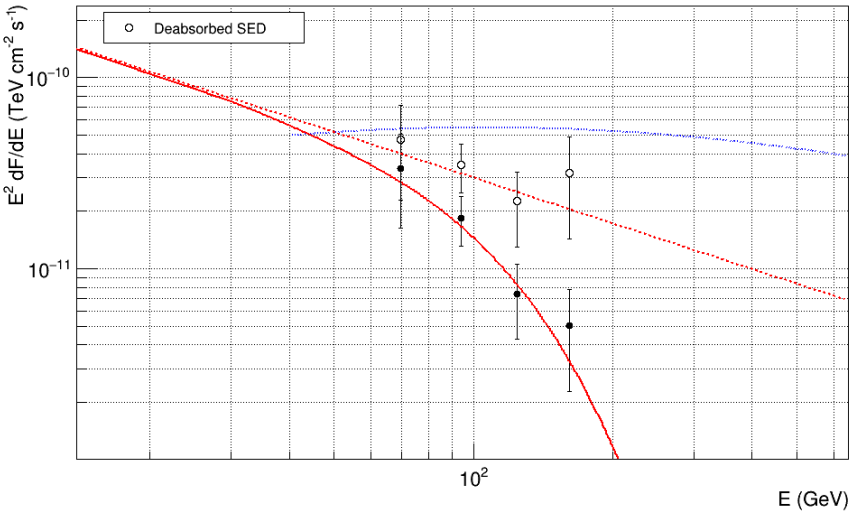

Figure 5.13: Energy spectrum unfolding of OP 313 for December 2023 data only.

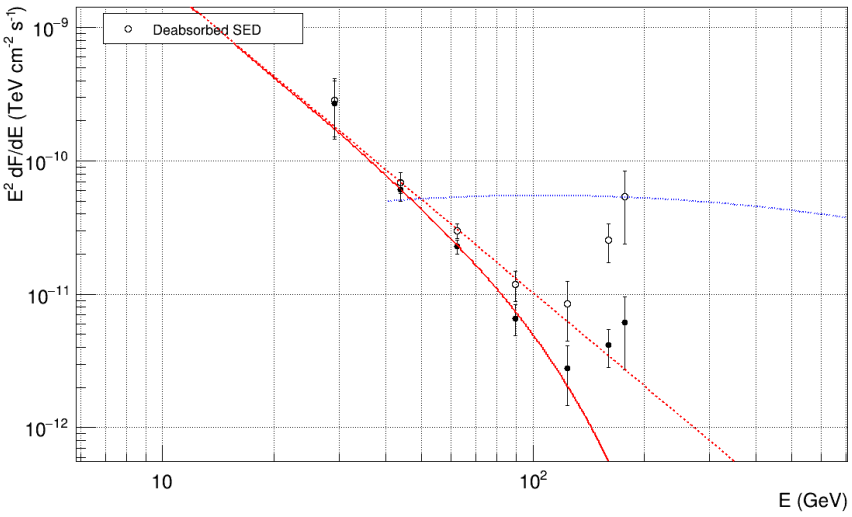

Figure 5.14: Energy spectrum unfolding of OP 313 for March and April 2024 data only.

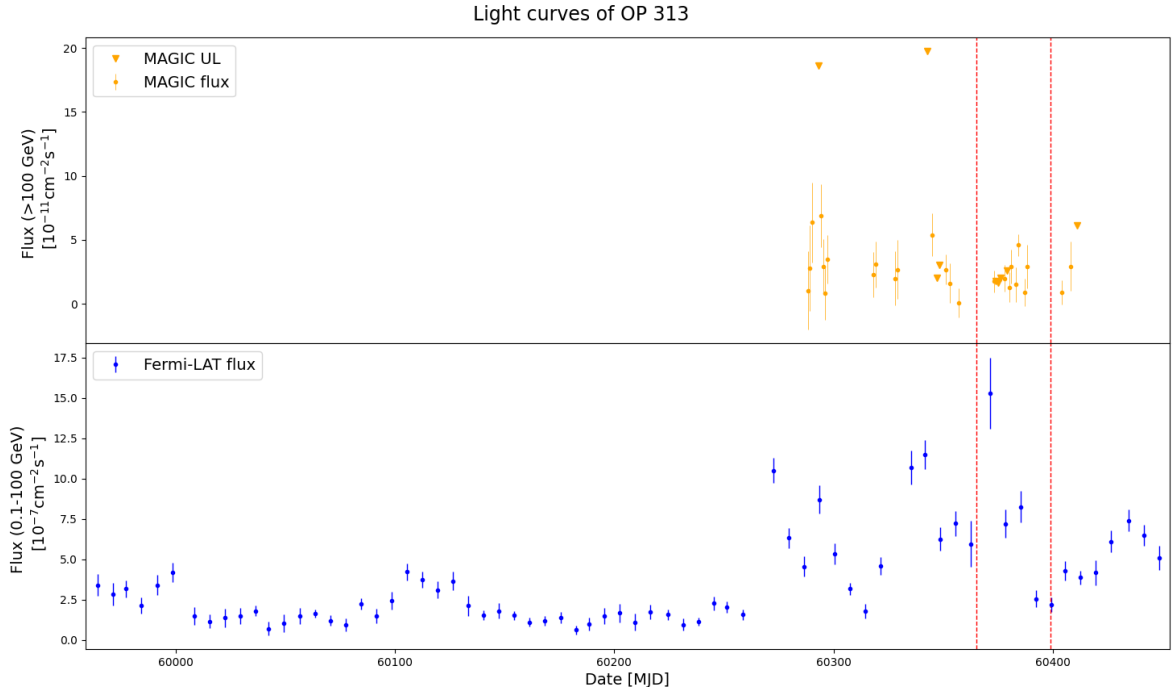

Figure 5.15: MAGIC and Fermi-LAT light curves of OP 313 from December 2023 to April 2024. Fermi-LAT light curve was done using weekly bin from Fermi-LAT Light Curve Repository data (NASA).

5.4 Neutrino alerts from IceCube

On May 5th, 2012, IceCube sent a neutrino alert coming from the direction of OP 313, with a deposited energy of 200 TeV [101], with a post-trial statistical significance of 3.4σ [102, 103]. This high post-trial significance makes the 2012 alert the most notable recorded in the direction of blazar OP 313.
Nevertheless, other multiple alerts were sent by IceCube in 2020 (respectively in April 10, May 1, May 17 and August 27), with a pre-trial significance of 3.1σ [104].
During the observation period 2023-2024, IceCube recorded two neutrino alerts originating from the direction of OP 313, adding significant interest to the multi-messenger survey of this source. As illustrated in Figure 5.16, these alerts were reported on February 25, 2024, and March 30, 2024, each with a pre-trial significance of about 3σ, just above the detection threshold. Therefore, it remains uncertain whether this signal is real; a post-trial significance calculation is required for more accurate verification. Regardless, these alerts are noteworthy because they coincide with a period of strong gamma activity from OP 313. For the first alert, observations began on January 12, 2024, amounting to $\sim$ 45 observation days, yielding a pre-trial significance of 3.16σ. For the second alert, observations started on October 28, 2023, totaling $\sim$ 154 observation days, with a pre-trial significance of 3.03σ. The directions of these alerts can be seen in Figures 5.17 and 5.18 and they are compatible with the sky position of OP 313.

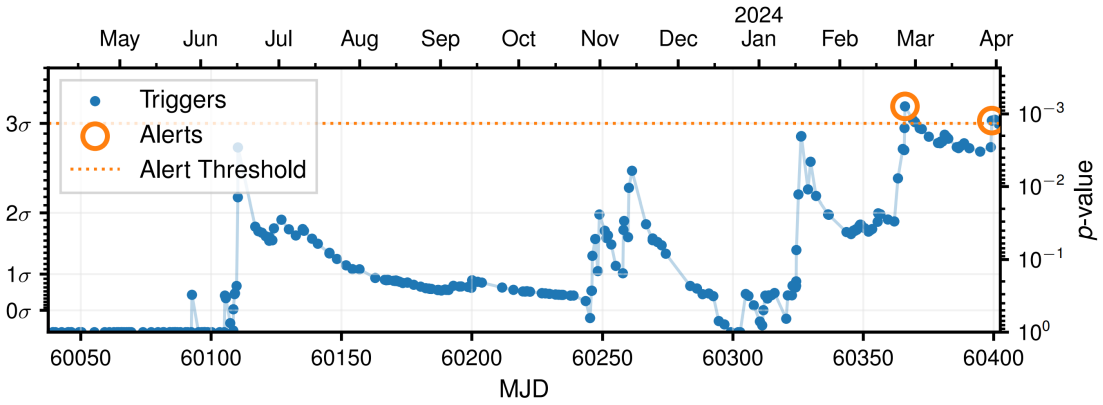

Figure 5.16: Historical neutrino triggers by IceCube at the location of OP 313. Credit: IceCube Collaboration

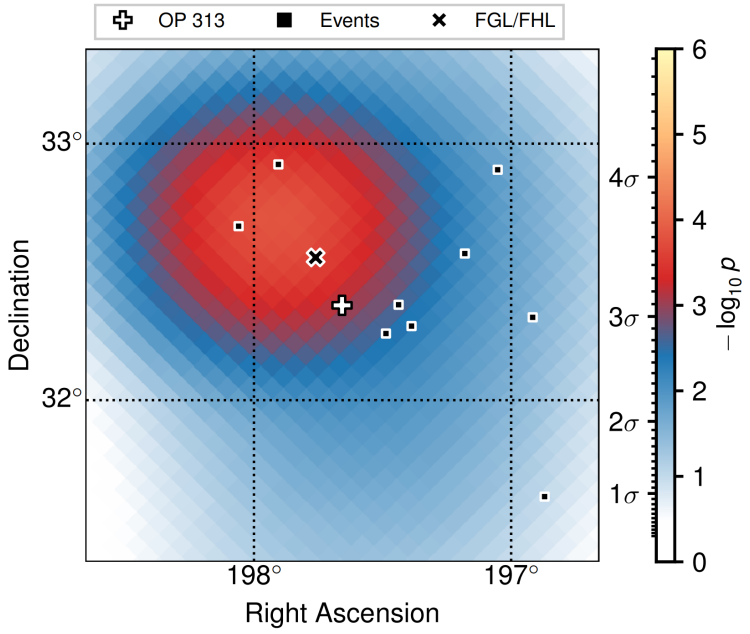

Figure 5.17: Sky map of OP 313 showing neutrinos from the first alert in 2024. Credit: IceCube Collaboration

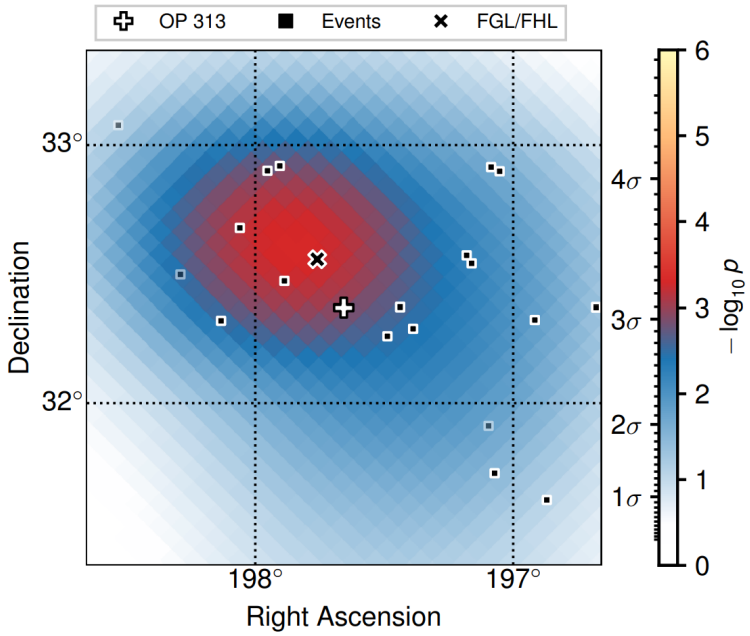

Figure 5.18: Sky map of OP 313 showing neutrinos from the second alert in 2024. Credit: IceCube Collaboration

Chapter 6

CONCLUSIONS AND FUTURE PERSPECTIVES

In this thesis, I focused on the study of the blazar OP 313, particularly I performed the analysis of data collected by the MAGIC telescope and I collected public multi-wavelength information on the source from gamma-ray, X-ray and optical instruments. Subsequently, I examined possible correlations with the neutrino alerts recorded by IceCube, taking a multi-messenger approach to the investigation.
The first significant result of my research is ***the detection of OP 313 in the VHE domain***. Before the start of this thesis project, the blazar OP 313 had never been observed in this energy range. However, my analysis of MAGIC data showed a new result: from December 2023 to April 2024, OP 313 manifested an intense gamma-ray emission, emerging as the most distant AGN ever observed in VHE. Additionally, data from Fermi-LAT confirmed that in the same time window, the blazar OP 313 exhibited its most powerful flare ever documented to date.
A second relevant result concerns ***the variability in terms of temporal and spectral properties of the source***. The first is clearly manifested through the light curves, showing flare periods in 2014, 2022, and the maximum in 2024, interspersed with quiescent phases. The second is observed in SEDs calculated for different time periods, with the spectrum trending steeper over time.
The two recent neutrino alerts from IceCube (March 2024), combined with previous alerts (2012 and 2020), have amplified the interest in multi-messenger analysis of this source. Importantly, the 2020 and 2024 alerts coincide with periods of strong gamma activity in the HE and HE/VHE domains, respectively. However, at present, it cannot be determined with certainty whether these alerts are indicative of real phenomena or can be attributed to background phenomena. Therefore, it is necessary to conduct a more refined analysis in order to assess their significance more clearly.
In Figure 6.1, I have presented a conclusive plot obtained by comparing the light curves of OP 313 from 2014 to 2024, integrating data from telescopes operating in different energy bands: MAGIC (VHE), Fermi-LAT (HE), and Swift-XRT (X-ray) and optical telescopes (G-R-I bands). The Fermi-LAT data were acquired from the Fermi LAT Light Curve Repository (LCR), the Swift-XRT data were extracted from

https://www.swift.ac.uk/ and the optical data from https://fink-portal.org/ and https://asas-sn.osu.edu/. In this plot, it is evident how the emission changes in time, intensifing significantly in the period 2023-2024 in all energy bands.
Among future developments, the application of models for SED based on the most recent data from OP 313 is essential. In particular, the adoption of lepto-hadronic models could allow the evaluation of compatibility with a hadronic scenario. Modeling this blazar could provide important insights into the mechanisms of CR acceleration within the relativistic jets of AGNs.

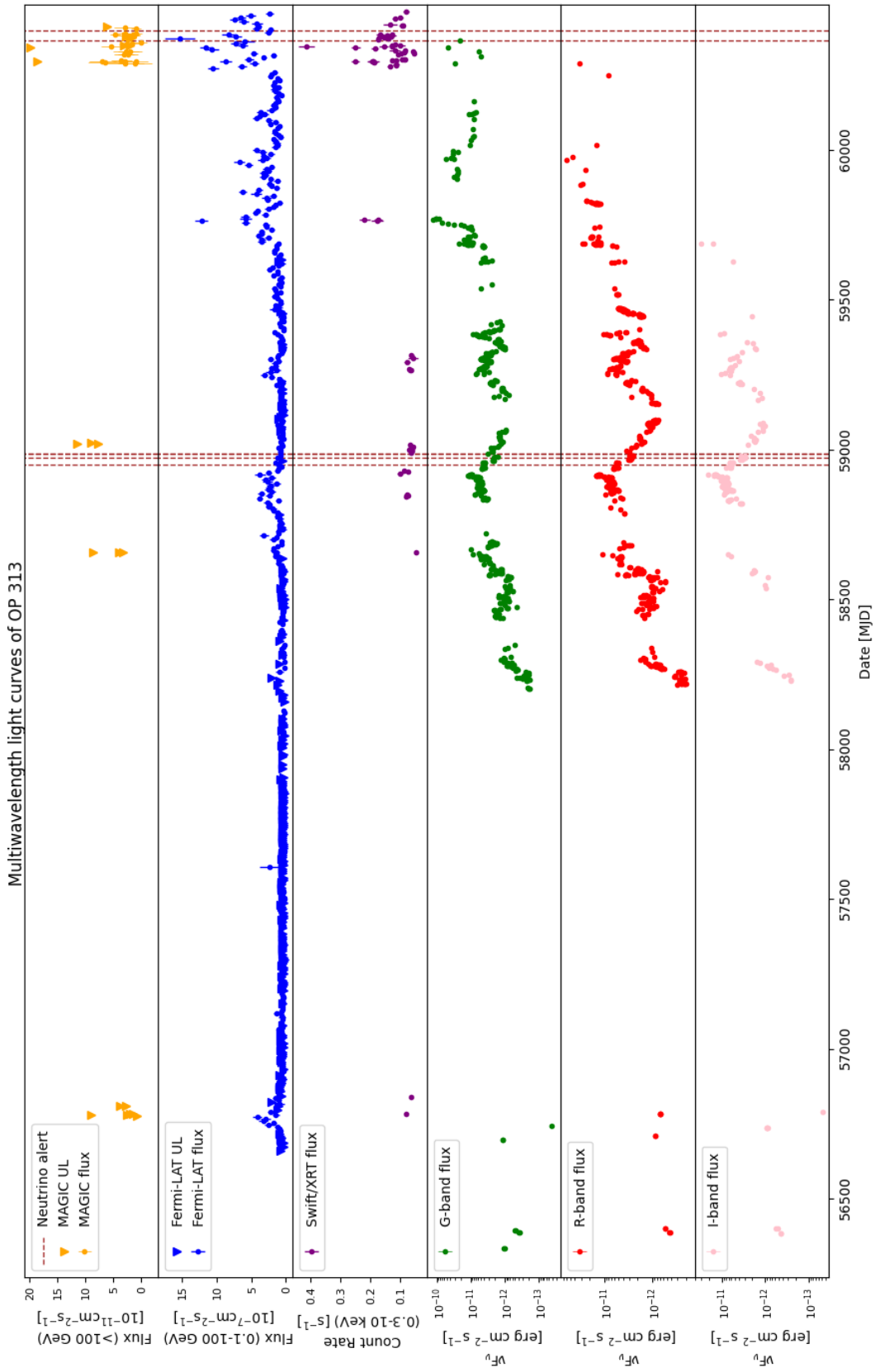

Figure 6.1: Multiwavelenght light curves of OP 313. From top to bottom: MAGIC, Fermi-LAT, Swift-XRT, G-band, R-band, I-band light curves of OP 313.

Appendix A

THE CASE OF THE BLAZAR TXS 0506+056

On September 22, 2017, the IceCube Neutrino Observatory detected a high-energy neutrino event designated IC 170922A coming from the direction of the blazar TXS 0506+056 [1]. This event was notable because it had a high probability (56.5%) of having astrophysical origin, rather than a background atmospheric neutrino, with an energy of $\sim$ 290 TeV. TXS 0506+056 is a BL Lac blazar, with a redshift of 0.3365 $\pm$ 0.0010 [105] and it has been classified as the first known source of high-energy astrophysical neutrinos.
Following the neutrino alert, multiple telescopes and observatories were mobilized to conduct follow-up observations across the electromagnetic spectrum.
In particular, two observations in gamma-ray domain were significant:

- **Fermi-LAT:** The Fermi Gamma-ray Space Telescope detected enhanced gamma-ray activity from a known source, the blazar TXS 0506+056, located 0.1 degrees from the neutrino's best-fit direction.
- **MAGIC Telescopes:** The MAGIC telescopes also detected VHE gamma-rays from TXS 0506+056, providing detailed light curves and spectra. The light curve and spectra for energies above 90 GeV, by MAGIC observations, are displayed in Figure A.1. Specifically, the VHE gamma-ray flux observed by MAGIC showed variability on daily timescales, with notable flares occurring on October 3-4 and October 31, 2017.

The detection of neutrinos and photons from the same source represented a significant breakthrough in multi-messenger astrophysics. This approach has combined different types of cosmic messengers to study astrophysical phenomena, offering a more comprehensive understanding of cosmic events. The combined observations from IceCube and various gamma-ray telescopes provided compelling evidence for a connection between high-energy neutrinos and flaring blazars. This multi-messenger approach has opened new windows for understanding the origins of UHE CRs and the processes driving HE emissions in the Universe.

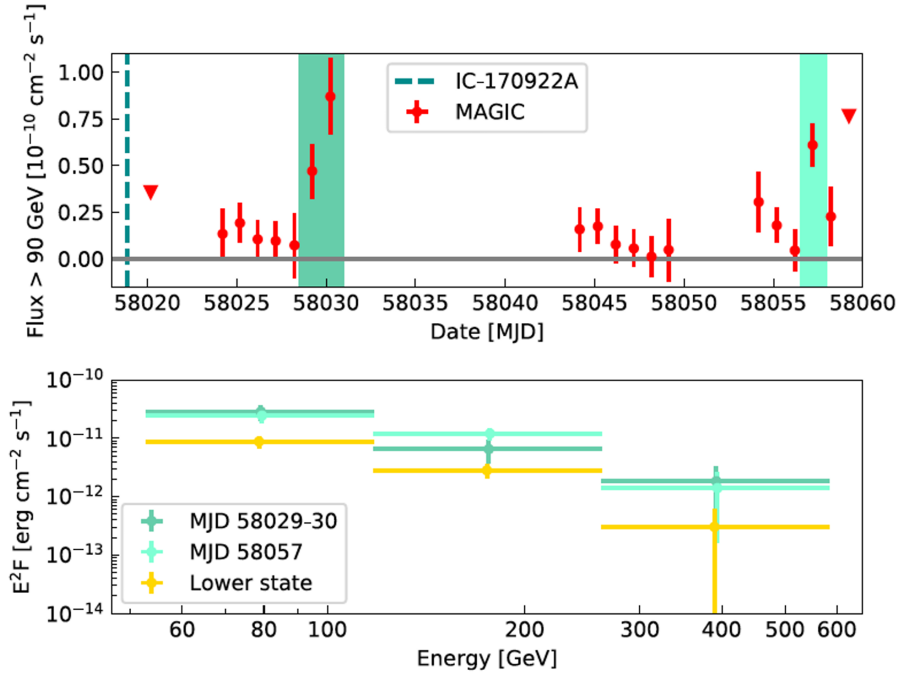

Figure A.1: VHE (E > 90 GeV) light curve and SED of the blazar TXS 0506+056 detected by MAGIC. Top: The colored boxes indicate two periods of enhanced emission, the triangles represent upper limits, the dashed blue line marks the arrival time of the high-energy neutrino event IC-170922A. Bottom: The SED of TXS 0506+056, measured by MAGIC during different observation periods. Figure taken from [106].

Appendix B

CRAB NEBULA CROSS-CHECK FOR MAGIC ANALYSIS

The Crab Nebula is a SNR and PWN in the constellation Taurus. It is one of the most studied objects in HE astrophysics due to its continuous and stable emission across a wide range of the electromagnetic spectrum, from radio waves to gamma-rays. Its role as a standard candle in astrophysics is crucial for the calibration of instruments studying HE phenomena in the Universe. Thanks to these properties, I used Crab Nebula as a cross-check to test the functionality of my data analysis chain. In this appendix I will show the outputs obtained from Crab Nebula standard data analysis for the period ST.03.16 (Section B.1) and for the period ST.03.20 (Section B.2). The small discrepancies present are due to the fact that I built a chain of analysis specifically for extra-galactic objects (using an OFF sample with that origin) because I wanted to optimize it for OP 313, which is an extra-galactic source, as opposed to Crab Nebula, which is instead a galactic object. In any case, the results found are consistent with those found in the literature [107].

B.1 Period ST.03.16

While analyzing the OP 313 data during the period ST.03.16, I performed a standard analysis and I cross-checked my results with the analysis of Crab Nebula data in the same period. I analyzed the Crab Nebula data whit the same characteristics as the OP 313 data: the data were collected in wobble mode, under moonless sky conditions, and within a zenith angle range from 5 to 35 degrees. Using a low energy cut and running the programs `odie`, `caspar`, and `flute`, I generated the plots shown in Figures B.1, B.2, B.3 and B.4, respectively.

B.2 Period ST.03.20

As I analyzed OP 313 data performing a standard analysis during the period ST.03.20, I cross-checked them with Crab Nebula data analysis in the same period. I analyzed Crab Nebula data with the same characteristics as OP 313 data: they were taken

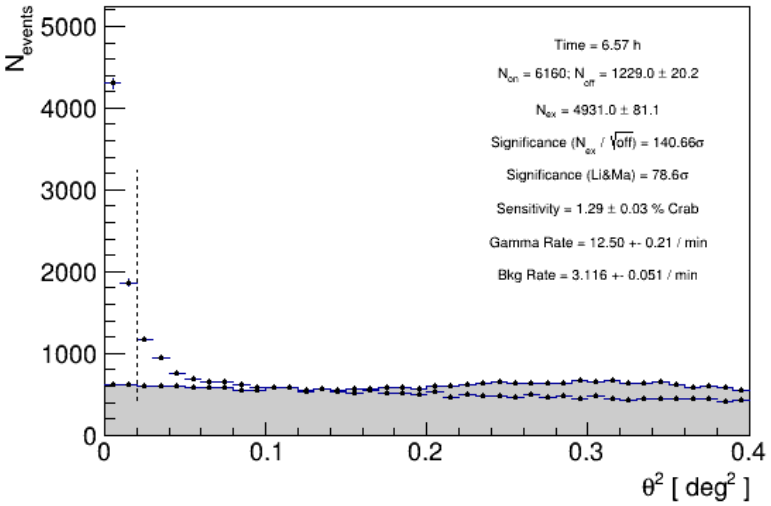

Figure B.1: θ^2 plot of standard Crab Nebula analysis in ST.03.16.

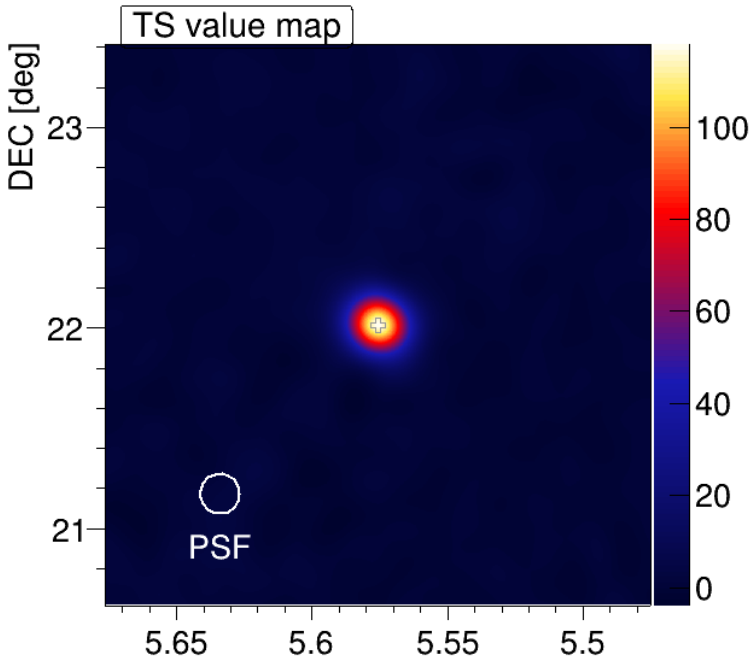

Figure B.2: Sky map of standard Crab Nebula analysis in ST.03.16.

in wobble mode, in moonless sky condition and with zenith range between 5 and 50, split in two samples. Using LE energy cut and running `odie`, `caspar` and `flute` programs I found the plots shown in Figures B.5, B.6, B.7 and B.8, respectively.

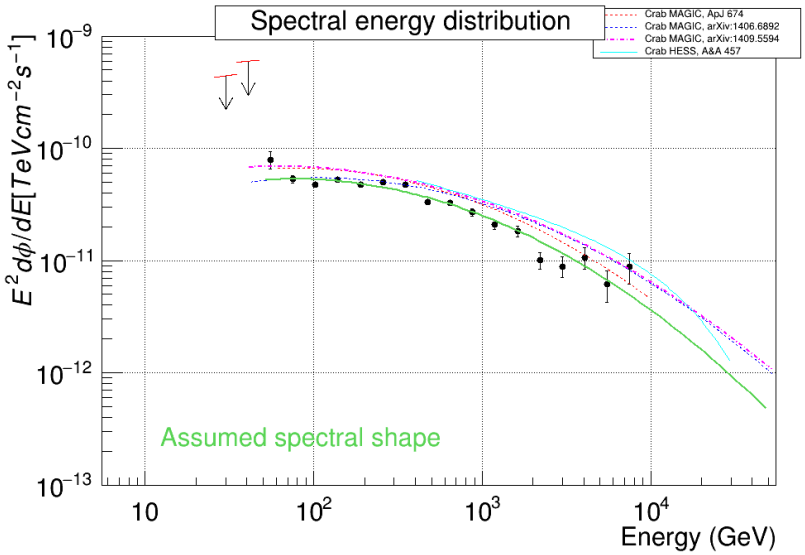

Figure B.3: SED of standard Crab Nebula analysis in ST.03.16.

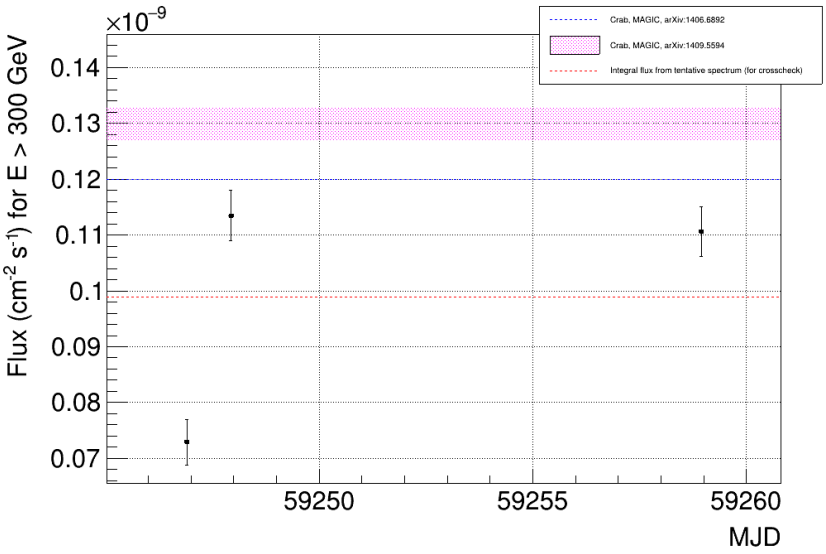

Figure B.4: Light curve of standard Crab Nebula analysis in ST.03.16.

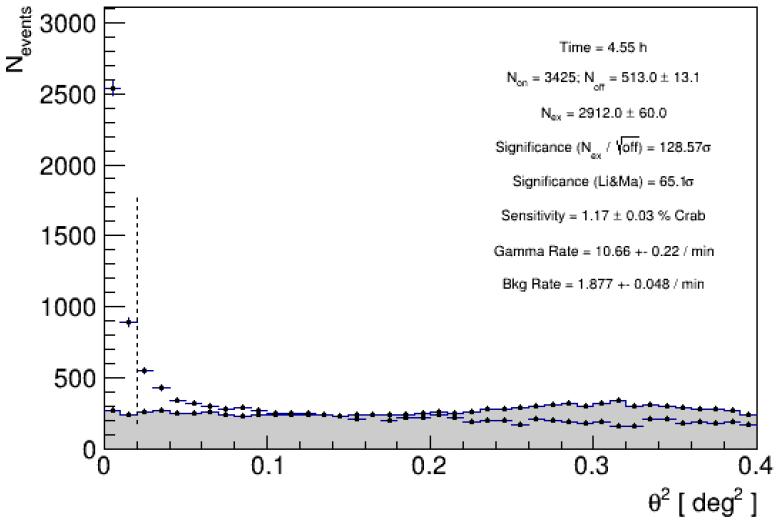

Figure B.5: θ^2 plot of standard Crab Nebula analysis in ST.03.20.

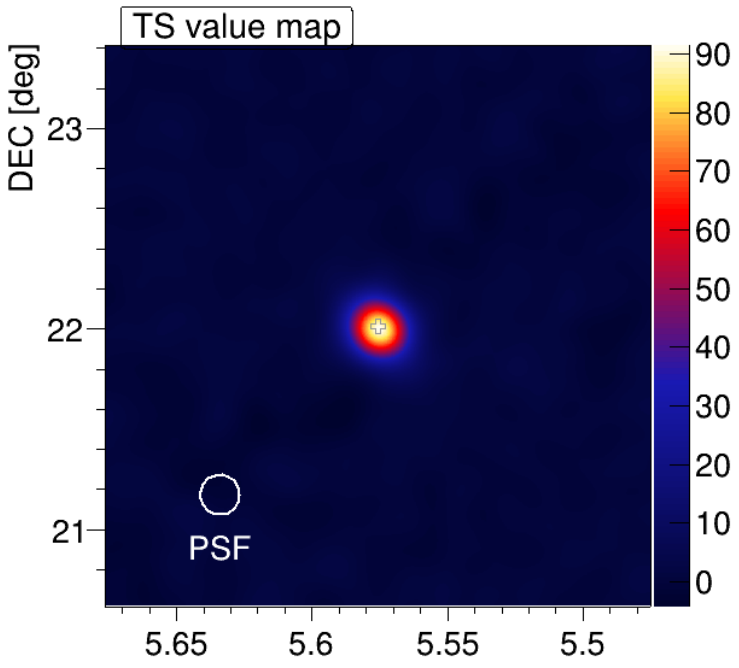

Figure B.6: Sky map of standard Crab Nebula analysis in ST.03.20.

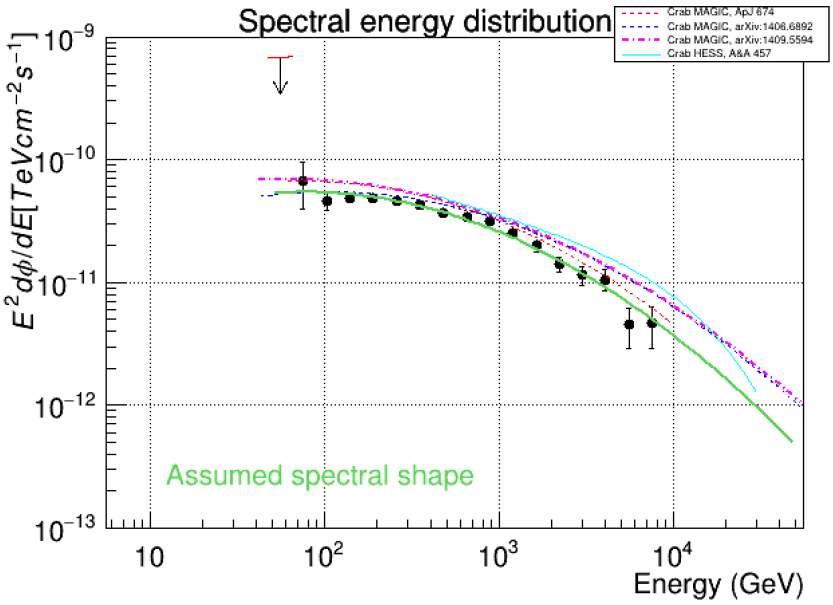

Figure B.7: SED of standard Crab Nebula analysis in ST.03.20.

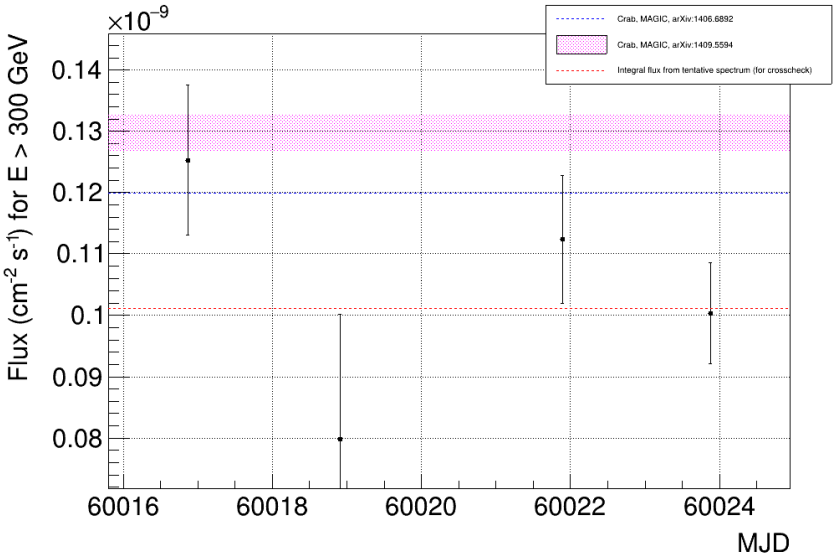

Figure B.8: Light curve of standard Crab Nebula analysis in ST.03.20.

Appendix C

ADDITIONAL MAGIC DATA RESULTS OF OP 313

In this appendix I present additional results obtained during MAGIC data analysis of OP 313 from December 2023 to April 2024. In particular, the sky maps of OP 313 related to the different months of observation obtained with `caspar` (Figures C.1, C.2, C.3, C.4). Then, I report the different SED of OP 313, related to the different months of observation obtained with `flute` and `foam` (Figures C.5, C.6, C.7, C.8). Finally, I inserted the remaining energy spectrum unfolding of OP 313, for January and February, obtained with `fold` (Figures C.9 and C.10).
The energy spectrum unfolding was derived imposing E = 100 GeV as the minimun energy. This cut is justified by estimating the threshold energy based on MC simulations, as done in Figures C.11, C.12. In these figures we can see that the number of excesses is maximized for E $\sim$ 100 GeV. The main settings were the minimun and maximum zenith of the OP 313 sample, the minimun size in energy (set at 30 for OP 313, as explained in Section 5.2), and the spectral index of MCs weighted with that of blazar OP 313 (set at -2). For the plot in December I set a zenith range between 23 and 53, for the plot in March I set a zenith range between 3 and 45 (see values in Table 5.3). Interpolating with a Landau function, I found the following values for the peaks of the excesses: 125 $\pm$ 1.4 GeV in December and 111 $\pm$ 0.8 GeV in March, compatible with my decision of using E = 100 GeV as the minimum energy.

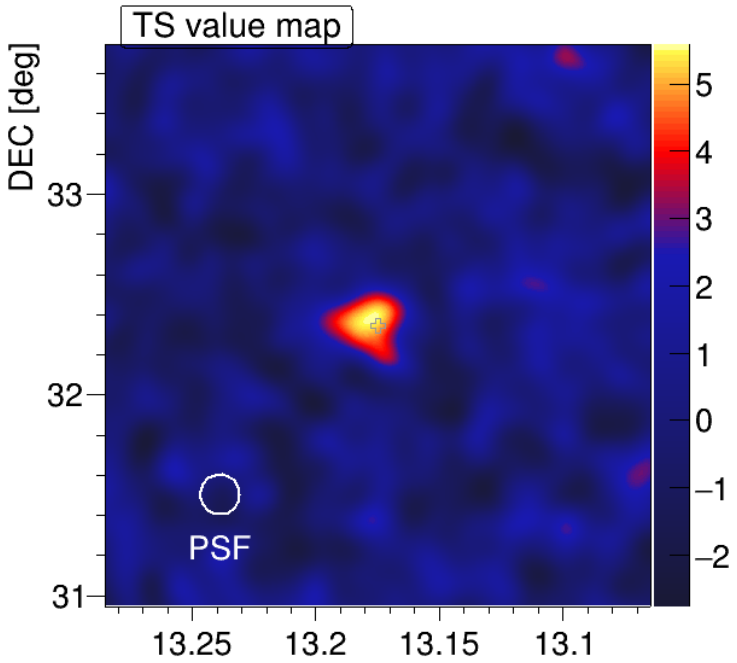

Figure C.1: Sky map of OP 313 for December 2023 data only.

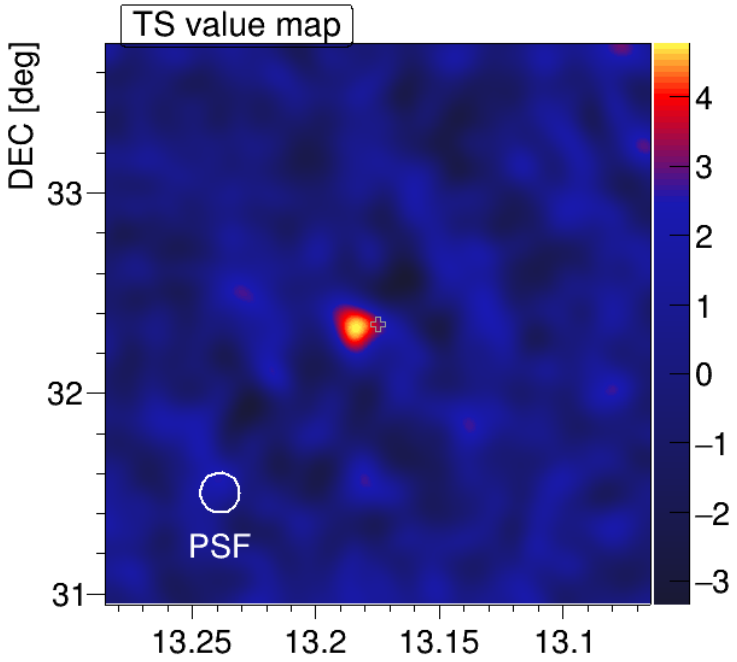

Figure C.2: Sky map of OP 313 for January 2024 data only.

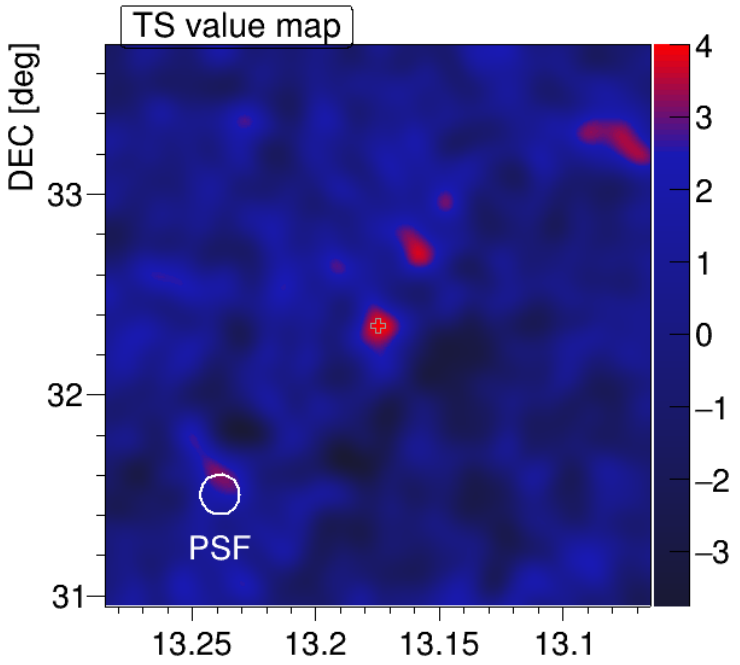

Figure C.3: Sky map of OP313 for February 2024 data only.

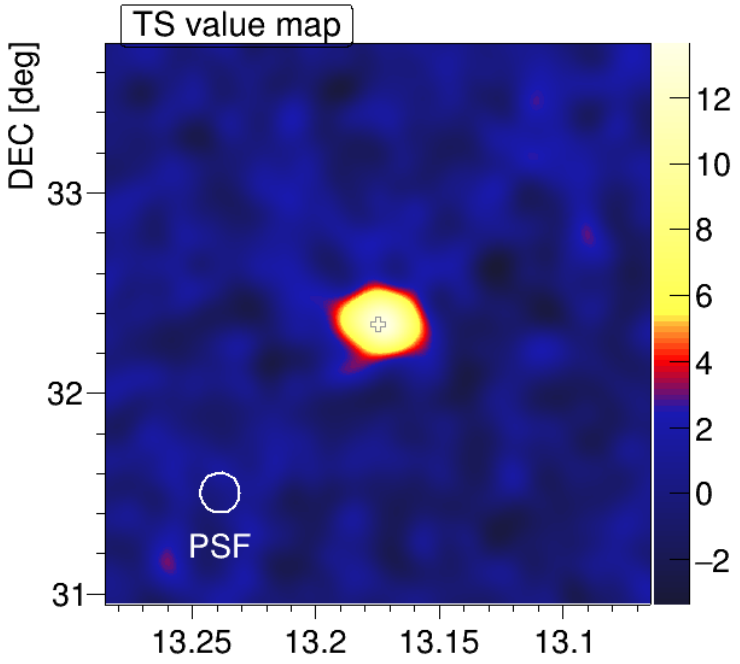

Figure C.4: Sky map of OP 313 for March and April 2024 data only.

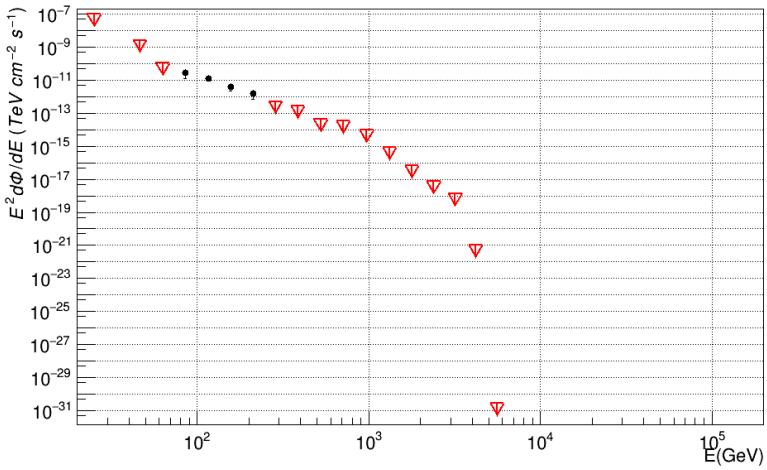

Figure C.5: SED of OP 313 for December 2023 data only.

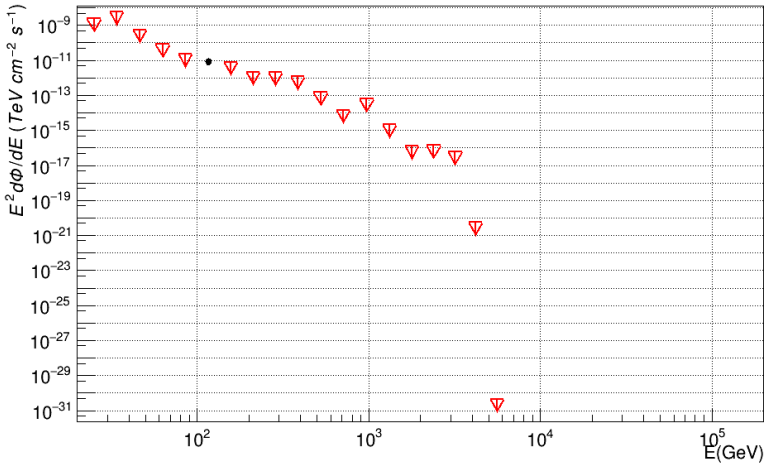

Figure C.6: SED of OP 313 for January 2024 data only.

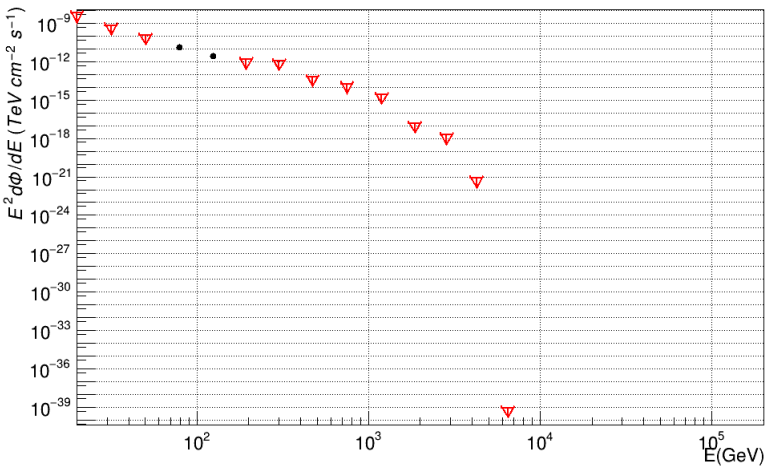

Figure C.7: SED of OP 313 for February 2024 data only.

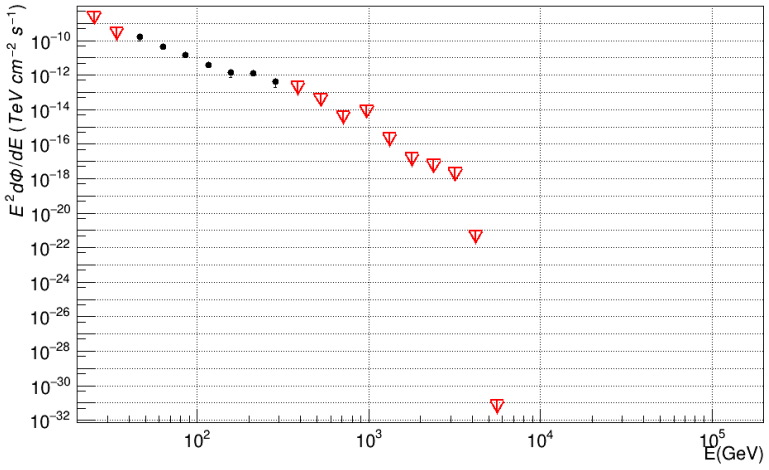

Figure C.8: SED of OP 313 for March and April 2024 data only.

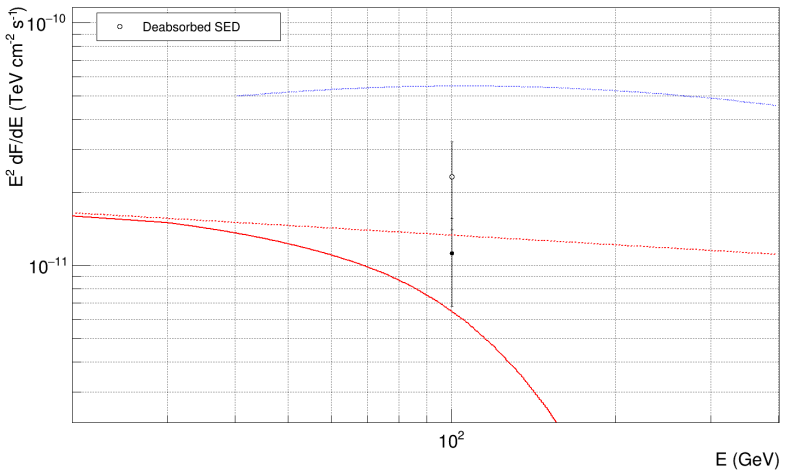

Figure C.9: Energy spectrum unfolding of OP 313 for January 2024 data only.

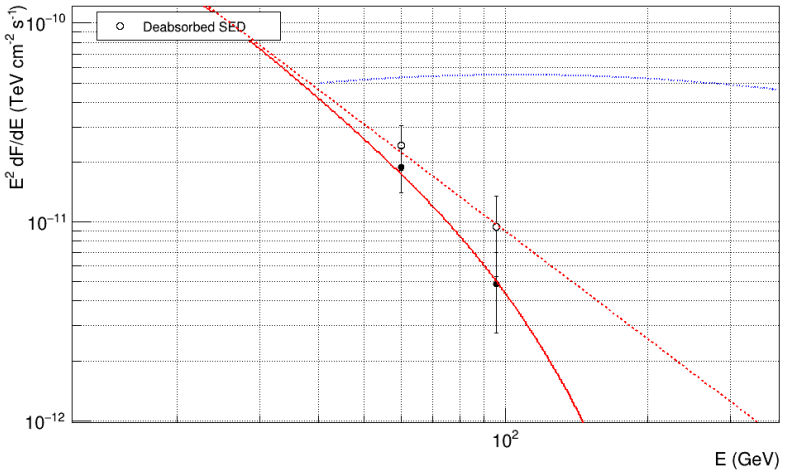

Figure C.10: Energy spectrum unfolding of OP 313 for February 2024 data only.

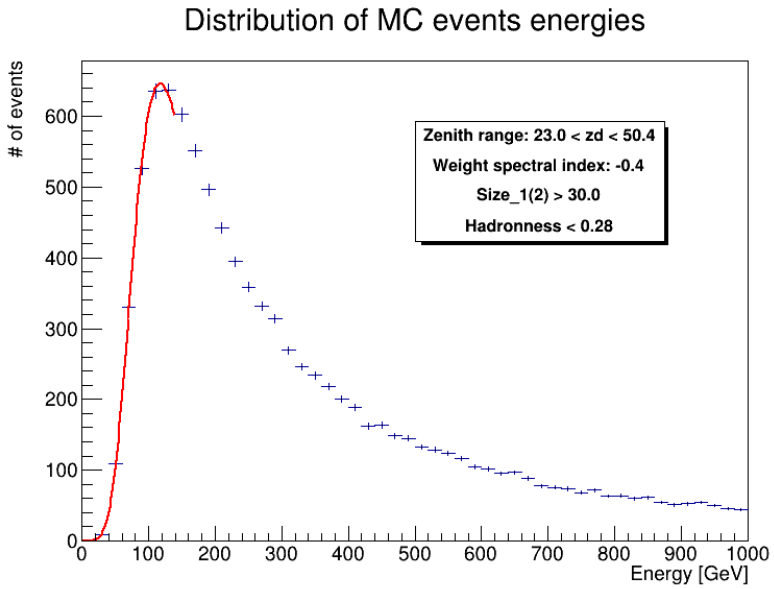

Figure C.11: Number of excesses of OP 313 for December data. Crosses indicate counts; the red line represents the Landau function used for peak interpolation.

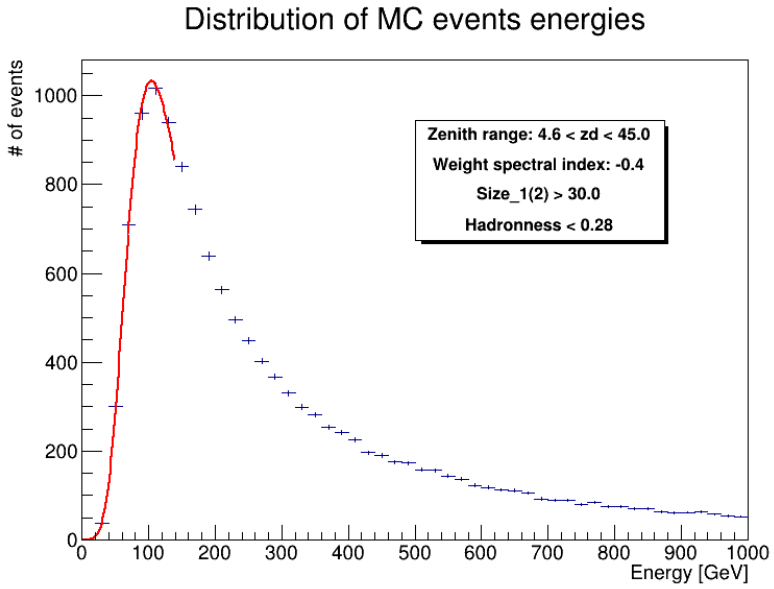

Figure C.12: Number of excesses of OP 313 for March data. Crosses indicate counts; the red line represents the Landau function used for peak interpolation.

Acknowledgments

First, I would like to express my sincere gratitude to my supervisor Prof. Elisa Bernardini for her guidance and vast knowledge throughout my study and research. Her motivation and enthusiasm have been a constant source of inspiration, driving me to strive for excellence in my work.
In addition, I extend my heartfelt thanks to my co-supervisors, Prof. Pratik Majumdar and Dr. Davide Miceli. Prof. Majumdar's invaluable tips during the data analysis phase were instrumental in shaping the direction of my research. Dr. Miceli's insightful comments and encouragement provided the guidance I needed during the entire process of researching and writing this thesis. Their combined expertise and support were crucial to the successful completion of this project.
I would also like to express my gratitude to the entire MAGIC Collaboration, with whom I had the privilege of working over the past months.
A special thanks goes to Dr. Axel Arbet-Engels and Dr. Lea Heckmann for their significant assistance in data analysis. Their useful comments, suggestions, and the comparison of results greatly enhanced the quality and depth of my research.
Finally, I would like to acknowledge my family and friends, who provided both intellectual and emotional support throughout this journey. Their encouragement made the challenging moments more manageable and the successes more meaningful.

The MAGIC Collaboration is acknowledged for allowing the use of proprietary observational data. MAGIC results presented in this thesis have not undergone the internal review procedure of MAGIC publications.

Bibliography

[1] IceCube Collaboration, M. G. Aartsen, M. Ackermann, et al. "Multimessenger observations of a flaring blazar coincident with high-energy neutrino IceCube-170922A". In: *Science* 361.6398 (July 2018), eaat1378. DOI: 10.1126/science.aat1378.

[2] Victor Francis Hess. "Über Beobachtungen der durchdringenden Strahlung bei sieben Freiballonfahrten". In: *Z. Phys.* 13 (1912), p. 1084.

[3] William F Hanlon. "Updated cosmic ray spectrum". In: (2009). URL: https://web.physics.utah.edu/~whanlon/spectrum.html.

[4] Barbara Wiebel-Sooth, Peter L. Biermann, and Hinrich Meyer. "Cosmic rays. VII. Individual element spectra: prediction and data". In: *A&A* 330 (Feb. 1998), pp. 389–398. DOI: 10.48550/arXiv.astro-ph/9709253.

[5] Hans-Heinrich Voigt, P. L. Biermann, G. Börner, et al. *Landolt-Börnstein: Numerical Data and Functional Relationships in Science and Technology - New Series¬Gruppe/Group 6 Astronomy and Astrophysics¬Volume 3 Voigt: Extension and Supplement to Volume 2¬Interstellar Matter, Galaxy, Universe*. 1999.

[6] Kenneth Greisen. "End to the cosmic-ray spectrum?" In: *Physical Review Letters* 16.17 (1966), p. 748.

[7] G. T. Zatsepin and V. A. Kuz'min. "Upper Limit of the Spectrum of Cosmic Rays". In: *Soviet Journal of Experimental and Theoretical Physics Letters* 4 (Aug. 1966), p. 78.

[8] Enrico Fermi. "On the Origin of the Cosmic Radiation". In: *Physical Review* 75.8 (Apr. 1949), pp. 1169–1174. DOI: 10.1103/PhysRev.75.1169.

[9] A. M. Hillas. "The Origin of Ultra-High-Energy Cosmic Rays". In: *High Energy Astrophysics*. Ed. by Frederick Lamb. 1985, p. 277.

[10] Antoine Letessier-Selvon and Todor Stanev. "Ultrahigh energy cosmic rays". In: *Reviews of Modern Physics* 83.3 (July 2011), pp. 907–942. DOI: 10.1103/RevModPhys.83.907.

[11] Maurizio Spurio. *Probes of Multimessenger Astrophysics*. 2018. DOI: 10.1007/978-3-319-96854-4.

[12] Thomas Schwetz, Mariam Tórtola, and José W. F. Valle. "Three-flavour neutrino oscillation update". In: *New Journal of Physics* 10.11, 113011 (Nov. 2008), p. 113011. DOI: 10.1088/1367-2630/10/11/113011.

[13] Y. Fukuda, T. Hayakawa, E. Ichihara, et al. "Evidence for Oscillation of Atmospheric Neutrinos". In: 81.8 (Aug. 1998), pp. 1562–1567. DOI: 10.1103/PhysRevLett.81.1562.

[14] Q. R. Ahmad, R. C. Allen, T. C. Andersen, et al. "Measurement of the Rate of $\nu_e + d \rightarrow p + p + e^-$ Interactions Produced by ^8B Solar Neutrinos at the Sudbury Neutrino Observatory". In: *Phys. Rev. Lett.* 87 (7 July 2001), p. 071301. DOI: 10.1103/PhysRevLett.87.071301.

[15] Q. R. Ahmad, R. C. Allen, T. C. Andersen, et al. "Direct Evidence for Neutrino Flavor Transformation from Neutral-Current Interactions in the Sudbury Neutrino Observatory". In: *Physical Review Letters* 89.1 (June 2002). ISSN: 1079-7114. DOI: 10.1103/physrevlett.89.011301.

[16] Christian Spiering. "Towards high-energy neutrino astronomy. A historical review". In: *European Physical Journal H* 37.3 (Aug. 2012), pp. 515–565. DOI: 10.1140/epjh/e2012-30014-2.

[17] Shan Gao, Anatoli Fedynitch, Walter Winter, et al. "Modelling the coincident observation of a high-energy neutrino and a bright blazar flare". In: *Nature Astronomy* 3 (Jan. 2019), pp. 88–92. DOI: 10.1038/s41550-018-0610-1.

[18] V. Beckmann and C. Shrader. "The AGN phenomenon: open issues". In: *Proceedings of "An INTEGRAL view of the high-energy sky (the first 10 years)" - 9th INTEGRAL Workshop and celebration of the 10th anniversary of the launch (INTEGRAL 2012). 15-19 October 2012. Bibliotheque Nationale de France.* Jan. 2012, 69, p. 69. DOI: 10.22323/1.176.0069.

[19] C. Megan Urry and Paolo Padovani. "Unified Schemes for Radio-Loud Active Galactic Nuclei". In: *PASP* 107 (Sept. 1995), p. 803. DOI: 10.1086/133630.

[20] K. I. Kellermann, R. Sramek, M. Schmidt, et al. "VLA Observations of Objects in the Palomar Bright Quasar Survey". In: *AJ* 98 (Oct. 1989), p. 1195. DOI: 10.1086/115207.

[21] Elisa Prandini and Gabriele Ghisellini. "The Blazar Sequence and Its Physical Understanding". In: *Galaxies* 10.1, 35 (Feb. 2022), p. 35. DOI: 10.3390/galaxies10010035.

[22] Gabriele Ghisellini. *Radiative Processes in High Energy Astrophysics*. Vol. 873. 2013. DOI: 10.1007/978-3-319-00612-3.

[23] Renato Falomo, Elena Pian, and Aldo Treves. "An optical view of BL Lacertae objects". In: *A&AR* 22, 73 (Sept. 2014), p. 73. DOI: 10.1007/s00159-014-0073-z.

[24] G. Fossati, L. Maraschi, A. Celotti, et al. "A unifying view of the spectral energy distributions of blazars". In: *MNRAS* 299.2 (Sept. 1998), pp. 433–448. DOI: 10.1046/j.1365-8711.1998.01828.x.

[25] Malcolm S. Longair. *High Energy Astrophysics*. 2011.

[26] Elisa Prandini, Konstantinos Dialektopoulos, and Jelena Strišković. "Gamma rays: propagation and detection". In: *arXiv e-prints*, arXiv:2211.17021 (Nov. 2022). DOI: 10.48550/arXiv.2211.17021.

[27] Raj Kumar Parajuli, Makoto Sakai, Ramila Parajuli, et al. "Development and Applications of Compton Camera—A Review". In: *Sensors* 22.19 (2022). ISSN: 1424-8220. DOI: 10.3390/s22197374.

[28] Thomas Siegert, Deirdre Horan, and Gottfried Kanbach. "Telescope Concepts in Gamma-Ray Astronomy". In: *Handbook of X-ray and Gamma-ray Astrophysics*. 2022, 80, p. 80. DOI: 10.1007/978-981-16-4544-0_43-1.

[29] Augustine Faanu, James Ephraim, and Emmanuel Darko. "Assessment of public exposure to naturally occurring radioactive materials from mining and mineral processing activities of Tarkwa Goldmine in Ghana". In: *Environmental monitoring and assessment* 180 (Nov. 2010), pp. 15–29. DOI: 10.1007/s10661-010-1769-9.

[30] Janeth Valverde, Nicholas Kirschner, Zachary Metzler, et al. "The Compton-Pair telescope: A prototype for a next-generation MeV γ-ray observatory". In: *arXiv e-prints* (Aug. 2023), arXiv:2308.12464. DOI: 10.48550/arXiv.2308.12464.

[31] V. Schoenfelder, H. Aarts, K. Bennett, et al. "Instrument Description and Performance of the Imaging Gamma-Ray Telescope COMPTEL aboard the Compton Gamma-Ray Observatory". In: *ApJS* 86 (June 1993), p. 657. DOI: 10.1086/191794.

[32] David J. Thompson and Alexander A. Moiseev. "Pair Production Detectors for Gamma-Ray Astrophysics". In: *Handbook of X-ray and Gamma-ray Astrophysics*. 2022, 54, p. 54. DOI: 10.1007/978-981-16-4544-0_159-1.

[33] W. B. Atwood, A. A. Abdo, M. Ackermann, et al. "The Large Area Telescope on the Fermi Gamma-Ray Space Telescope Mission". In: *ApJ* 697.2 (June 2009), pp. 1071–1102. DOI: 10.1088/0004-637X/697/2/1071.

[34] G. F. Knoll. *Radiation detection and measurement*. 1979.

[35] David J. Thompson. "Space detectors for gamma rays (100 MeV-100 GeV): From EGRET to Fermi LAT". In: *Comptes Rendus Physique* 16.6-7 (Aug. 2015), pp. 600–609. DOI: 10.1016/j.crhy.2015.07.002.

[36] Manel Errando and Takayuki Saito. "How to Detect Gamma Rays from Ground: An Introduction to the Detection Concepts". In: *Handbook of X-ray and Gamma-ray Astrophysics (eds. C. Bambi*. 2023, 144, p. 144. DOI: 10.1007/978-981-16-4544-0_61-1.

[37] W. Heitler. *Quantum theory of radiation*. 1954.

[38] Mathieu de Naurois and Daniel Mazin. "Ground-based detectors in very-high-energy gamma-ray astronomy". In: *Comptes Rendus Physique* 16.6-7 (Aug. 2015), pp. 610–627. DOI: 10.1016/j.crhy.2015.08.011.

[39] Marion Guelfand, Simon Chiche, Kumiko Kotera, et al. "Particle content of very inclined air showers for radio signal modeling". In: 2024.5, 055 (May 2024), p. 055. DOI: 10.1088/1475-7516/2024/05/055.

[40] G. Di Sciascio. "Measurement of Energy Spectrum and Elemental Composition of PeV Cosmic Rays: Open Problems and Prospects". In: *arXiv e-prints*, arXiv:2202.11618 (Feb. 2022). DOI: 10.48550/arXiv.2202.11618.

[41] J. Matthews. "A Heitler model of extensive air showers". In: *Astroparticle Physics* 22.5-6 (Jan. 2005), pp. 387–397. DOI: 10.1016/j.astropartphys.2004.09.003.

[42] Alessandro De Angelis and Mário Pimenta. *Introduction to Particle and Astroparticle Physics*. 2018. DOI: 10.1007/978-3-319-78181-5.

[43] Travis M. Shaffer, Edwin C. Pratt, and Jan Grimm. "Utilizing the power of Cerenkov light with nanotechnology". In: *Nature Nanotechnology* 12.2 (Feb. 2017), pp. 106–117. DOI: 10.1038/nnano.2016.301.

[44] PA Cerenkov et al. "Visible emission of clean liquids by action of γ radiation". In: *Dokl. Akad. Nauk SSSR*. Vol. 2. 8. 1934, pp. 451–454.

[45] Trevor C. Weekes. *Very high energy gamma-ray astronomy*. 2003.

[46] Jamie Holder. "Atmospheric Cherenkov Gamma-Ray Telescopes". In: *The WSPC Handbook of Astronomical Instrumentation, Volume 5: Gamma-Ray and Multimessenger Astronomical Instrumentation*. 2021, pp. 117–136. DOI: 10.1142/9789811203817_0006.

[47] J. Aleksić, S. Ansoldi, L. A. Antonelli, et al. "The major upgrade of the MAGIC telescopes, Part II: A performance study using observations of the Crab Nebula". In: *Astroparticle Physics* 72 (Jan. 2016), pp. 76–94. DOI: 10.1016/j.astropartphys.2015.02.005.

[48] H. Anderhub, M. Backes, A. Biland, et al. "FACT—The first Cherenkov telescope using a G-APD camera for TeV gamma-ray astronomy". In: *Nuclear Instruments and Methods in Physics Research A* 639.1 (May 2011), pp. 58–61. DOI: 10.1016/j.nima.2010.10.081.

[49] J Holder and VERITAS collaboration. "VERITAS: status and performance". In: *Science With The New Generation Of High Energy Gamma-Ray Experiments: The Variable Gamma-Ray Sources: Their Identifications and Counterparts*. World Scientific, 2007, pp. 69–76.

[50] M. Actis, G. Agnetta, F. Aharonian, et al. "Design concepts for the Cherenkov Telescope Array CTA: an advanced facility for ground-based high-energy gamma-ray astronomy". In: *Experimental Astronomy* 32.3 (Dec. 2011), pp. 193–316. DOI: 10.1007/s10686-011-9247-0.

[51] M. Doro, D. Bastieri, A. Biland, et al. "The reflective surface of the MAGIC telescope". In: *Nuclear Instruments and Methods in Physics Research A* 595.1 (Sept. 2008), pp. 200–203. DOI: 10.1016/j.nima.2008.07.073.

[52] J. R. García, F. Dazzi, D. Häfner, et al. "Status of the new Sum-Trigger system for the MAGIC telescopes". In: *arXiv e-prints*, arXiv:1404.4219 (Apr. 2014), arXiv:1404.4219. DOI: 10.48550/arXiv.1404.4219.

[53] R. López-Coto, D. Mazin, R. Paoletti, et al. "The Topo-trigger: a new concept of stereo trigger system for imaging atmospheric Cherenkov telescopes". In: *Journal of Instrumentation* 11.4 (Apr. 2016), P04005. DOI: 10.1088/1748-0221/11/04/P04005.

[54] IceCube-Gen2 Collaboration, : M. G. Aartsen, et al. "IceCube-Gen2: A Vision for the Future of Neutrino Astronomy in Antarctica". In: *arXiv e-prints* (Dec. 2014), arXiv:1412.5106. DOI: 10.48550/arXiv.1412.5106.

[55] Wrijupan Bhattacharyya. "Observation of Very High Energy gamma-rays from Active Galactic Nuclei and characterization of their non-thermal emission mechanisms". In: (2019).

[56] G. Fogli, E. Lisi, Alessandro Mirizzi, et al. "Probing supernova shock waves and neutrino flavor transitions in next-generation water Cerenkov detectors". In: *Journal of Cosmology and Astroparticle Physics* 2005 (Dec. 2004). DOI: 10.1088/1475-7516/2005/04/002.

[57] Konstantia Balasi, Christos Markou, K. Tzamarioudaki, et al. "The response of an autonomous underwater telescope to high energy neutrinos for the observation of Gamma-ray bursts (GRBs)". In: *HNPS Proceedings* 22 (Mar. 2019), p. 88. DOI: 10.12681/hnps.1936.

[58] M. G. Aartsen, M. Ackermann, J. Adams, et al. "Search for Sources of Astrophysical Neutrinos Using Seven Years of IceCube Cascade Events". In: *The Astrophysical Journal* 886.1 (Nov. 2019), p. 12. DOI: 10.3847/1538-4357/ab4ae2.

[59] M. G. Aartsen, M. Ackermann, J. Adams, et al. "The IceCube Neutrino Observatory: instrumentation and online systems". In: *Journal of Instrumentation* 12.3 (Mar. 2017), P03012. DOI: 10.1088/1748-0221/12/03/P03012.

[60] Thomas Kintscher. *Rapid response to extraordinary events: transient neutrino sources with the IceCube experiment*. Humboldt Universitaet zu Berlin (Germany), 2020.

[61] M. Ackermann, E. Bernardini, N. Galante, et al. "Neutrino Triggered Target of Opportunity (NToO) test run with AMANDA-II and MAGIC". In: *International Cosmic Ray Conference*. Vol. 3. International Cosmic Ray Conference. Jan. 2008, pp. 1257–1260. DOI: 10.48550/arXiv.0709.2640.

[62] M. G. Aartsen, M. Ackermann, J. Adams, et al. "The IceCube realtime alert system". In: *Astroparticle Physics* 92 (June 2017), pp. 30–41. DOI: 10.1016/j.astropartphys.2017.05.002.

[63] M. G. Aartsen, R. Abbasi, M. Ackermann, et al. "Energy reconstruction methods in the IceCube neutrino telescope". In: *Journal of Instrumentation* 9.3, P03009 (Mar. 2014), P03009. DOI: 10.1088/1748-0221/9/03/P03009. arXiv: 1311.4767 [physics.ins-det].

[64] M. L. Ahnen, S. Ansoldi, L. A. Antonelli, et al. "Performance of the MAGIC telescopes under moonlight". In: *Astroparticle Physics* 94 (Sept. 2017), pp. 29–41. DOI: 10.1016/j.astropartphys.2017.08.001.

[65] Ruben Lopez-Coto. "Very-high-energy gamma-ray observations of pulsar wind nebulae and cataclysmic variable stars with MAGIC and development of trigger systems for IACTs". PhD thesis. Autonomous University of Barcelona, Spain, July 2015.

[66] D. Heck, J. Knapp, J. N. Capdevielle, et al. *CORSIKA: a Monte Carlo code to simulate extensive air showers.* 1998.

[67] R. Mirzoyan. "On the Calibration Accuracy of Light Sensors in Atmospheric Cherenkov Fluorescence and Neutrino Experiments". In: *International Cosmic Ray Conference*. Vol. 7. International Cosmic Ray Conference. Jan. 1997, p. 265.

[68] Alessio Berti et al. "Study of astrophysical transients with the MAGIC telescopes". In: (2018).

[69] A. M. Hillas. "Cerenkov Light Images of EAS Produced by Primary Gamma Rays and by Nuclei". In: *19th International Cosmic Ray Conference (ICRC19), Volume 3*. Vol. 3. International Cosmic Ray Conference. Aug. 1985, p. 445.

[70] F. A. Aharonian, W. Hofmann, A. K. Konopelko, et al. "The potential of ground based arrays of imaging atmospheric Cherenkov telescopes. I. Determination of shower parameters". In: *Astroparticle Physics* 6.3-4 (Mar. 1997), pp. 343–368. DOI: 10.1016/S0927-6505(96)00069-2.

[71] W. Hofmann, I. Jung, A. Konopelko, et al. "Comparison of techniques to reconstruct VHE gamma-ray showers from multiple stereoscopic Cherenkov images". In: *Astroparticle Physics* 12.3 (Nov. 1999), pp. 135–143. DOI: 10.1016/S0927-6505(99)00084-5.

[72] Corrado Gini. "Measurement of Inequality of Income". In: *Economic Journal* 31 (Jan. 1921). DOI: 10.2307/2223319.

[73] V. P. Fomin, A. A. Stepanian, R. C. Lamb, et al. "New methods of atmospheric Cherenkov imaging for gamma-ray astronomy. I. The false source method". In: *Astroparticle Physics* 2.2 (May 1994), pp. 137–150. DOI: 10.1016/0927-6505(94)90036-1.

[74] R.W. Lessard, J.H. Buckley, V. Connaughton, et al. "A new analysis method for reconstructing the arrival direction of TeV gamma rays using a single imaging atmospheric Cherenkov telescope". In: *Astroparticle Physics* 15.1 (2001), pp. 1–18. ISSN: 0927-6505. DOI: https://doi.org/10.1016/S0927-6505(00)00133-X.

[75] J. Aleksić, E. A. Alvarez, L. A. Antonelli, et al. "Performance of the MAGIC stereo system obtained with Crab Nebula data". In: *Astroparticle Physics* 35.7 (Feb. 2012), pp. 435–448. DOI: 10.1016/j.astropartphys.2011.11.007.

[76] T. -P. Li and Y. -Q. Ma. "Analysis methods for results in gamma-ray astronomy." In: *ApJ* 272 (Sept. 1983), pp. 317–324. DOI: 10.1086/161295.

[77] S. Abdollahi, F. Acero, M. Ackermann, et al. "Fermi Large Area Telescope Fourth Source Catalog". In: *ApJS* 247.1, 33 (Mar. 2020), p. 33. DOI: 10.3847/1538-4365/ab6bcb.

[78] J. Aleksić, S. Ansoldi, L. A. Antonelli, et al. "Search for very high energy gamma-rays from the z = 0.896 quasar 4C +55.17 with the MAGIC telescopes". In: *MNRAS* 440.1 (May 2014), pp. 530–535. DOI: 10.1093/mnras/stu227.

[79] Manuel Meyer, Jeffrey D. Scargle, and Roger D. Blandford. "Characterizing the Gamma-Ray Variability of the Brightest Flat Spectrum Radio Quasars Observed with the Fermi LAT". In: *ApJ* 877.1, 39 (May 2019), p. 39. DOI: 10.3847/1538-4357/ab1651.

[80] J. Ballet, T. H. Burnett, S. W. Digel, et al. "Fermi Large Area Telescope Fourth Source Catalog Data Release 2". In: *arXiv e-prints* (May 2020). DOI: 10.48550/arXiv.2005.11208.

[81] Paul C. Hewett and Vivienne Wild. "Improved redshifts for SDSS quasar spectra". In: *Monthly Notices of the Royal Astronomical Society* 405.4 (July 2010), pp. 2302–2316. ISSN: 0035-8711. DOI: 10.1111/j.1365-2966.2010.16648.x.

[82] Buson Sara. "Fermi LAT Detection of a GeV Flare from OP 313 (B2 1308+32)". In: *The Astronomer's Telegram* 6068 (Apr. 2014), p. 1.

[83] Mangal Hazra, Sabyasachi Pal, and Debasish Saha. "Fermi/LAT detection of enhanced gamma-ray activity from the blazars OP 313 and 4C +01.02". In: *The Astronomer's Telegram* 14404 (Feb. 2021), p. 1.

[84] Thomas J. Balonek, Miguel De Los Santos, Daniel Dougherty, et al. "ATel 12898: Rapid Optical Flaring of the Quasar 1308+326". In: *The Astronomer's Telegram* 12898 (June 2019), p. 1.

[85] John J. Slater, Riley M. Corcoran, Warner S. Neal, et al. "Optical Flares in Blazars 1156+295, 1308+326 and 1749+096". In: *The Astronomer's Telegram* 14727 (June 2021), p. 1.

[86] Riley M. Corcoran, John J. Slater, Warner S. Neal, et al. "Continued Optical Flaring in Blazar 1308+326". In: *The Astronomer's Telegram* 15334 (Apr. 2022), p. 1.

[87] L. Carrasco, G. Escobedo, A. Porras, et al. "A recent NIR flare of the Blazar GB6J1310+3220". In: *The Astronomer's Telegram* 15428 (June 2022), p. 1.

[88] S. Garrappa. "Fermi-LAT detection of enhanced gamma-ray activity from the FSRQ OP 313 (B2 1308+32)". In: *The Astronomer's Telegram* 15483 (June 2022), p. 1.

[89] Madeline L. Hulburt, Ha-Eun H. Choi, Norah Du, et al. "Unprecedented Optical Flare Continues in Blazar 1308+326, Reaching Historic Maximum Brightness". In: *The Astronomer's Telegram* 15474 (June 2022), p. 1.

[90] E. K. Urbach, C. W. Stubbs, L. Denneau, et al. "ATLAS photometry of 1308+326 shows continued brightening". In: *The Astronomer's Telegram* 15480 (June 2022), p. 1.

[91] MAGIC Collaboration. "Constraints on VHE gamma-ray emission of Flat Spectrum Radio Quasars with the MAGIC telescopes". In: *arXiv e-prints* (Mar. 2024). DOI: 10.48550/arXiv.2403.13713.

[92] J. Otero-Santos, V. Piirola, L. Pacciani, et al. "Optical follow-up of the gamma-ray flare of the blazar OP 313 reveals a bright state with high polarization degree". In: *The Astronomer's Telegram* 16360 (Dec. 2023), p. 1.

[93] F. D'Ammando and A. Arbet-Engels. "Swift-XRT follow-up confirms the high activity state of the FSRQ OP 313". In: *The Astronomer's Telegram* 16504 (Mar. 2024), p. 1.

[94] Chiara Bartolini, Federica Giacchino, Maria Stella Gisonna, et al. "Fermi-LAT detection of renewed gamma-ray activity from the FSRQ OP 313, and enhanced gamma-ray activity from the FSRQ ON 393". In: *The Astronomer's Telegram* 16356 (Dec. 2023), p. 1.

[95] Juan Cortina and CTAO LST Collaboration. "First detection of VHE gamma-ray emission from FSRQ OP 313 with LST-1". In: *The Astronomer's Telegram* 16381 (Dec. 2023), p. 1.

[96] C. J. Miller, R. C. Nichol, L. Wasserman, et al. "What Does a Three-Sigma Detection Really Mean?" In: *American Astronomical Society Meeting Abstracts #198*. Vol. 198. American Astronomical Society Meeting Abstracts. May 2001, 30.04, p. 30.04.

[97] Louis Lyons. "Discovering the Significance of 5 sigma". In: *arXiv e-prints* (Oct. 2013). DOI: 10.48550/arXiv.1310.1284.

[98] A. Domínguez, J. R. Primack, D. J. Rosario, et al. "Extragalactic background light inferred from AEGIS galaxy-SED-type fractions". In: *MNRAS* 410.4 (Feb. 2011), pp. 2556–2578. DOI: 10.1111/j.1365-2966.2010.17631.x.

[99] Pankaj Kushwaha, Alok C. Gupta, Paul J. Wiita, et al. "Multiwavelength temporal and spectral variability of the blazar OJ 287 during and after the 2015 December flare: a major accretion disc contribution". In: *MNRAS* 473.1 (Jan. 2018), pp. 1145–1156. eprint: 1709.04957 (astro-ph.HE).

[100] Chiara Bartolini. "Fermi-LAT detection of renewed gamma-ray activity from the FSRQ OP 313". In: *The Astronomer's Telegram* 16497 (Mar. 2024), p. 1.

[101] Antonio Marinelli, J. Rodrigo Sacahui, Ankur Sharma, et al. "Analysing the gamma-ray activity of neutrino emitter candidates: comparing TXS 0506+056 with other blazars". In: *MNRAS* 506.3 (Sept. 2021), pp. 3760–3772. DOI: 10.1093/mnras/stab1312.

[102] Alexander Plavin, Yuri Y. Kovalev, Yuri A. Kovalev, et al. "Observational Evidence for the Origin of High-energy Neutrinos in Parsec-scale Nuclei of Radio-bright Active Galaxies". In: *ApJ* 894.2 (May 2020), p. 101. DOI: 10.3847/1538-4357/ab86bd.

[103] A. V. Plavin, Y. Y. Kovalev, Yu. A. Kovalev, et al. "Directional Association of TeV to PeV Astrophysical Neutrinos with Radio Blazars". In: *ApJ* 908.2 (Feb. 2021), p. 157. DOI: 10.3847/1538-4357/abceb8.

[104] The Fact Collaboration, The H. E. S. S. Collaboration, The Icecube Collaboration, et al. "Searching for VHE gamma-ray emission associated with IceCube neutrino alerts using FACT, H.E.S.S., MAGIC, and VERITAS". In: *37th International Cosmic Ray Conference*. Mar. 2022, p. 960. DOI: 10.22323/1.395.0960.

[105] Simona Paiano, Renato Falomo, Aldo Treves, et al. "The Redshift of the BL Lac Object TXS 0506+056". In: *ApJL* 854.2 (Feb. 2018), p. L32. DOI: 10.3847/2041-8213/aaad5e.

[106] S. Ansoldi, L. A. Antonelli, C. Arcaro, et al. "The Blazar TXS 0506+056 Associated with a High-energy Neutrino: Insights into Extragalactic Jets and Cosmic-Ray Acceleration". In: *ApJL* 863.1 (Aug. 2018), p. L10. DOI: 10.3847/2041-8213/aad083.

[107] J. Albert, E. Aliu, H. Anderhub, et al. "VHE γ-Ray Observation of the Crab Nebula and its Pulsar with the MAGIC Telescope". In: *ApJ* 674.2 (Feb. 2008), pp. 1037–1055. DOI: 10.1086/525270.